Award Number: W81XWH-09-1-0391

TITLE:
Host Genes and Resistance/Sensitivity to Military Priority Pathogens

PRINCIPAL INVESTIGATOR:
Gerald I. Byrne, Ph.D.

CONTRACTING ORGANIZATION:
University of Tennessee Health Science Center
Memphis, Tennessee 38163-1201

REPORT DATE:
June 2012

TYPE OF REPORT: Annual

PREPARED FOR: U.S. Army Medical Research and Materiel Command
Fort Detrick, Maryland 21702-5012

DISTRIBUTION STATEMENT: Approved for Public Release;
Distribution Unlimited

The views, opinions and/or findings contained in this report are those of the author(s) and should not be construed as an official Department of the Army position, policy or decision unless so designated by other documentation.

REPORT DOCUMENTATION PAGE

Form Approved
OMB No. 0704-0188

Public reporting burden for this collection of information is estimated to average 1 hour per response, including the time for reviewing instructions, searching existing data sources, gathering and maintaining the data needed, and completing and reviewing this collection of information. Send comments regarding this burden estimate or any other aspect of this collection of information, including suggestions for reducing this burden to Department of Defense, Washington Headquarters Services, Directorate for Information Operations and Reports (0704-0188), 1215 Jefferson Davis Highway, Suite 1204, Arlington, VA 22202-4302. Respondents should be aware that notwithstanding any other provision of law, no person shall be subject to any penalty for failing to comply with a collection of information if it does not display a currently valid OMB control number. **PLEASE DO NOT RETURN YOUR FORM TO THE ABOVE ADDRESS.**

1. REPORT DATE *(DD-MM-YYYY)*	**2. REPORT TYPE**	**3. DATES COVERED** *(From - To)*
06-1-2012	Annual	06/01/11 – 06/30/2012

4. TITLE AND SUBTITLE

Host Genes and Resistance/Sensitivity to Military Priority Pathogens

5b. GRANT NUMBER
W81XWH-09-1-0391

5c. PROGRAM ELEMENT NUMBER

6. AUTHOR(S)

Byrne, Gerald, I; Cui, Yan; Li, Kui; Lu, Lu; Miller, Mark, A; Williams, Robert; Marion, Tony.

E

5e. TASK NUMBER

5f. WORK UNIT NUMBER

7. PERFORMING ORGANIZATION NAME(S) AND ADDRESS(ES)

University of Tennessee Health Science Center
Memphis TN 38163-1201

8. PERFORMING ORGANIZATION REPORT NUMBER

9. SPONSORING / MONITORING AGENCY NAME(S) AND ADDRESS(ES)
U.S. Army Medical Research and Material Command
Fort Detrick, MD 21702-5012

10. SPONSOR/MONITOR'S ACRONYM(S)

11. SPONSOR/MONITOR'S REPORT NUMBER(S)

12. DISTRIBUTION / AVAILABILITY STATEMENT
Approved for public release; distribution unlimited

13. SUPPLEMENTARY NOTES

14. ABSTRACT

This report provides data from our study of differential susceptibility to DoD priority pathogens (*Francisella tularensis* (FT), *Burkholderia pseudomallei* (Bp), *Acinetobacter baumannii* (Ab), *Leishmania major* (Lm), SARS, H5Ni avian influenza) using BXD recombinant inbred mice. We have identified 38 phenotypes that may that may lead to differential immune responsiveness of C57BL/6 (B6) vs DBA/2 (D2) mice following Ab infection. Data from the Bp study indicates that survival of acute pneumonic Burkholderia infection is a complex trait that may involve at least 3 different loci. FT studies have shown that there are differences in innate immune responses to pneumonic FT infection between B6 and D2 mice. The SARS study found that D2 mice are more susceptible to MA15 virus than B6 mice. The mouse genomics core continues to generate datasets (spleen, lung, T-cells, etc) from BXD strains, which are available on GeneNetwork. The bioinformatics core has implemented a method for performing Bayesian network analysis of biological data, such as responses to pathogen infection and other biological processes. Studies with all the pathogens are ongoing to identify host genes/pathways that are involved in disease process.

5a. CONTRACT NUMBER

15. SUBJECT TERMS
Host genetics, Pathogens, Biodefense, Disease susceptibility, Humanized mice

16. SECURITY CLASSIFICATION OF:			**17. LIMITATION OF ABSTRACT**	**18. NUMBER OF PAGES**	**19a. NAME OF RESPONSIBLE PERSON**
a. REPORT	**b. ABSTRACT**	**c. THIS PAGE**			USAMRMC
U	U	U	UU	65	**19b. TELEPHONE NUMBER** *(include area code)*

Table of Contents

Page

Introduction 4

Key Research Accomplishments, Reportable Outcomes, Conclusion, References

1. DoD-priority Bacterial Pathogens
   - 1.1 *Acinetobacter baumannii* project 5
   - 1.2 *Burkholderia pseudomallei* project 11
   - 1.3 *Francisella tularensis* project 17
2. Severe Acute Respiratory Syndrome (SARS Co-V) project 21
3. Mouse Genomics core 23
4. Construction of gene networks models 27

Appendices

Publications 32

Introduction

In our third annual report we are providing data on our ongoing studies. We have included background data from previous reports as a link to understanding our recent data. We have made some interesting observations, and would therefore like to continue these studies.

Our hypothesis is that differential susceptibility to DoD-priority pathogens is the result of host genetic variability, and that these discrete loci and/or gene pathways can be identified using BXD recombinant inbred mice. The pathogens we are studying are naturally occurring endemic diseases, emerging infectious diseases, and potential biowarfare agents: *Leishmania major*, *Burkholderia pseudomallei*, Severe Acute Respiratory Syndrome (SARS-CoV), highly pathogenic H5N1 Avian Influenza virus, *Francisella tularensis* and multidrug resistant *Acinetobacter baumannii*.

The three main objectives of our study are:

1. To identify specific phenotypic differences in the responses of the BXD parental strains following infection with each of the DoD-priority pathogens.
2. To identify host genetic loci and pathways that correlate with the differential susceptibility/resistance phenotype(s) of the parental mouse strains to the DoD-priority pathogens.
3. To define and validate candidate genes and gene networks responsible for differential susceptibility/resistance phenotype(s) of the parental mouse strains for each DoD-priority pathogen.

In this report, we describe our research progress for a specific pathogen in relation to the proposed objectives. We have addressed these objectives to different extents for the different pathogens because the infection models for each pathogen have not developed at the same rate. For example the *Francisella*, *Burkholderia* and *Acinetobacter* are more advanced than the SARS model.
The mouse genomics core has continued to generate datasets for different mouse strains and these datasets are available on GeneNetwork. The bioinformatics core has provided an update on the Bayesian network analysis of biological data in response to infection by a pathogen.

Key research accomplishments, reportable outcomes, conclusion, references

1. Bacterial Pathogens
1.1 Studies with *Acinetobacter baumannii*

A. Overview

In the progress report from September 2010, we reported that we were having difficulty establishing pulmonary infection with *Acinetobacter baumannii* (Ab) that resulted in disease symptoms in either of the parental mouse strains. We performed a series of experiments using cyclophosphamide treatment in an effort to reduce the innate response to Ab in hopes of establishing a disease state in one or both of the parental strains. We were unable to establish symptomatic infections using this approach.

In an effort to identify a differential phenotype in the parental strains following pulmonary infection with Ab, we initiated studies to evaluate a series of immune parameters within the lung following intranasal infection with Ab. We performed time-course studies in which mice were infected with 1 x 10^6 CFU of Ab, and then a subset of the mice were sacrificed every 24 hours, bronchiolar lavage (BAL) was performed, and flow cytometric analyses was performed to determine the frequency of neutrophils within the BAL cell population.

The results of these studies have revealed that there is a significant difference in the recruitment of immune cells to the peritoneal cavity of B6 vs. D2 mice 24 hours after intranasal challenge (**Figure 1**). No differences were observed in mice sacrificed at later timepoints (data not shown). Flow cytometric analysis revealed that the bulk of the cells recruited to the lungs of D2 mice were neutrophils (data not shown).

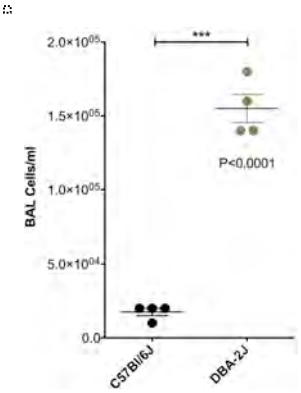

Figure 1. Differential recruitment of immune cells into the lungs following pulmonary infection with *Acinetobacter baumannii*. Mice (4/group) were challenged with either 1 x 10^6 CFU Ab via the intranasal route. The mice were sacrificed 24 hr later and bronchiolar lavage (BAL) was performed. BAL cells were counted using a hemocytometer. Statistical analysis was performed using an unpaired t-test.

We have initiated a series of studies using several lung parameters as phenotypic readouts for BXD analyses. Based on the data shown in **Figure 1**, recruitment of cell to the lungs is the one of the phenotypes of interest and is the one that we have concentrated most of our efforts on to this point. We have performed screening with 25 BXD strains (all between 10-12 weeks old) and have found that several of the BXD strains are phenotypically similar to D2 mice, some are phenotypically similar to B6 mice, and several strains display intermediate phenotypes (**Figure 2**). Some of the group sizes are too small to yield statistically relevant findings, and additional studies will be performed with these strains as mice of the appropriate age become available. Interval mapping (using GeneNetwork.org) using this cohort of animals reveals a suggestive QTL on chromosome 10 (**Figure 3**). We have established breeding cages for additional strains that will be used to continue this line of investigation and to confirm/narrow the interval on chromosome 10 that appears to correlate with the differential innate immune responses of B6 and D2 mice following *Acinetobacter* infection.

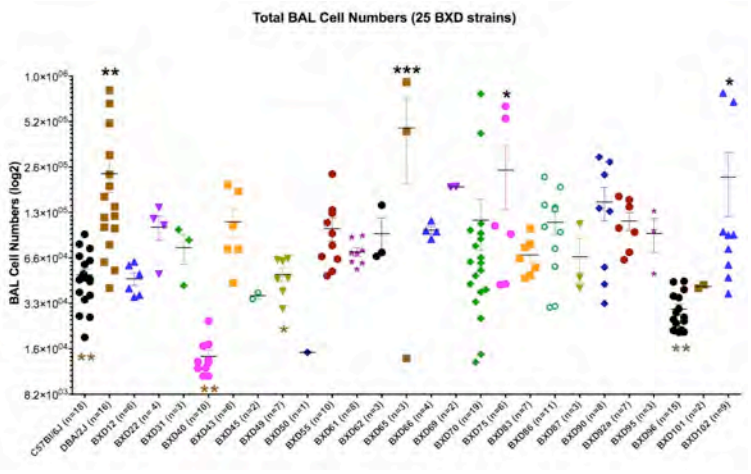

Figure 2. Differential recruitment of immune cells into the lungs of BXD strains following pulmonary infection with *Acinetobacter baumannii*. BXD mice were challenged with 1 x 10^7 CFU Ab via the intranasal route. The mice were sacrificed 24 hr later and bronchiolar lavage (BAL) was performed. BAL cells were counted using a Scepter cell counter. Statistical analysis was performed using one-way ANOVA using Dunnett post tests to compare each of the BXD strains with the C57Bl/6 (statistical significance is indicated in black) and with the DBA/2J mice (statistical significance indicated in brown). Statistical significance is as follows: p<0.05 *, p<0.01 **, and p<0.001 ***.

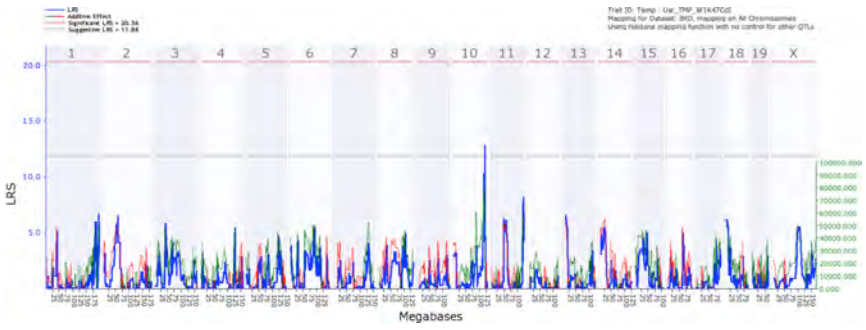

Figure 3. Interval map using recruitment of cells to the lungs of Acinetobacter-infected mice as the query phenotype. A cohort of mice which includes 25 BXD strain were infected intranasally with 1 x 10^7 CFU of Acinetobacter baumannii. Twenty-four hous later, the maice were sacrificed and bronchiolar lavage was performed on each mouse. The number of cells collected from the lungs of each mouse was determined and used as a phenotypic readout for differential innate responsiveness to *Acinetobacter*. Interval mapping was performed using the in silico resources within GeneNetwork.org. to identify genetic loci that correlate with differential recruitment of immune cells to the lungs of infected mice.

We have also been collecting bronchiolar lavage fluids (BALF) and serum samples upon sacrifice of each of the mice shown in **Figure 2**. Each of the samples will be subjected to multiplex cytokine quantitative analyses using a Luminex 32-plex cytokine/chemokine kit. Approximately half of the BALF samples have already been analyzed and it is apparent that there are significant differences in the production of a number of the analytes by the parental and BXD strains following Ab infection. In BALF samples, we have observed differences in production of 24 of the 32 analytes tested (IFN-g, IL-1a, IL-1b, IL-2, IL-4, IL-3, IL-6, G-CSF, IL-9, IL-10, IL-12p40, IL-12p70, LIF, IL-13, LIX, IL-15, IL-17, IP-10, KC, M-CSF, MIP-2, MIG, VEGF, TNF-a). Interval mapping of these differential cytokine/chemokine phenotypes have identified several QTL that correlate with differential expression of many of these cytokines. The most commonly observed QTLs are on chromosomes 5 (centered at approximately 100Mb) and 6 (centered at approximately 26Mb). As shown in **figure 4**, either significant or suggestive QTLs were observed for each of the cytokines at a similar region of chromosome 5, and suggestive QTLs were observed at a similar region of chromosome 6 for four of the six cytokines shown.

Figure 4. Interval mapping of a panel of differentially expressed cytokines/ chemokines. Interval mapping was performed using the in silico resources within GeneNetwork.org to identify genetic loci that correlate with differential disease-state expression of IL-5, IL-6, IL-10, IL-12p70, IL-15, and M-CSF in the lungs of *Acinetobacter*-infected mice.

We surveyed the genes that are within the suggested interval of chromosome 5 in an effort to identify genes that have obvious roles in the production of immune responses (**Figure 5**). Many of the prospective genes that were identified are likely to play a role in innate resistance to bacterial pathogens. For example, Cmklr1, a genetic locus on chromosome 5, encodes chemokine-like receptor-1. This receptor is expressed on a number of immune cells including plasmacytoid dendritic cells, myeloid dendritic cells, macrophages, and NK cells [1]. After activation of this receptor, these cells synthesize and secrete a number of proinflammatory cytokines, including IL-6 and TNFα [2]. Activation of this receptor

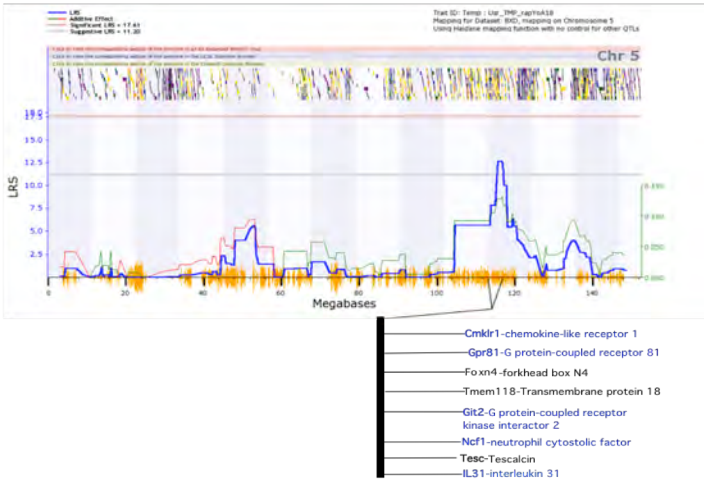

Figure 5. Identity of host genes encoded within the suggestive QTL on chromosome 5 that may be potentially involved in immune processes. Genes that are potentially involved in immune processes are listed in blue.

causes initiation of signaling cascades such as ERK1 and NF-kB [3].
Gpr81, which encodes G-protein coupled receptor (GPCRs) 81, was also found within the loci of the suggestive QTL on chromosome 5. GPCRs are expressed on inflammatory cells such as polymorphonuclear leukocytes, monocytes and macrophages for classic chemoattractants and chemokines. These receptors also play a crucial role in the migration of phagocytes to sites of inflammation[4].
Other genes of interest that lie within this locus encode the IL-31 receptor and neutrophil cytostolic factor (IL-31r and NCF1respectively). The IL-31 receptor is expressed on a number of cell types including monocytes, epithelial cells and T cells and has role in limiting type 2 inflammation in the lung [5, 6]. NCF1 encodes neutrophil cytostolic factor (p47hox). This protein has been implicated as a regulator for IL-4 signaling pathways that are important for macrophage cell fate choice. Furthermore, this protein is a subunit of the NADPH oxidase enzyme complex, which plays an essential role in the function of phagocytes [7].
Genes of interest within the interval identified on chromosome 6 (**Figure 6**) include Irf5, which encodes the protein interferon regulatory factor 5. This protein binds to specific regions of DNA that regulate the activity of genes that produce interferons and other cytokines. Irf5 has also been shown to stimulate the activity of natural killer cells [8]. Another gene of interest within this QTL is NRF1 (Nuclear respiratory factor-1) gene that is an early phase component of the host antibacterial defenses [9].

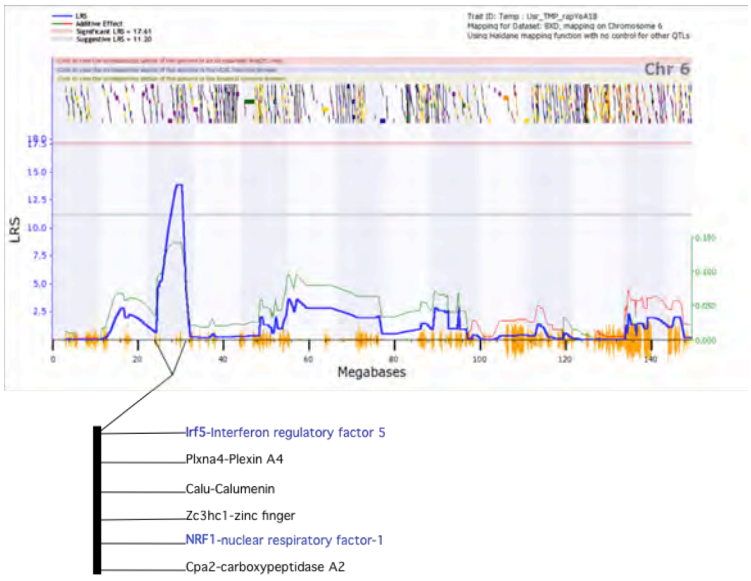

Figure 6. Identity of host genes encoded within the suggestive QTL on chromosome 6 that are potentially involved in immune processes. Genes that are potentially involved in immune processes are listed in blue.

Linkage analysis of several other cytokine phenotypes identified suggesting QTLs on chromosome 12 (**Figure 7**), significant and suggestive QTLs of chromosome 15 (**Figure 8**), and a significant QTL on chromosome 19 (**Figure 9**). Genes within the

Figure 7. Interval mapping of a differentially expressed cytokines/ chemokines. Interval mapping was performed using the in silico resources within GeneNetwork.org to identify genetic loci that correlate with differential disease-state expression of TNF-alpha, MIP-2, and G-CSF in the lungs of *Acinetobacter*-infected mice.

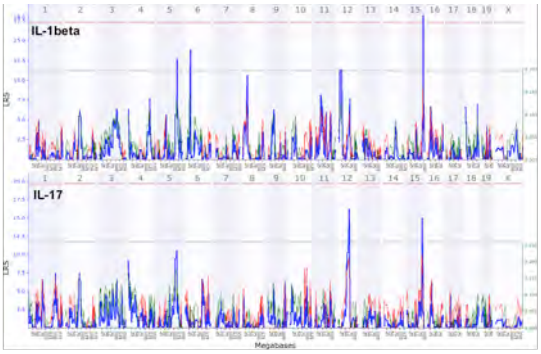

Figure 8. Interval mapping of phenotypic data from differentially-expressed cytokines/ chemokines. Interval mapping was performed using the in silico resources within GeneNetwork.org to identify genetic loci that correlate with differential disease-state expression of IL-1beta and IL-17 in the lungs of *Acinetobacter*-infected mice.

Figure 9. Interval mapping of phenotypic data from differentially-expressed cytokines/ chemokines. Interval mapping was performed using the in silico resources within GeneNetwork.org to identify genetic loci that correlate with differential disease-state expression of IL-1alpha and LIX in the lungs of *Acinetobacter*-infected mice.

identified interval on chromosome 19 (**Figure 10**) that are of immediate interest include secretoglobin, and T-cell immune regulator (Tcirg1). Secretoglobins modulate inflammatory and immunologic responses to the environment at mucosal surfaces and inside the body and are associated with increased bronchial inflammation [10]. This multi-functional protein with anti-inflammatory/immunomodulatory properties has been implicated to have a homeostatic role against oxidative damage, inflammation, autoimmunity and cancer [10, 11]. Tcirg1 is a membrane protein that is induced after immune activation on the surface of certain peripheral human T and B cells as well as monocytes and IL-10 expressing T-cells. This gene has implicated in inhibiting T-cell proliferation by modulation of CTLA-4 expression [12]; of course, this function is unlikely to have any role in the innate response to *Acinetobacter*. Loci included the significant QTL region on chromosome 19 also encode several G-protein coupled receptors that as previously stated, are important for the migration of phagocytes.

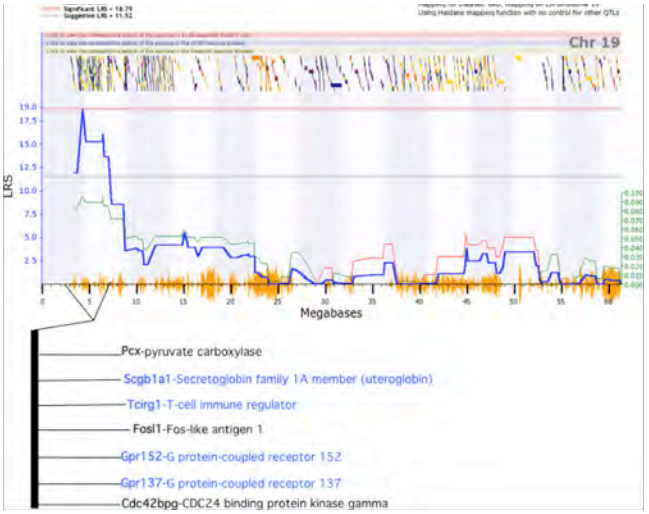

Figure 10. Identity of host genes encoded within the suggestive QTL on chromosome 19 are potentially involved in immune processes. Genes that are potentially involved in immune processes are listed in blue.

Dr. Cui has performed a preliminary analysis of these data (only 17 BXD strains) and has identified a significant correlation between the levels of a number of these cytokines (**Figure 11**) and has identified three genetic genomic locations [Chr 6 near 65 Mb (mCV22576656), Chr 14 near 43 Mb (rs13482156), and Chr 19 near 51 Mb (rs3716572)] that each impact the level of several cytokines. We performed principal components analysis of the cytokines with an absolute correlation greater than 0.7 for the three loci and mapped the first principal component of each of the groups of cytokines (**Figure 12**). The first principal component of each of the sets of cytokines has a significant or highly suggestive QTL at the marker location. Several genes at these

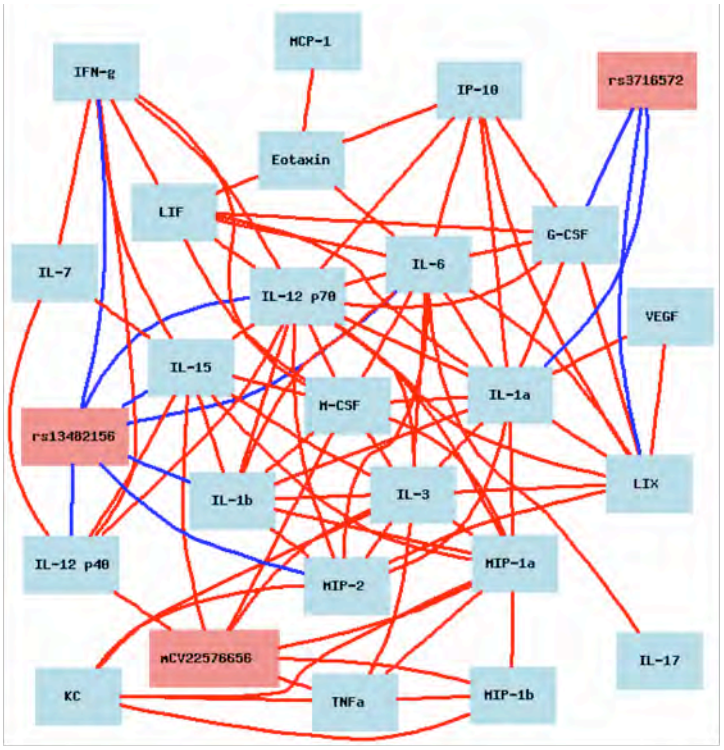

Figure 11. Correlation network for cytokine levels in the BALF of BXD strains infected with *Acinetobacter baumannii*. Three genotype markers (red boxes) on chromosomes 6, 14, and 19 are highly correlated with several cytokines. Pearson's correlation coefficient greater than 0.7 (solid lines) are shown.

Figure 12. QTL mapping of first principal component for cytokines correlated (Pearson correlation coefficient > 0.7) with mCV22576656 (top), rs13482156 (middle), and rs3716572 (bottom).

three loci, including a cluster of immunoglobulin kappa (IGK) genes on Chr 6, *Mbl1* and *Bmp4* on Chr 14, and *Nfkb2* on Chr 19, have been previously associated with immune responses. These locations are promising starting points for developing network models that explain variation in response to infection with *Acinetobacter*. We have also begun to analyze serum samples collected from this cohort of mice (13 strains) and have observed differences in the levels of 14 of the analytes tested (eotaxin, G-CSF, IFN-g, IL-1a, M-CSF, IL-6, IL-13, KC, LIX, MIP-1a, MIP-1b, RANTES, and TNFa). Preliminary analyses of these data suggest that the loci on Chr 6 (mCV22576656) and Chr 14 (rs13482156) that were shown to influence the levels of cytokines in the BALF are also correlated with cytokine levels in the serum (**data not shown**).

We have also begun to analyze serum samples collected from this cohort of mice and have observed differences in the levels of 14 analytes of the analytes tested (eotaxin, G-CSF, IFN-g, IL-1a, M-CSF, IL-6, IL-13, KC, LIX, MIP-1a, MIP-1b, RANTES, and TNFa; **data not shown**). In summary, we have identified 38 phenotypes that may be useful in our search for host genetic elements that lead to differential innate immune responsiveness of B6 vs. D2 mice following infection with *Acinetobacter baumannii*.

B. Key Research Accomplishments:

- We have confirmed that B6 and D2 mice produce differential innate immune responses to pneumonic Ab infection
- We have identified a suggestive QTL on chromosome 10 that appears to correlate with the differential recruitment of immune cells to the lungs in response to pneumonic *Acinetobacter* infection.
- We have identified putative QTL's (chromosomes 5, 6, and 19) that correlate with a disease-state expression of a series of cytokines/chemokines in the lung compartment of *Acinetobacter*-infected.
- We have identified 38 total phenotypes that include cell recruitment to the lungs, differential expression of 24 cytokines/chemokines in the lung compartment, and 14 cytokine/chemokines that are differentially expressed in the circulation (serum) of acutely infected mice.

C. Reportable outcomes:

Emery F., Parvathareddy J., Van Hoang K., **Cui Y**., **Williams R.W**., and **Miller M.A**. 2012. Quantitative trait loci that correlate with differential innate immune responses produced by mice suffering from acute pulmonary *Acinetobacter baumannii* infection. PLoS One (manuscript in preparation).

D. Conclusions:

We have identified a large number of clear phenotypic differences between the innate responsiveness of B6 and D2 mice to pulmonary infection with *Acinetobacter baumannii*. We have initiated studies in a cohort of BXD strains and hope to identify host genes that correlate with the differential responsiveness of the parental strains to *Acinetobacter*. Although we have only completed analyses of relatively few BXD strains, we have already identified a significant correlation between several cytokines produced in the lungs and the differential responsiveness of B6 vs. D2 mice to *Acinetobacter* infection. Moreover, we have preliminarily identified a genetic locus on chromosome 10 that correlates with differential recruitment of immune cells to the lungs and four loci (on chromosomes 5, 6, 12, and 19) that appear to correlate with differential production of a number of cytokines/chemokines following pneumonic infection. Identification of this large panel of queriable phenotypes will allow for very interesting network modeling that has potential to identify gene networks that are involved in a variety of innate immune responses to *Acinetobacter* infection.

E References:

1. Zabel, B.A., A.M. Silverio, and E.C. Butcher, *Chemokine-like receptor 1 expression and chemerin-directed chemotaxis distinguish plasmacytoid from myeloid dendritic cells in human blood.* Journal of immunology, 2005. 174(1): p. 244-51.

2. Zabel, B.A., et al., *Chemokine-like receptor 1 expression by macrophages in vivo: regulation by TGF-beta and TLR ligands.* Experimental hematology, 2006. 34(8): p. 1106-14.
3. Bondue, B., et al., *ChemR23 dampens lung inflammation and enhances anti-viral immunity in a mouse model of acute viral pneumonia.* PLoS pathogens, 2011. 7(11): p. e1002358.
4. Sun, L. and R.D. Ye, *Role of G protein-coupled receptors in inflammation.* Acta Pharmacol Sin. 33(3): p. 342-50.
5. Perrigoue, J.G., et al., *IL-31-IL-31R interactions negatively regulate type 2 inflammation in the lung.* The Journal of experimental medicine, 2007. 204(3): p. 481-7.
6. Perrigoue, J.G., et al., *IL-31-IL-31R interactions limit the magnitude of Th2 cytokine-dependent immunity and inflammation following intestinal helminth infection.* Journal of immunology, 2009. 182(10): p. 6088-94.
7. Yi, L., et al., *p47(phox) directs murine macrophage cell fate decisions.* The American journal of pathology, 2012. 180(3): p. 1049-58.
8. Paun, A., et al., *Functional characterization of murine interferon regulatory factor 5 (IRF-5) and its role in the innate antiviral response.* The Journal of biological chemistry, 2008. 283(21): p. 14295-308.
9. Suliman, H.B., et al., *Co-regulation of nuclear respiratory factor-1 by NFkappaB and CREB links LPS-induced inflammation to mitochondrial biogenesis.* Journal of cell science, 2010. 123(Pt 15): p. 2565-75.
10. Heinzmann, A., *Association of uteroglobulin-related protein 1 with bronchial asthma.* Int. Arch. Allergy Immunology, 2003. 131(4): p. 291-295.
11. Chiba, Y., T. Kusakabe, and S. Kimura, *Decreased expression of uteroglobin-related protein 1 in inflamed mouse airways is mediated by IL-9.* American journal of physiology. Lung cellular and molecular physiology, 2004. 287(6): p. L1193-8.
12. Bulwin, G.C., et al., *TIRC7 inhibits T cell proliferation by modulation of CTLA-4 expression.* Journal of immunology, 2006. 177(10): p. 6833-41.

1.2 Studies with *Burkholderia pseudomallei*

1.2.1 Identification of host genes that correlate with differential susceptibility/resistance to infection

A. Overview

Our initial studies with a pneumonic *Burkholderia* challenge model (intranasal instillation) confirmed the previously published observation that B6 mice are more resistant than D2 mice to Bp infection. We found that following intranasal instillation of 50 CFU of Bp strain 1026b, D2 mice typically succumbed to infection by day 4 post-infection while B6 mice survived the infection. Subsequent studies showed that the same results were obtained with challenge doses of up to 200 CFU/mouse.

Based on these findings, we initiated forward genetics studies with a cohort of BXD strains in an effort to identify host genetic loci that correlate with the differential susceptibility observed in the parental strains. We screened a cohort of 35 BXD strains for susceptibility to pneumonic Bp infection. Groups of male mice were challenged with 50-100 CFU of Bp (from a diluted frozen stock) via intranasal instillation and then monitored for weight retention and survival. B6 and D2 mice were included in each of the 19 experiments that have been performed, and the D2 mice were always the last group to be challenged to ensure the "potency" of the challenge stock throughout the instillation process. We found that several of the BXD strains were highly susceptible to Bp (similar to D2 mice), others were relatively resistant to Bp (similar to B6 mice), and several strains displayed intermediate phenotypes (**Figure 13A**). Interval mapping (see GeneNetwork.org) using this cohort of animals revealed a significant QTL on chromosome 5 and suggestive QTLs on chromosomes 7 and 14 (**Figure 13B**) that correlated with differential susceptibility/resistance to Bp.

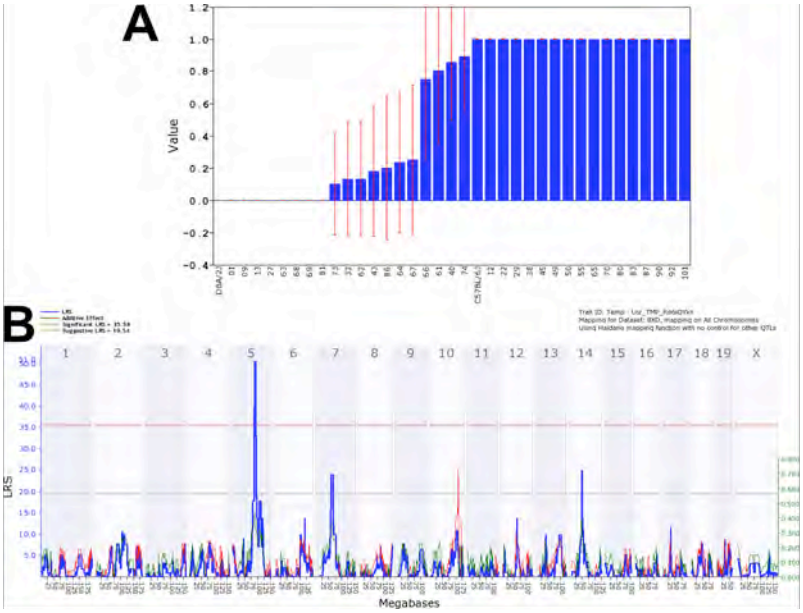

Figure 13. Interval map using survival of pneumonic challenge with *Burkholderia pseudomallei* as the query phenotype. A cohort of male mice which included 35 BXD strains was infected intranasally with 50-100 CFU of *Burkholderia pseudomallei*. Infected mice were monitored for survival for up to 11 days post-infectionand those that survived infection were given a value of "1" while those that succumbed to infection received a value of "0" (**Panel A**). Interval mapping was performed using the *in silico* resources within GeneNetwork.org to identify genetic loci that correlated with survival (**Panel B**).

Another disease-state phenotype that may prove useful in understanding the host response to Bp infection is weight retention two-days post-challenge. Linkage analysis of weight retention in male mice following pneumonic challenge with Bp identified a highly suggestive QTL on chromosome 15 that correlates with the differential in weight retention that was observed in the parental and BXD mouse strains (**Figure 14**).

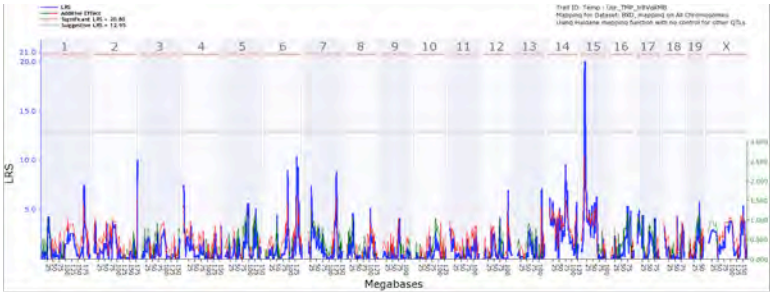

Figure 14. Interval map using weight retention following pneumonic challenge with *Burkholderia pseudomallei* as the query phenotype. A cohort of male mice which included 35 BXD strains was infected intranasally with 50-100 CFU of *Burkholderia pseudomallei*. Infected mice were monitored for weight retention for up to 11 days post-infection. Interval mapping was performed using the *in silico* resources within GeneNetwork.org to identify genetic loci that correlated with survival.

Interestingly, females from several of the BXD strains as well as female D2 mice were significantly more resistant to pneumonic Bp infection that their male counterparts. Linkage

analysis of survival data from female mice yields very different results from those obtained using data from male mice. Several peaks are observed, none of which are even considered suggestive QTLs. Moreover, inclusion of survival data from both male and female mice for linkage analysis results in an inability to identify QTLs that correlate with survival/resistance to Bp infection (**Figure 15**) We are hopeful that identification of additional strains with this differential sex-related phenotype will lead to identification of correlating host genetic factor(s).

We have also initiated studies to identify additional Bp disease-state phenotypic differences between the parental strains. Parental mice were challenged with 100 CFU via intranasal instillation and then sacrificed 24 hours later for collection of blood serum and brochoalveolar lavage. BAL cells and BAL fluids/serum were collected from each mouse and subjected to flow cytometric analysis and multiplex cytokine/chemokine analysis (32-plex), respectively. Neutrophil recruitment was significantly higher (p=0.03) in D2 mice (compared to B6; data not shown). Multiplex cytokine analysis identified six analytes from the BALF and five analytes from the serum whose Bp disease-state levels were significantly different between the two parental mouse strains (**Figure 16**). Similar preliminary studies with a cohort of BXD strains suggested that we will be able to exploit these additional phenotypes as well as some additional lung cell phenotypes and cytokine/chemokine phenotypes (data not shown) for forward genetic analyses.

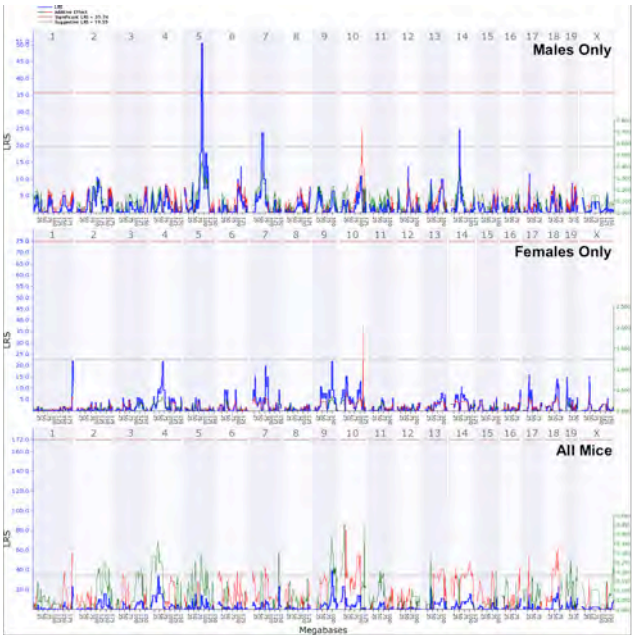

Figure 15. Differential susceptibility of male vs. female mice to pneumonic Bp infection. Survival of BXD mice challenged intranasally with 100 CFU Bp was monitored and linkage analyss was performed on male, female, and all mice as indicated in the upper right of each panel.

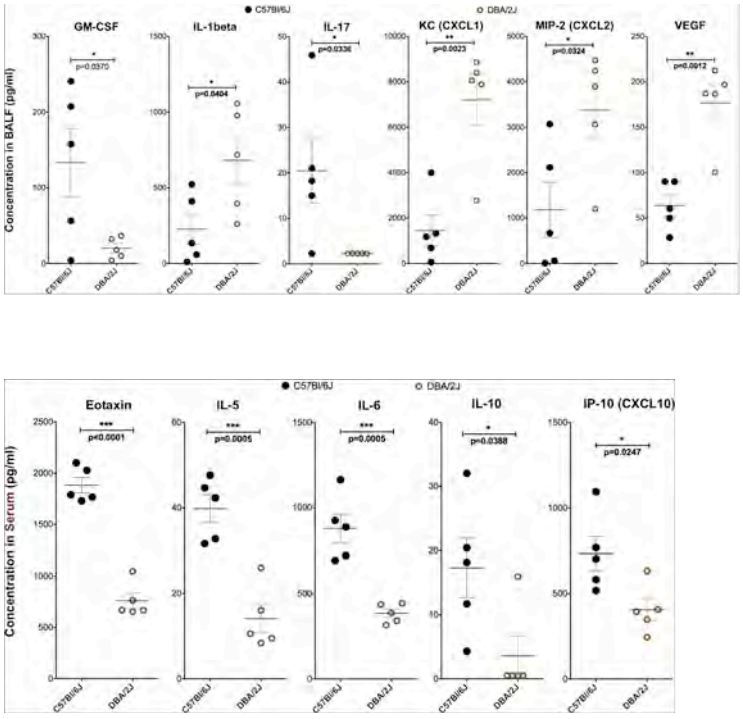

Figure 16. Differential disease-state cytokine expression in the lung compartment and in the peripheral circulation during acute *Burkholderia* infection of BXD parental mouse strains. BXD mice were challenged with 100 CFU Bp strain 1026b via the intranasal route, sacrificed 24 hr later, and bronchoalveolar lavage (BAL) and serum collection was performed. Multiplex cytokine/chemokine analysis (32-plex) was performed on BAL fluids (**Top Panel**) and serum samples (**Bottom Panel**). Statistical analysis was performed using unpaired student-t tests. Statistical significance is as follows: p<0.05 *, p<0.01 **, and p<0.001 ***.

Based on these findings with the parental strains, we have initiated studies in which we are measuring disease-state lung parameters, such as immune cell recruitment to the lungs (bronchoalveolar lavage cells or BAL cells) and cytokine/chemokine expression in the lungs (BAL fluids or BALF) and peripheral circulation (blood serum), 24-hours post-infection (intranasal instillation).

To monitor the frequency of neutrophils ($CD11b^+$ / $GR1^+$), alveolar macrophages ($CD11c^+$ / $F4/80^+$ / $CD205^+$), interstitial macrophages ($F4/80^+$ / $CD11b^+$), g/d T cells (g/d TCR^+), and NK cells ($NKGA/C/E^+$) recruited to the lungs as well as the activation status of the macrophage cell types (MHC class II expression levels / $I\text{-}A/I\text{-}E^+$), BAL cells are subjected to eight-color flow cytometric analysis after staining with the following marker-specific

flourochrome conjugates: Ly6G-Ly6C-Horizon-V450, CD11b-Horizon-V500, I-A/I-E-FITC, gamma/delta TCR-PE, NKGA/C/E-PerCP-eFluor 710, CD205 (DEC205)-PE-Cy7, CD11c-APC, and F4/80-APC-Alexa Fluor 750. We have observed differences in each of these parameters in the parental strains as well as the randomly selected BXD strains studies to date. For example, the frequency and activation status (MHC surface density) of both interstitial and alveolar macrophages vary widely between different strains of mice (**Figure 17**). Linkage analyses of these data reveal a suggestive QTL on chromosome 16 correlating with frequency of interstitial macrophages (male mice only). Additional BXD strains and additional numbers of many of the strains shown in **Figure 5** must be performed before fruitful linkage analysis can be performed with each of these parameters. We have also begun to measure the concentrations of cytokines/chemokines in the BALF collected from these mice via 32-plex Luminex analyses. We are at various stages of analyzing these data. Clearly, there are differences amongst the parental and BXD strains for many of the analytes we have measured, and preliminary linkage analysis using these analytes as query phenotypes have identified suggestive QTLs correlated with differential cytokine expression (data not shown). Clearly, more BXD strains are needed for these analyses (and we are continuing to add strains as they become available though our breeding program), and due to the relatively high degree of biological variability that is associated with these measurements we will need to reach our goal of 10 mice/sex/strain before we expect to have high confidence in the resulting linkage analysis.

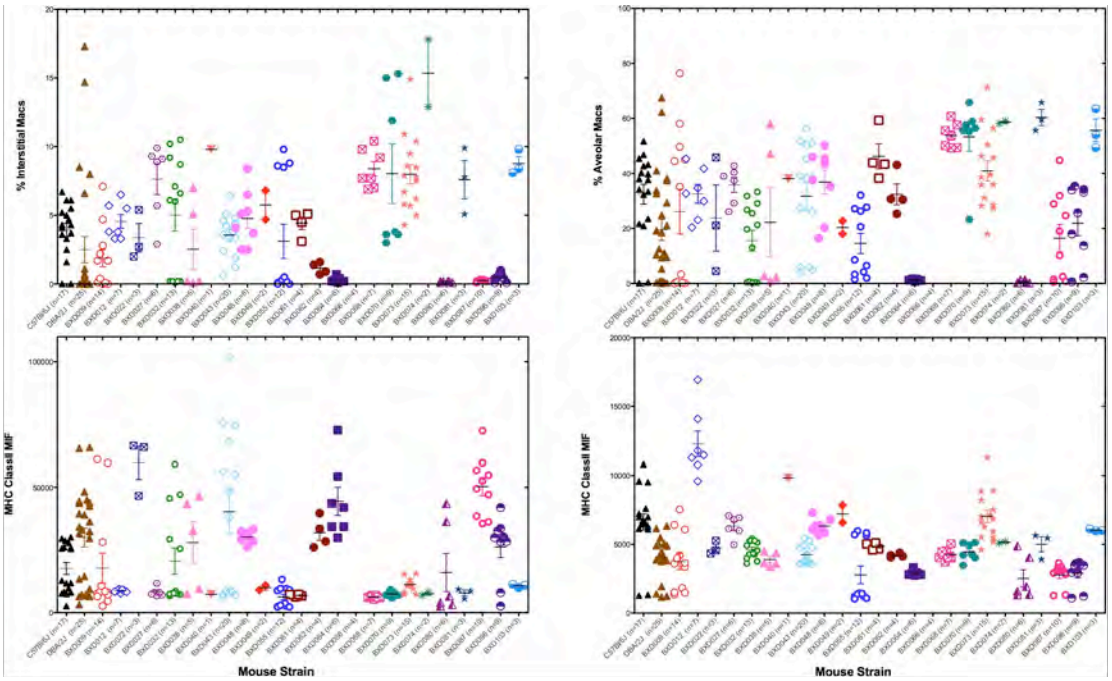

Figure 17. Differential frequency and activation status of interstitial and alveolar macrophages in the lungs of Bp-infected mice. Parental and randomly-selected BXDs strains were challenged intranasally with 100 CFU Bp and sacrificed 24 hours later. Flow cytometric analysis of BAL cells was performed to determine the frequency of interstitial macrophages (upper left panel) and alveolar macrophages (upper right panel) as well as the activation status (MHC class II expression density) of both cell types (lower panels). These plots show data from both male and female mice and no statistical analyses have been performed.

B. Key Research Accomplishments

- We have identified one highly significant QTL and two suggestive QTLs that correlate with differential susceptibility of mice to pneumonic *Burkholderia pseudomallei* infection. Screening of additional BXD strains that have recombinations within the intervals of these three QTLs will allow us to increase the precision of QTL mapping significantly, helping us to identify specific candidate genes that correlate with differential susceptibility to *Burkholderia*.
- We have clearly shown that there are sex-based differences in susceptibility to pneumonic Burkholderia infection (female mice generally appear to be more resistant to this pathogen).
- Using parental strain we have identified at least eleven additional phenotypes that will allow fruitful linkage analysis (once the number of strains and N-numbers are increased) that will allow us to perform computer modeling studies that are designed to identify gene networks that are critical for various innate immune as well as susceptibility/resistance to *Burkholderia* infection.
- We have generated preliminary data using measurements of disease-state cytokines/chemokine production and innate immune cell frequencies/activation status in the lungs of acutely infected parental

and BXD mice. These preliminary data indicate that the phenotypes identified using parental mice (as well as several others) will be useful for QTL analyses.

C. Reportable Outcomes

Publications:

Ceballos-Olvera, I., Sahoo, M., **Miller, M.A**., del Barrio, L., and **Re F**. 2011. Inflammasome-dependent pyroptosis and IL-18 protect against *Burkholderia pseudomallei* lung infection while IL-1b is deleterious detrimental. *PLOS Path*. 7(12): e1002452. *PMID- 22241982*

Miller, M.A., Parvathareddy, J., Emery, F., Van Hoang, K., **Cui, Y**., and **Williams, R.W. 2012**. Identification of quantitative trait loci correlating with differential susceptibility of mice to pneumonic *Burkholderia pseudomallei* Infection. PLoS One (manuscript in preparation).

D. Conclusions

Using survival as a phenotype for linkage analyses to identify host loci that correlate with differential susceptibility/resistance of mice to pneumonic *Burkholderia pseudomallei* infection has been successful. Survival of acute pneumonic *Burkholderia* infection is a complex trait in mice that appears to involve at least three different host loci (on chromosomes 5, 7, and 14). We have not identified any specific host genes that involved, but we now are able to select BXD strains (or collaborative cross strains) that have recombinations within these three loci to narrow the interval (and the candidate gene pool). We have also identified a number of additional phenotypes that include weight retention, immune cell frequency/activation status in the lungs, and cytokine/chemokine expression in the lungs of acutely infected mice. Once the “lung parameter” studies have been completed on 30-35 strains, we expect to have at least 15 phenotypes that will be useful for identifying QTLs that correlate with differential innate responsiveness of the parental mouse strains. Network modeling of using these data will allow us to identify host gene networks that enable mice to survive acute pneumonic *Burkholderia pseudomallei* infection.

1.2.2 Studies on cellular pathways responsible for genetic susceptibility to *Burkholderia pseudomallei* infection

Our recently published results indicate that excessive inflammation instigated by IL-1 is deleterious in melioidosis. Accordingly, inhibition of the inflammatory response reduced mortality and morbidity. We have now explored different approaches to reduce the innate immune response to infection with *B. pseudomallei* with the expectation that it would increase resistance to this pathogen. For example, we have found that intranasal administration of LPS and the neutrophil chemoattractant fMLP 48 hours before infection protected mice from infection with lethal doses of *B. pseudomallei* (**figure 1**).

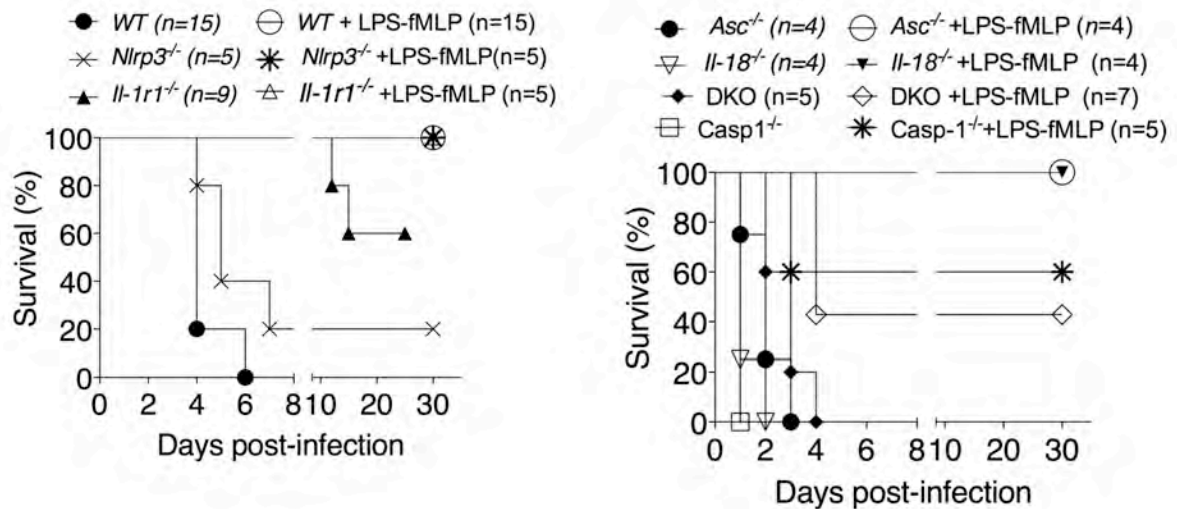

Figure 1. LPS+fMLP protect from lethal doses of *B. pseudomallei*. Mice were pre-exposd to LPS (100 mg)72 hrs and fMLP (20 nM) 48 hrs before intranasal infection with lethal doses of B. pseudomallei. WT, *Il-1r1*$^{-/-}$*, Nlrp3*$^{-/-}$ mice were infected with 250 CFU. *Asc*$^{-/-}$*, Il-18-/-, Il-1r1/Il-18* DKO, *Casp-1*$^{-/-}$ mice 30 CFU).

C57 BL/6 (WT), C57 with Nlrp3 inflammasome knock out (Nlrp3$^{-/-}$), C57 IL-1 receptor 1 knock out (Il-1r1$^{-/-}$), C57 Asc knock out (Asc$^{-/-}$), and C57 IL-18 knock out (Il-18$^{-/-}$) were all protected by the LPS/fMLP pretreatment relative to similarly infected, untreated mice. The pretreatment was less effective in C57 IL-1 receptor 1/ IL-18 double knock out (DKO) and C57 Caspace 1 knock out (Casp1$^{-/-}$) mice. Each of the gene knock outs eliminated one or more inflammasome or inflammatory cytokine components of the innate/inflammation response to bacterial infection. This treatment resulted in lower production of inflammatory cytokines, lower recruitment of neutrophils to the lung (as measured by MPO content in BALF), and lower bacterial burden in organs (**figure 2**).

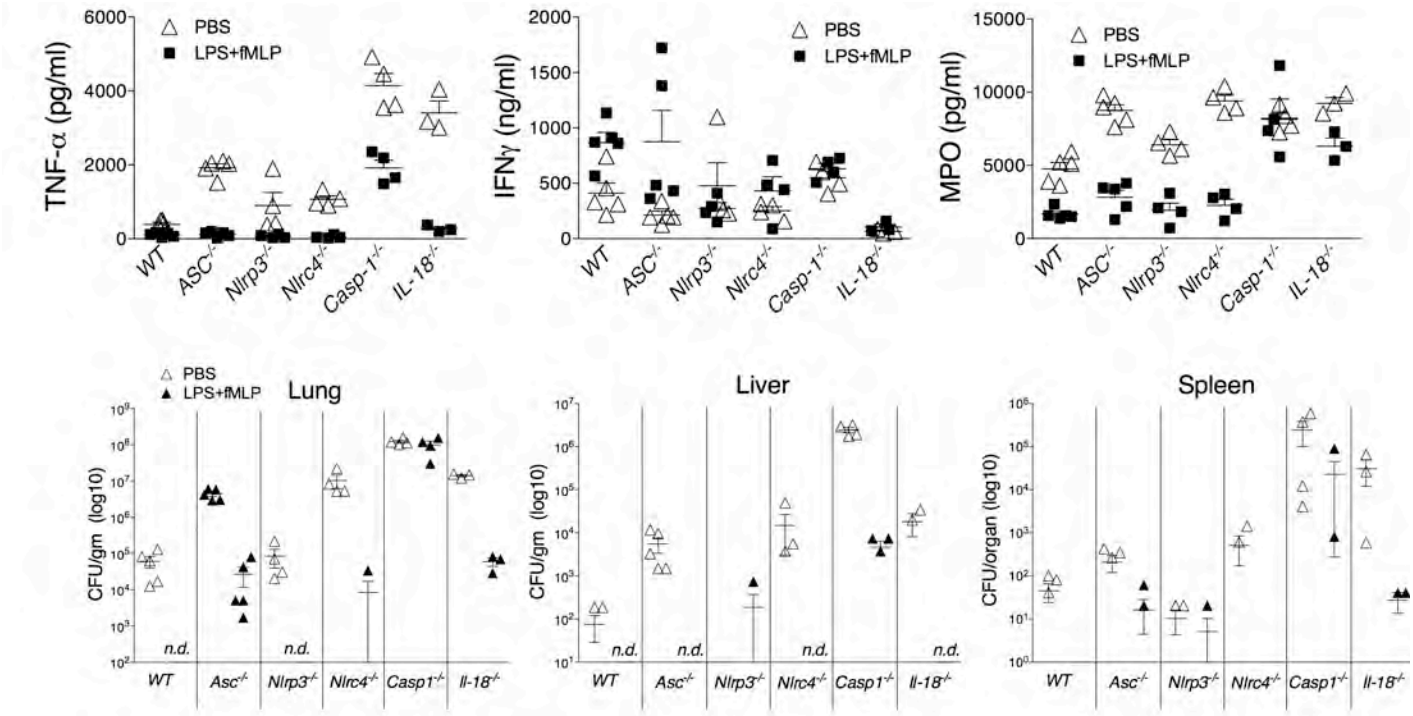

Figure 2. LPS+fMLP protect from lethal doses of *B. pseudomallei*. Mice were pre-exposed to LPS (100 mg) and fMLP (20 nM) 48 hours before infection and then intranasally infected with lethal doses of *B. pseudomallei*. Mice were sacrificed 48 hours postinfection and cytokine levels in BALF and bacteria burden in organs were measured.

Various mechanisms may account for this protective effect. It is conceivable that LPS pre-exposure renders mice tolerant to endotoxic shock during infection. LPS administration is also increasing IFNg production in response to infection. Finally, LPS treatment diminishes recruitment of neutrophils to the lung. Our future experiments will determine which of these mechanisms is responsible for the protection.

1.3 Studies with *Francisella tularensis*

A. Overview

Francisella tularensis Schu S4 is an extremely virulent bacterial pathogen in humans (LD_{50}<10 CFU) and in all mouse strains that have been studied (LD_{50}<10). In our hands, there is very little difference in the ultimate outcome of infection of the two parental mouse strains (B6 and D2); the mice all die and at very similar rates. However, we and others have observed differences in the bacterial burdens that are observed in B6 vs. D2 mice. It is known that B6 mice typically carry 5-10 fold higher FT burdens than D2 mice during acute infection. It stands to reason that these two mouse strains produce distinct innate immune responses that are responsible for this difference in bacterial burdens.

In an effort to identify phenotypes of differential innate immune responsiveness of B6 vs. D2 mice to pneumonic *Francisella tularensis* Schu S4 (FT) infection, we performed a timecourse study of disease-state lung parameters following pneumonic infection. Mice were challenged with 250 CFU of FT via intranasal instillation. At each of the following timepoints (12, 18, 24, 48, 72, 96, and 120 hours) post-infection, 5 mice/group were subjected to submandibular puncture for blood collection and were then sacrificed. Immediately after sacrifice, brochoalveolar lavage was performed using 1 ml of sterile PBS, cells were pelleted via centrifugation, BAL cells were enumerated using a Millipore Sceptor automatic cell counter, and BALF fluids were stored at 80˚C until use. Cytokine/chemokine quantitation in each BAL fluid was then performed via Luminex-based multiplex analysis (32-plex Millipore kit).

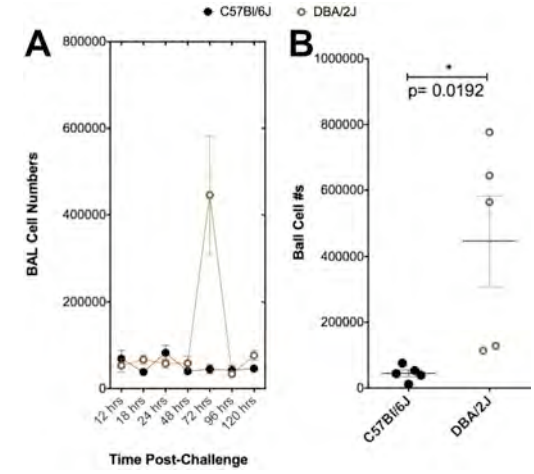

Figure 1. Differential expression of cytokines in the lung compartment of *Francisella tularensis* Schu S4-infected B6 and D2 mice. B6 and D2 mice (35/group were challenged via intranasal instillation with 250 CFU FT Schu S4. On day three (72 hrs) post-infection, 5 mice/group were sacrificed and bronchoalveolar lavage (BAL) was performed. Cytokine/chemokine quantitations in BAL fluids were performed via Luminex-based multiplex analysis (32-plex Millipore kit). Statistical analyses were performed using student-t tests and p values are indicated.

We found that on day 3 post-infection (72 hrs), cells numbers recruited to the lungs of D2 mice were significantly higher than observed in B6 mice (**Figure 1**). Interestingly, this difference in BAL cell numbers was transient.

Multiplex cytokine analysis of BALF revealed that most of the cytokine and chemokine levels remained relatively flat in the lungs of both B6 and D2 mice for the first two days of acute infection. However, on day three significant increases in levels of several cytokines were observed in the lungs of either B6, D2, or both strains. Differential expression of 10 analytes (M-CSF, G-CSF, IL-1alpha, IL-6, IL-12p40, IL-17, LIF, RANTES, KC, and VEGF) was observed on day 3 post-infection (also see **Figure 2** and **Figure 3**). On day 4 post-infection there were 11 analytes that appear to be differentially expressed in B6 vs. D2 mice (M-CSF, G-CSF, IL-6, IL-12p70, IL-17, LIF, KC, VEGF, MIP-2, MCP-1, and MIG) and on day 5 post infection 10 of the analytes were differentially expressed by B6 vs. D2 mice (M-CSF, G-CSF, IL-1alpha, KC, VEGF, MIP-2, MIG, Eotaxin, MIP-1alpha, and MIP-1beta).

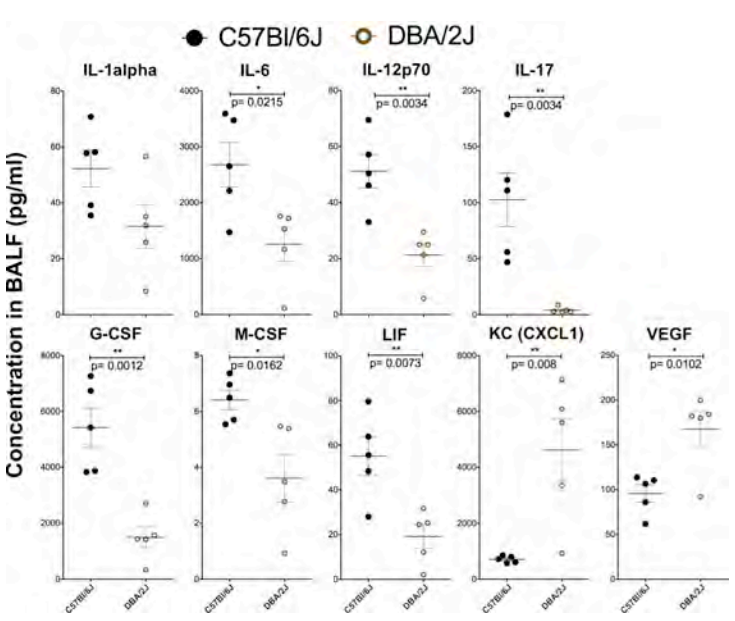

Figure 2. Differential expression of cytokines in the lung compartment of *Francisella tularensis* Schu S4-infected B6 and D2 mice. B6 and D2 mice (35/group were challenged via intranasal instillation with 250 CFU FT Schu S4. On day three (72 hrs) post-infection, 5 mice/group were sacrificed and bronchoalveolar lavage (BAL) was performed. Cytokine/chemokine quantitations in BAL fluids were performed via Luminex-based multiplex analysis (32-plex Millipore kit). Statistical analyses were performed using student-t tests and p values are indicated.

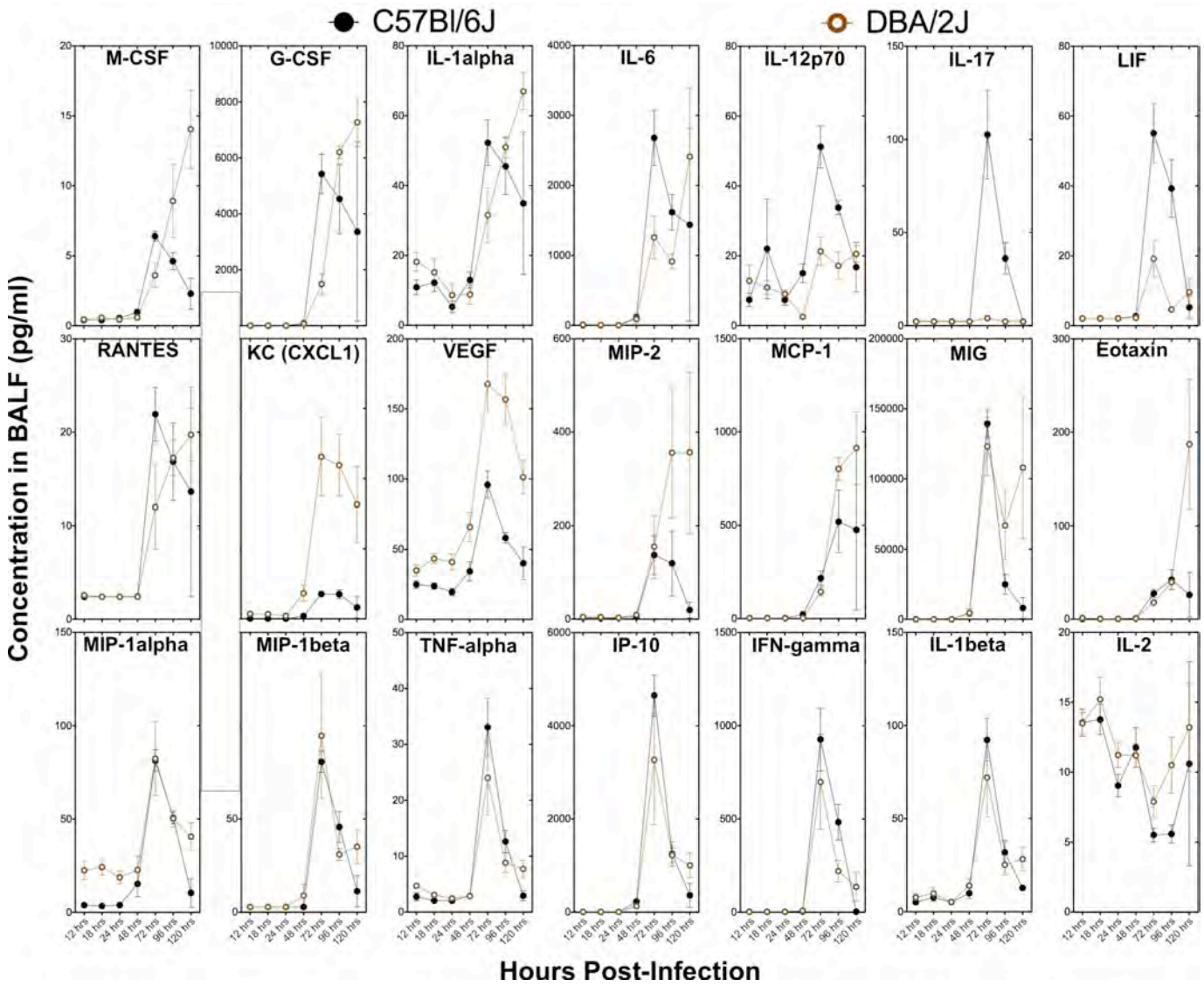

Figure 3. Kinetic monitoring of cytokine/chemokine production in the lung compartment of B6 and D2 mice following pneumonic challenge with *Francisella tularensis* Schu S4. B6 and D2 mice (35/group) were challenged via intranasal instillation with 250 CFU FT Schu S4. At the indicated time points (12, 18, 24, 48, 72, 96, and 120 hrs post-infection), mice were sacrificed and bronchoalveolar lavage was performed. Quantitation of cytokine/chemokine levels in the BAL fluids was performed via Luminex-based multiplex analysis (32-plex Millipore kit).

We also analyzed serum samples via Luminex-based cytokine/chemokine multiplex analysis (32-plex Millipore kit). Similar to our findings with the BALF, most of the cytokine levels remained fairly flat until three days post-infection. At this timepoint, a significant elevation in concentration of many of the cytokines was apparent in serum of either B6, D2, or both strains (**Figure 4**). However, in contrast to what was observed in the BALF, there were only six analytes that appeared to be differentially expressed (IL-1beta, IL-6, IL-12p70, IL-17, MIP-1alpha, and IL-10), and only 4 of those were statistically relevant differences (**Figure 5**). Interestingly, only three of the six analytes that were differentially expressed in the serum were found to be differentially expressed in the lung compartment. On day 4 post-infection, 19 of the analytes (**Figure 4**) appeared to be differentially expressed by B6 vs. D2 mice (M-CSF, IL-1beta, IL-2, IL-5, IL-6, IL-10, IL-12p70, IL-13, RANTES, KC, MIP-2, MCP-1, MIG, Eotaxin, MIP-1alpha, MIP-1beta, TNF-alpha, IP-10, and IFN-gamma). On day 5, only IL-12p40 appeared to be differentially expressed by B6 vs. D2 mice.

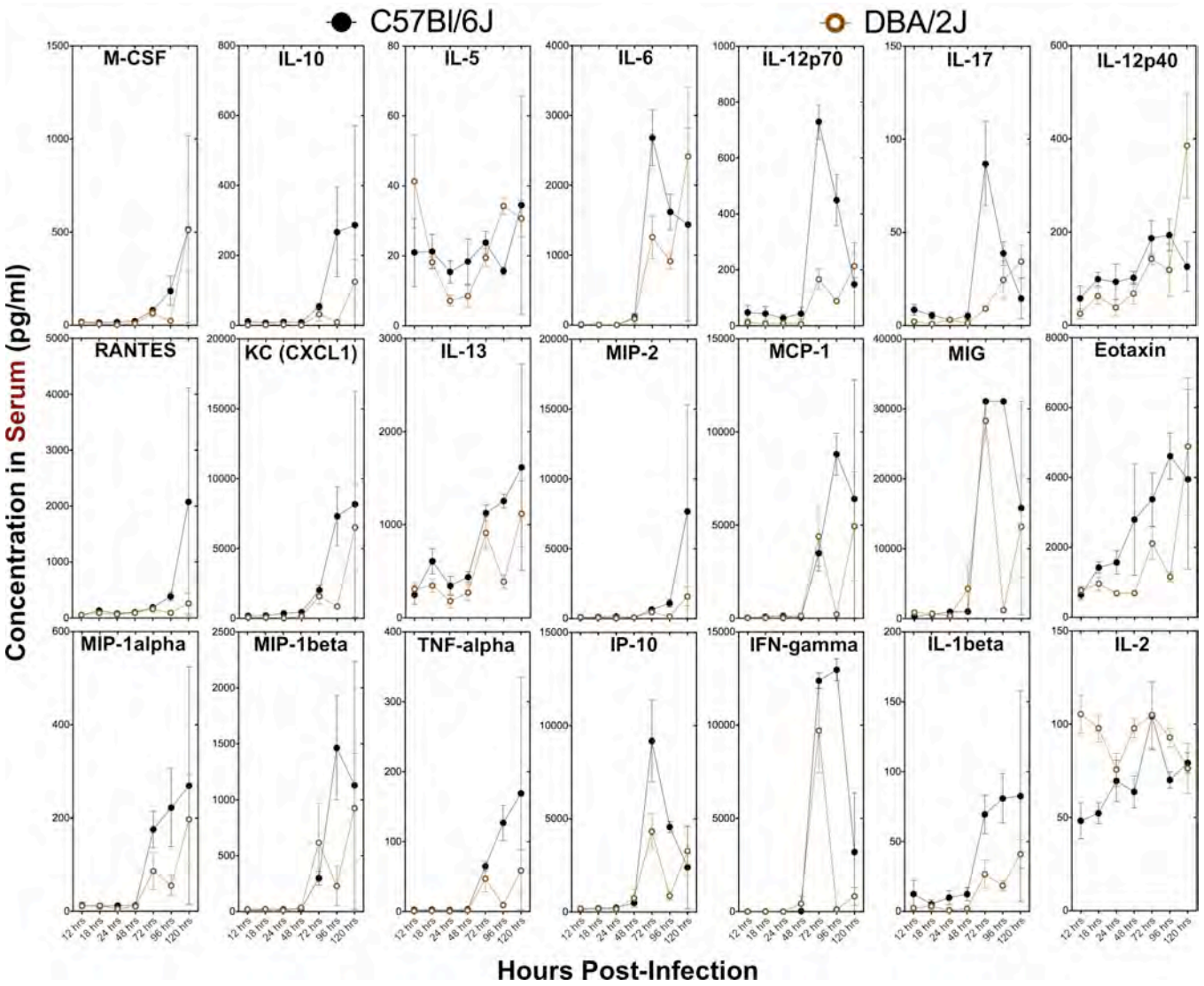

Figure 4. Kinetic monitoring of cytokine/chemokine levels in the peripheral circulation of B6 and D2 mice following pneumonic challenge with *Francisella tularensis* Schu S4. B6 and D2 mice (35/group) were challenged via intranasal instillation with 250 CFU FT Schu S4. At the indicated time points (12, 18, 24, 48, 72, 96, and 120 hrs post-infection), blood samples were collected via submandibular puncture. Quantitation of cytokine/chemokine levels in the serum samples was performed via Luminex-based multiplex analysis (32-plex Millipore kit).

These studies have identified a large number of potential disease-state phenotypes that could be useful for QTL analysis and gene network modeling studies. Choosing the most appropriate timepoint for collecting the data will be a critical decision. Clearly, days 3 and 4 post-infection offer the most distinct phenotypes for QTL analysis, and the day 4 timepoint offers the largest number of phenotypes. However, day 3 post-infection may be the more relevant timepoint for evaluating the effect of disease-state cytokine/chemokine expression on the developing innate immune response to FT.

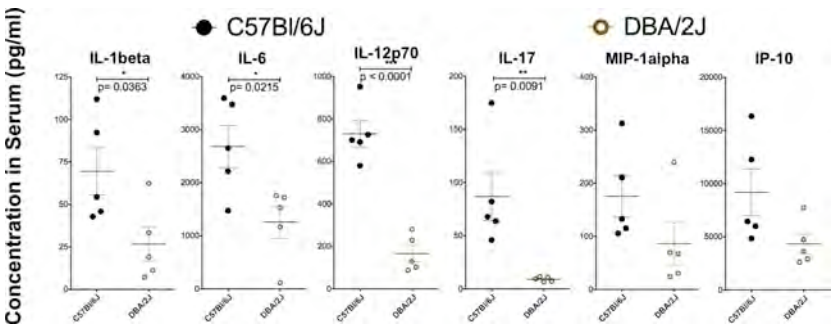

Figure 5. Differential expression of cytokines/chemokines by B6 vs. D2 mice 72-hours post-infection with *Francisella tularensis* Schu S4. B6 and D2 mice (5/group were challenged with 250 CFU FT Schu S4. Blood serum was collected via submandibular puncture 72-hours later. Cytokine/chemokine quantitations were performed via Luminex-based multiplex analysis (32-plex Millipore kit). Statistical analyses were performed using a student-t test and p values are indicated.

B. Key Research Accomplishments

- We have identified 16 distinct phenotypes of differential responsiveness of B6 vs. D2 mice to pneumonic FT infection (BAL cell numbers, 9 analytes in BALF, and 6 analytes in serum) on day 3 post-infection.
- We have identified 25 distinct phenotypes of differential responsiveness of B6 vs. D2 mice to pneumonic FT infection (6 analytes in BALF, and 19 analytes in serum) on day 4 post-infection.
- We have identified 11 distinct phenotypes of differential responsiveness of B6 vs. D2 mice to pneumonic FT infection (10 analytes in BALF, and 1 analytes in serum) on day 5 post-infection.

C. Reportable Outcomes

Publications:
Napier, Brooke A., **Miller, Mark A., Bina, James E**., and Weiss, David S. 2012. A link between intraphagosomal metabolic requirements and virulence in Francisella. PNAS (submitted, under revision).

Llewellyn, A.C., Zhao, J., Song, F., Parvathareddy, Jyothi, Xu, Q., Napier, B.A., Laroui, H., Gallo, R., **Bina, James E**., Cotter, P.A., Miller, **Mark A**., Raetz, Christian R., David S. Weiss. 2012. RtzC is a novel deacetylase involved in lipid A modification and innate immune evasion. Mol. Micro. (manuscript submitted).

D. Conclusions

We have laid the groundwork for QTL analyses that could identify host genetic loci that correlate with differential innate immune responses to pneumonic FT infection. These differences in innate immunity result (at least in part) in a 5-10 fold difference in bacterial burdens between B6 and D2 mice. Our results have also shown quite nicely that the innate response to FT challenge is significantly delayed compared to most infection models. Most of the cytokine levels in both B6 and D2 mice remained relatively flat until day three post-infection. This is unusual and in stark contract to the other 2 pathogens we have discussed in this progress report (*Acinetobacter baumannii* and *Burkholderia pseudomallei*).

2. Studies with *SARS-CoV*.

2.1 Overview

To determine if there is a difference in susceptibility to SARS-CoV infection between the parental strains (C57BL/6J and DBA/2J), we challenged 10-week old, female mice of both strains via intranasal route with $1X10^5$ $TCID_{50}$ of the mouse adapted SARS-CoV strain (diluted in PBS), i.e., MA15 virus, and monitored the mice for weight change and viral replication in the lung tissues for 9 days. As controls, we also inoculated 4 mice from each strain with culture supernatants of Vero-E6 cells (the cell host for propagating the MA15 virus inocula) diluted in PBS. As shown in **Fig. 1**, neither C57BL/6J nor DBA/2J mice receiving control inocula (mock infection) lost weight during the 9-day observation period, indicating that the light anesthesia and intranasal challenge procedures do not produce appreciable adverse effects to these mice, nor do the constituents in culture medium of Vero-E6 cells.

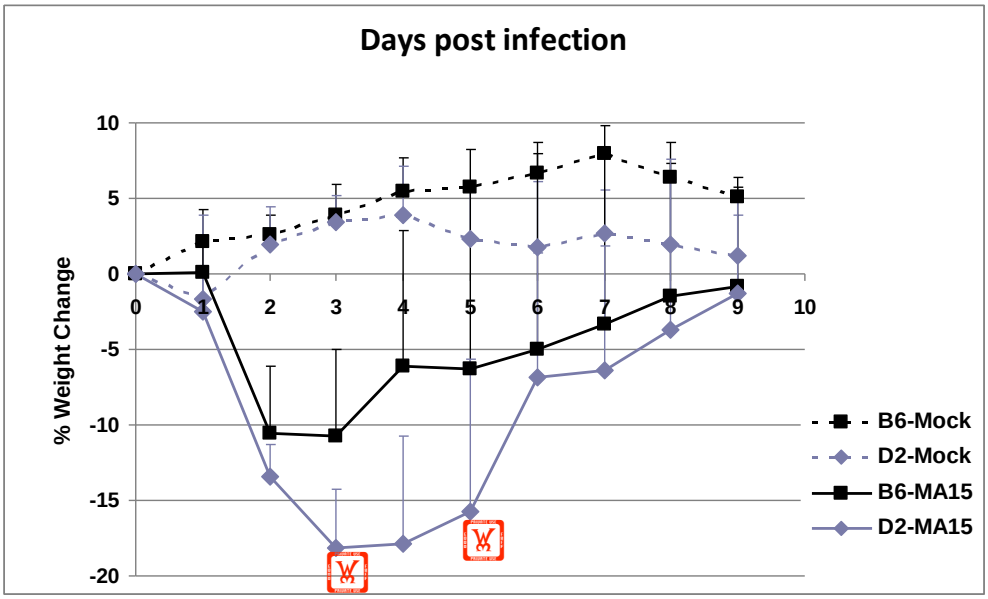

Fig. 1. Weight change of C57BL/6J and DBA/2J mice following challenge with mouse-adapted SARS-CoV, MA15. C57BL/6J (n=26) and DBA/2J (n=28) mice were inoculated with 10^5 $TCID_{50}$ of MA15 virus in PBS via the intranasal route. Control mice (4/group) received Vero-E6 culture supernatant diluted in PBS. Mice were monitored daily for weight change and a subset of infected mice (3-5/group) were sacrificed on 1, 2, 3, 4, 5, and 9 days post infection for evaluation of viral replication in the lungs (see Fig. 2). Asterisk denotes 1 mouse (DBA/2J) death observed on 3 and 5 days post infection, respectively.

In contrast, there was significant weight loss in both strains of mice infected with the MA15 virus. C57BL/6J mice lost a little over 10% of their starting weight at 2-3 days post infection (dpi), followed by a relatively fast recovery. On 8-9 dpi, C57BL/6J mice have regained weight to nearly pre-infection levels. However, DBA/2J mice had substantially more weight loss at 3-5 dpi than C57BL/6J mice, and these mice did not start to recover until after 6 dpi. In addition, a total of two DBA/2J mice died on 3 and 5 dpi, after losing 18% and 25% weight, respectively.

Analyses of infectious viral titers in lungs from a subset of infected mice revealed that high levels of pulmonary viral replication in both strains of mice for the first 4 dpi (**Fig. 2**), with DBA/2J mice harboring consistently 2-3 fold higher levels of viral replication. Strikingly, while viral titers have dropped to the 10^3 $TCID_{50}$/g tissue range in C57BL/6J mice at 5 dpi, viral replication remained high at >10^5 $TCID_{50}$/g tissue levels in DBA/2J mice. The 65-fold higher level of viral replication in DBA/2J mice than in C57BL/6J mice at this time point was consistent with the sustained weight loss seen in DBA/2J mice at 5 dpi. Collectively, these data demonstrate that DBA/2J mice are more susceptible to MA15 virus infection than C57BL/6J mice, in particular, in disease development and in supporting sustained pulmonary viral replication.

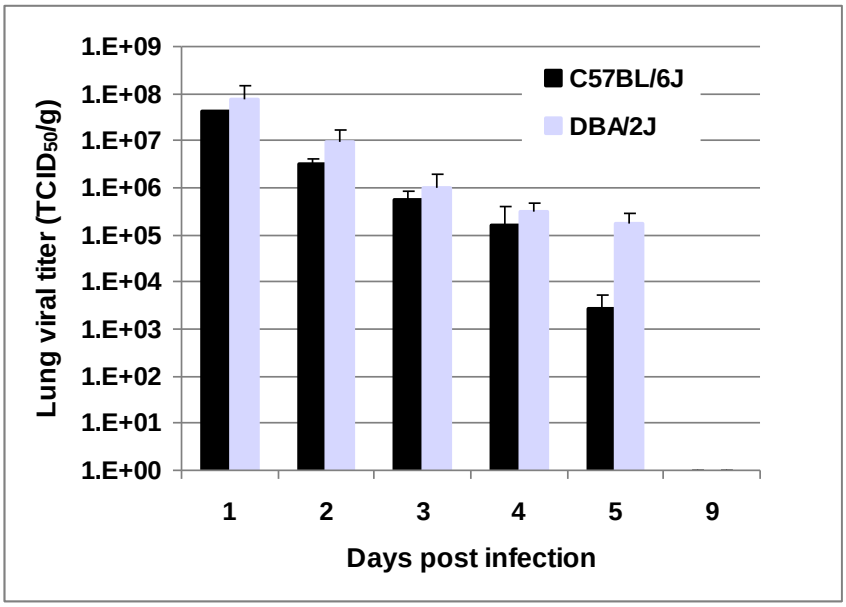

Fig. 2. Viral replication in the lungs of C57BL/6J and DBA/2J mice intranasally challenged with 10^5 $TCID_{50}$ of MA15 virus. Data shown are infectious viral titers in lung tissues from 3-5 mice/strain at each time point.

2.2 Reportable Outcomes

Publication:

Sun L, Xing Y, Chen X, Zheng Y, Yang Y, Nichols DB, Clementz MA, Banach BS, **Li K**, Baker SC, and Chen Z. Coronavirus papain-like proteases negatively regulate antiviral innate immune response through disruption of STING-mediated signaling. PLoS ONE 2012; 7: e30802.

2.3 Conclusions

We have shown that DBA/2J mice are more susceptible to MA15 virus infection than C57BL/6J mice. Compared with C57BL/6J mice, DBA/2J mice develop a more severe disease (as evidenced by more substantial weight loss at 3-5 dpi) and support higher viral replication in the lung, especially at 5 dpi. These findings provide the basis and reveal clear phenotypes for conducting BXD mice studies to identify host genes/pathways that are involved in the differential responses of the parental strains to MA15 virus infection.

3. Mouse Genomics Core

3.1 Transcriptome-mapping results using spleen gene expression data from BXD RI strains

This research program relies on massive gene expression data for the spleen from the BXD strains. These data are of tremendous use for cloning candidate genes and defining gene networks that modulate host-pathogen interactions and the lethality of select agents. During this past period, we performed linkage analysis of whole genome on the transcript level using the BXD spleen gene expression data that were created through Affymetrix GeneChip Mouse Gene 1.0 ST array. There are approximately 35,556 probe sets in this array. About 67% of probe sets (23,745) shows presence in BXD mouse spleen with mean expression values above 7. About 33% of probe sets (11,811) don't express in BXD mouse spleen, and was removed for this analysis. Using our QTLReaper (www.genenetwork.org/qtlreaper.html), a total of 16968 eQTLs have been identified with LRS =>10 (roughly at suggestive level), 3016 eQTLs have been identified with LRS =>17 (roughly at significant level), 581 eQTLs have been identified with LRS =>50 (at very significant level and its expression phenotype looks like a Mendelian trait) (**Table 1**). We categorized these eQTLs into two groups: *cis*-eQTLs, in which the gene and associated marker were within 5 Mb, and *trans*-eQTLs, in which the gene and associated marker were separated by more than 5 Mb. We identified 1565 *cis*-eQTLs and 1451 *trans*-eQTLs at genome-wide significant level (LRS=>17). By increasing the LRS value, the ratio of cis-eQTL to trans-eQTL increases dramatically, but the percentage of cis- and trans-eQTL is similar at significant level (**Table 1**). These gene expression and eQTL data will be used for candidate gene analysis not only by our own group (see example below), but also by the entire research community.

Table 1.Transcriptome QTL mapping of BXD spleen

LRS	Total number	% of probesets	Cis	Trans	% of Cis	% of Trans
>=10	16968	71.46	2020	14948	11.90	88.10
>=17	3016	12.70	1565	1451	51.89	48.11
>=50	581	2.45	497	84	85.54	14.46

3.2 Candidate gene analysis for QTL that control oviduct infection phenotype

One example of candidate gene selection using system genetic strategy and spleen transcriptome-mapping data above is to narrow down the causal gene of QTL that is related to the genetic variance of oviduct infection (OI). This QTL has been mapped to distal chromosome 3 (**Figure 1**). There are more than 100 genes in the QTL region.

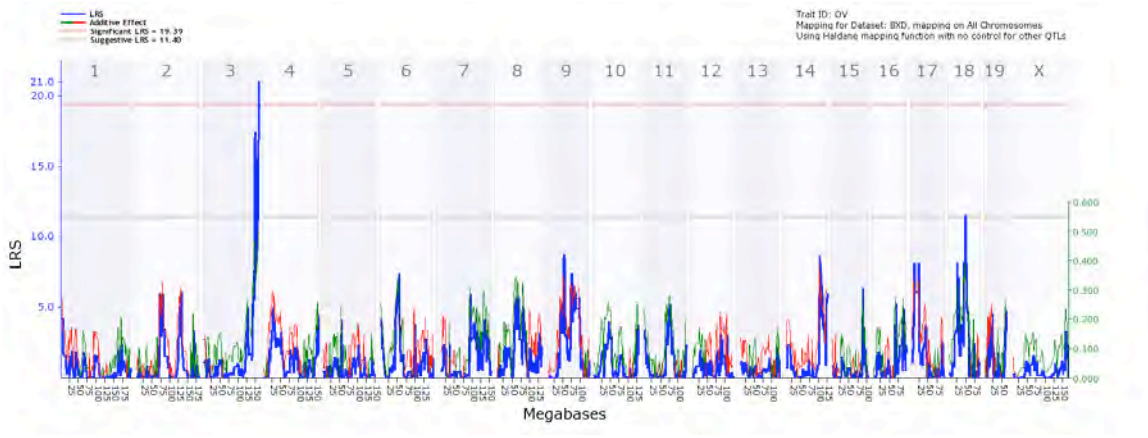

Figure 1. Interval mapping of oviduct gross pathology across the BXD strains reveals a QTL on distal Chr 3

We performed correlation analysis, eQTL analysis, and co-localization analysis using spleen gene expression data above, and finally narrowed down candidate genes from 126 to 5. The expression of those 5 genes is significantly correlated with OI phenotype (P< 0.05), and is cis-regulated with LRS 17 and above (P< 0.05)(**Table 2**).

Table 2. Candidate genes for a QTL of oviduct infection

Symbol	Gene (Chr: Mb)	Expression	Max LRS	eQTL (Chr: Mb)	r	p value (r)
Lphn2	Chr3: 148.478819	8.55	55.4	Chr3: 148.269914	-0.50	0.002
Syde2	Chr3: 145.651617	7.58	26.4	Chr3: 145.095423	-0.59	0.000
Mcoln2	Chr3: 145.812797	9.78	25.6	Chr3: 144.425237	0.35	0.037
Ttll7	Chr3: 146.606970	7.80	25.3	Chr3: 148.269914	-0.43	0.008
Ankrd13c	Chr3: 157.610215	10.36	17.4	Chr3: 157.878563	0.35	0.041

Further analysis of gene function and gene network suggest that Syde2 is the strongest candidate gene. It may work with several other genes together to affect severity of oviduct infection (**Figure 2**).

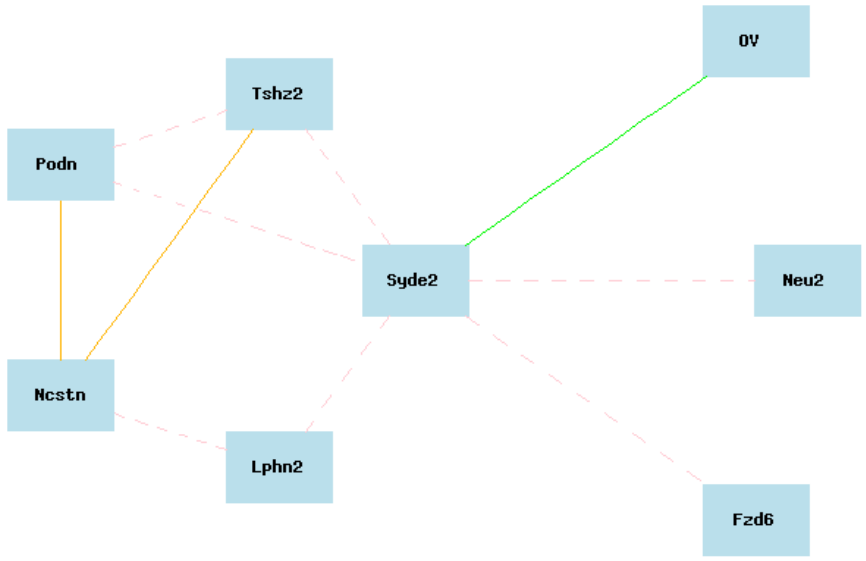

Figure 2. There is a strong network linking *Syde2* with oviduct infection phenotype and other genes

3.3 BXD strains colony for DoD select agents

We maintained more than 400 cages for DoD including most of JAX BXD strains and all of the UTHSC strains. During 2011–2012, we continue to provide BXD mice to the research program and added more new strains into the RBL area for multiple DoD projects. We are developing another 80 new BXD strains continuously, which will be used for result validation as the second cohort. Of these new strains, ~36 new strains have passed the 10th generation of inbreeding, and ~59 strains have passed the 8th generation. In the past year, we genotyped all of these 80 new BXD strains with 50 UTHSC BXD strains together using GeneSeek SNP array at about 8000 SNPs density. Many alleles have already

showed homozygosis for most of strains that can be used to validate genetic modulators for some selected phenotype or gene expression.

3.4 Develop and test the method of reverse complex trait analysis (RCTA)

QTL mapping usually proceeds through a forward genetics approach, starting with a complex phenotype that varies across a population and attempting to identify the genes and, potentially, genetic variations that cause this variation. RCTA is a novel reverse genetics method, and often starts with natural sequence variants rather than with engineered alleles or mutagenized stock. After we generated ~100X whole-genome shotgun coverage of DBA/2J (D2) combining with public available sequence of C57BL/6J (B6), we were able to generate a nearly comprehensive list of sequence variants, and identify the downstream effects of those sequence variants using BXD RI strains. In the past few years, we have identified 4.8 M SNPs, 680K insertions and deletions (InDels), and thousands of inversions and copy number variants (CNVs) segregating among the 80 BXD strains. In this past year, we explored possible functional consequences of sequence and structural variants using a large data set of expression profiles from the BXD family, and developed and tested the method of reverse complex trait analysis (RCTA). Here is one example that is related to immune system.

There is a single nonsynonymous SNP in *Wdr26*, which is a gene with an important role in innate immune response through suppression of the MAPK signaling pathway. Expression mapping showed that *Wdr26* is associated with a strong *cis* eQTL with an LRS 40 in lung (**Figure 3**).

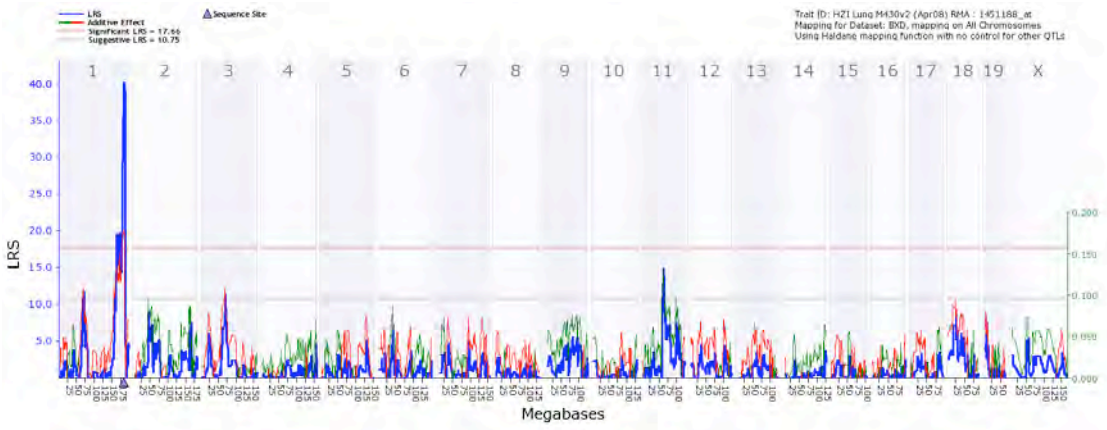

Figure 3. Interval mapping of *Wdr26* expression showed it is cis-regulated.

Expression levels of *Wdr26* covary well (r = –0.7167, p = 0.0012) with T cell proliferation in the immune system (GN Trait ID 10237, **Figure 4**), a trait that maps very closely to *Wdr26* with an LRS > 49. The human ortholog, *WDR26*, directly binds free Gβγ and forms a complex with endogenous Gβγ in T cells, attenuating chemotaxis in the T cells, which corroborates the function of *Wdr26* in mouse. This example illustrated that the functional consequence of the single nonsynonymous SNP in *Wdr26* can be readily determined by the reverse complex trait analysis.

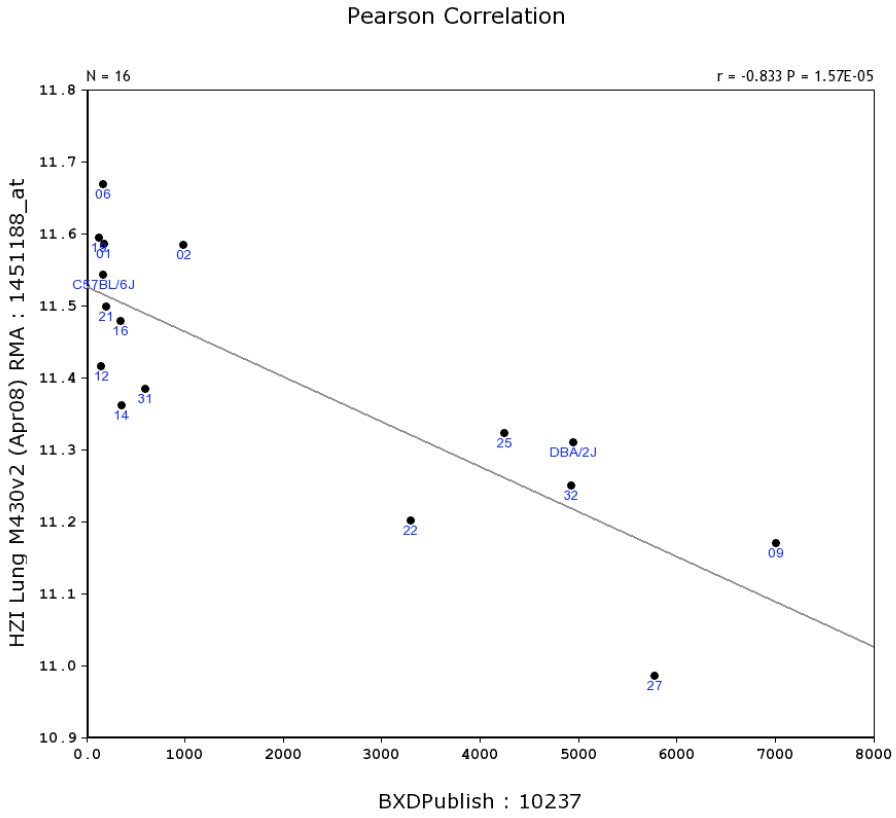

Figure 4.The expression of *Wdr26* correlated with T cell proliferation very well (r = -8.33, p < 0.0001).

The identification of sequence variants that modulate phenotypes is fundamental to understanding the genetic basis of both qualitative Mendelian traits and quantitative complex traits. The reverse complex trait analysis could efficiently link sequence variants to novel phenotypes. The tools and resources for RCTA analysis are publically available at GeneNetwork (GN) for DoD group and others in the research community.

3.5 New infectious or immune related data entered into GeneNetwork

We have generated and distributed a large number of important resources that are now used by DoD investigators to address central questions on the genetics of infection response. These data sets include spleens (109 strains), lung (57 strains), T cell (33 strains), etc.

3.6 Reportable outcomes

Publication:

Wang X, Mulligan MK, Pandey A, **Lu L**, Ciobanu DC, Nelson SF, Pollard KS, Taylor WL, Thomason DB, **Williams RW**: Sequencing the DBA/2J Mouse Genome: Reverse Genetics Using Test Cross Progeny. **PlosBiology** 2012, Manuscript in preparation.

4. Construction of gene network models

4.1 Introduction

Bayesian networks are graphical models that represent the dependence structure among multiple interacting variables. They consist of variables (nodes) that are connected by directed edges representing causal relationships between the nodes. The graphical representations in Bayesian networks allow for clear visualization and interpretation of the relationships between variables. Additionally, the causal dependencies implied by the networks provide testable hypotheses that can be used to assess the validity of the model or further investigate the relationships in the network. We have developed a workflow for Bayesian modeling of biological networks, such as those that are involved in determining responses to pathogen infection, and apply the model to two datasets using the BXD family of recombinant inbred mice. First, we provide an overview of modeling of the disease status of BXD mice infected with *Chlamydia psittaci*. Next, we apply our Bayesian network modeling method to the expression of immune related genes in the spleens of BXD mice.

4.2 Body

4.2.1 Summary of modeling of *Chlamydia* infection:

In the last year, we completed our investigation of *Chlamydia* infection in BXD mice a prepared a manuscript that has recently been published (2). We provided an extended discussion of these results in last year's annual report and will, therefore, only briefly summarize the creation and validation of the *Chlamydia* infection model.

BXD strains with the D2 genotype at the *Ctrq3* locus are more susceptible to infection with *Chlamydia psittaci* than strains with the B6 genotype; however, the specific molecular mechanism through which the genotype impacts disease status is unknown (1). To elucidate the pathways that connect *Ctrq3* genotype with disease outcome, we created a Bayesian network model from three sets of data: (1) *Ctrq3* genotype, (2) intermediate immune-related phenotypes, including quantitative variables associated with cytokines, macrophages, neutrophils, and pathogen load, and (3) disease status as quantified by the ratio of weight 6 days after infection to weight at the time of infection. Based on an analysis of correlations between variables, we selected 5 variables (genotype at *Ctrq3*, neutrophil level, pathogen load, MAS, and weight ratio) and created a Bayesian network model based on these variables (**Figure 1**). We performed cross-validation of the model to assess its accuracy and found that all variables in the network were predicted with an accuracy > 80%.

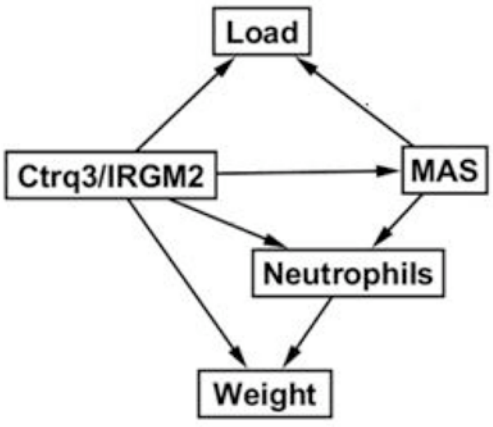

Figure 1. Bayesian network modeling of *C. psittaci* infection

We further investigated two of the relationships implied by the network. First, we used the model to predict the effects of external intervention on macrophages on disease progression and compared the predictions with data obtained from mice in which macrophages were chemically depleted. The effect of macrophage depletion on neutrophil level and weight change predicted by the model matched what was observed experimentally. Second, we found that strains with the susceptible genotype lost weight as a function of pathogen load while strains with the resistant genotype were almost completely unaffected over a wide range of pathogen load and confirmed this result in a larger cohort of BXD mice.

4.2.2 Modeling of immune-related genes in the spleens of BXD mice:

Gene expression in the spleen of young adult mice was profiled using the Affymetrix GeneChip Mouse Gene 1.0 ST array in a total of 108 strains, including 81 BXD strains. The data is freely available in the GeneNetwork website (www.genenetwork.org) and further details of the sample collection and processing are available at genenetwork.org/dbdoc/UTHSC_SPL_RMA_1210.html. To examine the expression of immune related gene in the spleen, we selected all 1249 genes with an "immune system process" Gene Ontology annotation (GO:0002376). We then identified all probesets in the spleen gene expression dataset that target these genes. A total of 1421 probesets target these immune related genes, and this collection of probesets was used in all of the following analysis.

Initial QTL mapping results:

We performed gene expression quantitative trait locus (eQTL) mapping of the immune related genes using QTLReaper (www.genenetwork.org/qtlreaper.html) for the BXD strains. 414 of the probesets were associated with eQTLs with an LRS ≥ 15. We categorized these eQTLs into two groups: *cis*-eQTLs, in which the gene and associated marker were within 5 Mb, and *trans*-eQTLs, in which the gene and associated marker were separated by more than 5 Mb. We identified 140 *cis*-eQTLs and 274 *trans*-eQTLs. In general, the genetic variation that underlies a *cis*-eQTL is believed to be found within the gene itself or to otherwise directly impact the expression of the gene. *Trans*-eQTLs, in contrast, are thought to result from an indirect mechanism. For example, a genetic variant located within the promoter region of gene A (*i.e.* a *cis*-eQTL) may directly impact expression of gene A. If the expression of gene A then affects the expression of genes B and C, the genetic variant would also be in indirect factor (i.e. a *trans*-eQTL) that explains the variation in expression of genes B and C.

As we investigated the eQTL mapping results, we found that *trans*-eQTLs were not evenly distributed across the genome. While the density of *trans*-eQTLs across the majority of the genome was low, there were several loci that contained several *trans*-eQTLs. For example, only 2 genes had a *trans*-eQTL that mapped to Chr 1 from 0-138 Mb, while 9 genes had a *trans*-eQTL that mapped to Chr 1 from 138-161 Mb. We identified a total of 9 genomic locations containing at least one *cis*-eQTL and at least three *trans*-eQTLs for the selected immune related genes. These 9 locations are promising starting points for modeling of immune gene networks in the spleen. Here, we will focus our discussion on creating models for two locations: Chr 2 near 65 Mb and Chr 17 near 35 Mb.

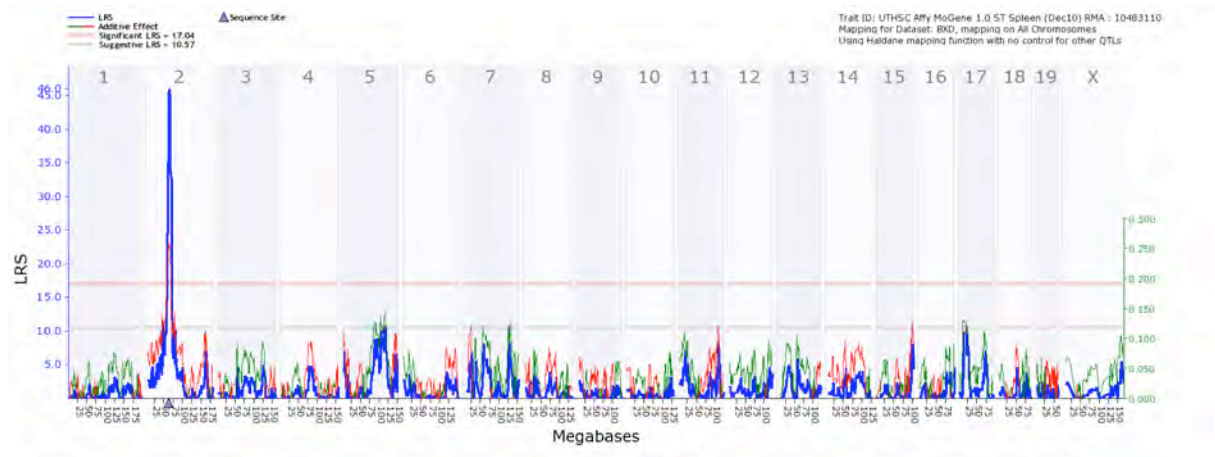

Figure 2. QTL mapping results for *Ifih1*. Significant QTLs ($p < 0.05$) are indicated by the peak solid red line, while suggestive QTLs ($p < 0.63$) are indicated with the solid grey line. The location of the gene is indicated by the purple triangle.

Modeling of impact of genetic variation on Chr 2 near 65 Mb:
Our first gene network model will investigate the impact of genetic variations at Chr 2 near 65 Mb on gene expression of immune related genes. One gene, *Ifih1*, located at 62.4 Mb on Chr 2 was regulated by a *cis*-eQTL at this location (**Figure 2**), and 12 genes had a *trans*-eQTL with LRS >= 15 at Chr 2 between 62 and 68 Mb. The genes with *trans*-eQTLs were highly correlated with one another and with *Ifih1* (**Figure 3**). The first step in creating a Bayesian network model is selecting the variables to include in the model. We selected the BXD genotype at rs3664317 (63.9 Mb on Chr 2) and *Ifih1* expression as two variables to include in the network. We removed genes that had low LRS values, low expression, low variance across strains, or a small difference in expression between the parental strains of the BXD mice. Of the genes with *trans*-eQTLs, we selected *Ifit1*, *Oas1a*, and *Oas1g*.

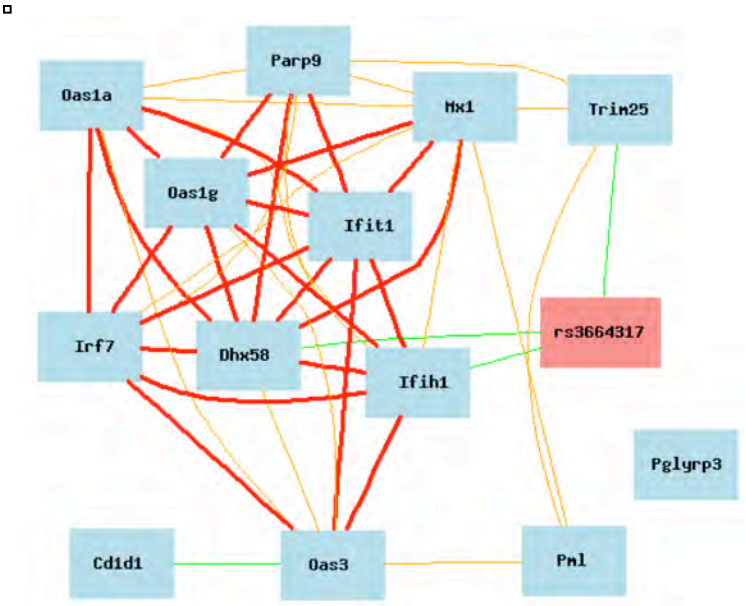

Figure 3. Correlation network of associations between a BXD genotype at 63.9 Mb on Chr 2 (rs3664317) and genes with eQTLs mapping near this locus. Correlations with Pearson's correlation > 0.7 (red), > 0.5 (orange), and < -0.5 (green) are shown.

We then used our Bayesian network modeling pipeline to learn the structure of the gene network model. We have described our structure learning method previously (2). Our structure learning procedure allows for prior knowledge to be included in the network by requiring that specific features are either included or excluded from the network structure. For example, if a regulatory relationship among genes is known, only network structures that include this relationship will be included in the network. Here, we prevented *Ifih1*, the *cis*-regulated gene, from being the child of any of the *trans*-regulated genes. **Figure 4** shows the structure of the gene network model of the Chr 2 eQTL. Some interesting relationships can be observed in the structure of the network. First, the genotype at rs3664317 influences the expression of *Ifih1* in all high scoring networks, as expected, but the genotype only influences the expression of the *trans*-regulated genes indirectly (i.e., *Ifih1* masks the influence of the genotype on the *trans*-regulated genes). Additionally, the network shows that there is a strong influence of the expression of *Ifih1* on *Ifit1* and *Oas1g* on *Oas1a*.

We performed parameter learning as described previously and assessed the model with the using leave-one-out cross validation. Specifically, we used the Q^2 parameter to evaluate the quality of the continuous predictions; a random predictor would provide $Q^2 = 0$, while a perfect predictor would provide $Q^2 = 1$. The values of Q^2 for predictions of the expression of *Ifih1*, *Ifit1*, *Oas1g*, and *Oas1a* using leave-one-out cross validation were 0.43, 0.66, 0.70, and 0.76, respectively.

Modeling of impact of genetic variation on Chr 17 near 35 Mb:
In contrast to the Chr 2 locus which contained only a single gene with a strong *cis*-eQTL, a locus on Chr 17 near 35 Mb contained several eQTLs for both *cis*- and *trans*-regulated immune related genes (**Figure 5**). Specifically, 17 and 15 probesets were regulated by *cis*- and *trans*-eQTL, respectively,

located between 33 and 38 Mb on Chr 17 with an LRS > 15. The majority of the *cis*-regulated genes were related to the histocompatibility complex, including, for example, *H2-K1*, *H2-Oa*, and *H2-Q6*. Except for *H2-Ea-ps*, all of the *cis*-regulated genes were highly correlated with each other; *H2-Ea-ps* had higher expression in strains with the D allele at this locus, while the other H2 genes had higher expression in strains with the B allele. To reduce the amount of data needed to examine the *cis*-regulated genes and, potentially, reduce the noise in the data obtained from single probesets, we used principal component analysis tools that are available in the GeneNetwork to select the first principal component (PC1) of the H2 genes with *cis*-eQTLs at this locus, excluding *H2-Ea-ps*. PC1 had a highly significant eQTL at Chr 17 near 35 Mb, and we, therefore, used PC1 in our network modeling. While investigating the *trans*-regulated genes to select genes for use in building gene network models, we observed that 3 chemokine receptor genes (*Cxcr3*, *Ccl19*, *Cx3cr1*) had *trans*-eQTLs at Chr 17 near 35 Mb and included these genes in the model. Finally, we included rs13482958, which is located at 34.5 Mb on Chr 17, as the genotype node in the network. We used no restrictions when performing network structure learning.

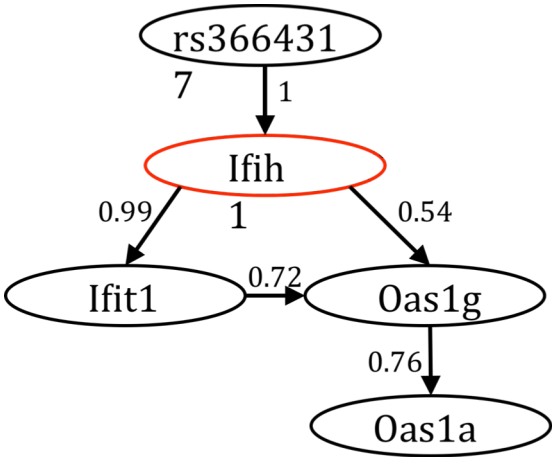

Figure 4. Structure of the Bayesian network model of influence of genetic variation at Chr 2 near 65 Mb on the expression of immune related genes. The number next to each directed edge of the BN indicates the confidence in the edge after model averaging as described in the text. *Cis*-regulated genes are shown in red.

Figure 4 shows the structure of the gene network model for genes regulated by the Chr 17 locus. In contrast to the behavior found for the for the Chr 2 locus (**Figure 3**), the effect of the genotype at the locus on all of the *trans*-regulated genes is not masked by the expression of the *cis*-regulated genes, as *Ccl19* is the direct child of the genotype node. This result may be due to *Ccl19* being influenced by a specific *cis*-regulated gene whose expression was not sufficiently captured by PC1. We performed leave-one-out cross validation to evaluate the network. The values of Q^2 for predictions of PC1, *Ccl19*, *Cxcr1*, and *Cxcr3* were 0.69, 0.51, 0.46, and 0.38, respectively.

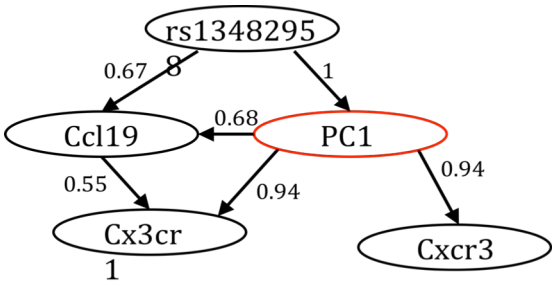

Figure 5. Structure of the Bayesian network model of influence of genetic variation at Chr 17 near 35 Mb on the expression of immune related genes. The number next to each directed edge of the BN indicates the confidence in the edge after model averaging as described in the text. PC1 is the first principal component of a cluster of histocompatibility complex genes that are located near rs13482958 and regulated by a *cis*-eQTL.

Key Research Accomplishments

- Completed and published Bayesian network modeling of *Chlamydia* infection in BXD mice
- Improved our integrated method for Bayesian network structure learning, parameter learning, cross-validation, and the prediction of the effects of external interventions, making it more automated and allowing for quicker model building for future data sets
- Analyzed gene expression of immune-related genes in the spleens of BXD mice and identified loci that impact the expression of several immune-related genes in *trans*
- Created two Bayesian network models for gene expression in the spleen

Reportable Outcomes

Publication:

Miyairi I, Ziebarth J, Laxton JD, Wang X, van Rooijen N, **Williams RW**, **Lu L, Byrne GI**, and **Cui Y**. 2012. Host genetics and Chlamydia disease: prediction and validation of disease severity mechanisms. PLoS One 7:e33781.

Conclusion

We have implemented a method for performing Bayesian network analysis of biological data, such as responses to pathogen infection. We first completed analysis of a model explaining the development of *Chlamydia psittaci* in BXD mice. Then, we applied our method to explore networks linking genotype and the expression of immune-related genes in the spleens of BXD mice. This work is significant not only because it improves understanding of the model systems examined here, but also because it shows that our Bayesian network workflow can be adapted for application to modeling responses to infectious diseases and other biological processes.

References

1. Miyairi, I., V. R. Tatireddigari, O. S. Mahdi, L. A. Rose, R. J. Belland, L. Lu, R. W. Williams, and G. I. Byrne. 2007. The p47 GTPases Iigp2 and Irgb10 regulate innate immunity and inflammation to murine *Chlamydia psittaci* infection. J Immunol 179:1814-24.

2. Miyairi, I., J. Ziebarth, J. D. Laxton, X. Wang, N. van Rooijen, R. W. Williams, L. Lu, G. I. Byrne, and Y. Cui. 2012. Host genetics and Chlamydia disease: prediction and validation of disease severity mechanisms. PLoS One 7:e33781.

OPEN ACCESS Freely available online

PLoS PATHOGENS

Inflammasome-dependent Pyroptosis and IL-18 Protect against *Burkholderia pseudomallei* Lung Infection while IL-1β Is Deleterious

Ivonne Ceballos-Olvera, Manoranjan Sahoo, Mark A. Miller, Laura del Barrio, Fabio Re[¤]*

Department of Microbiology, Immunology, and Biochemistry, University of Tennessee Health Science Center, Memphis, Tennessee, United States of America

Abstract

Burkholderia pseudomallei is a Gram-negative bacterium that infects macrophages and other cell types and causes melioidosis. The interaction of *B. pseudomallei* with the inflammasome and the role of pyroptosis, IL-1β, and IL-18 during melioidosis have not been investigated in detail. Here we show that the Nod-like receptors (NLR) NLRP3 and NLRC4 differentially regulate pyroptosis and production of IL-1β and IL-18 and are critical for inflammasome-mediated resistance to melioidosis. *In vitro* production of IL-1β by macrophages or dendritic cells infected with *B. pseudomallei* was dependent on NLRC4 and NLRP3 while pyroptosis required only NLRC4. Mice deficient in the inflammasome components ASC, caspase-1, NLRC4, and NLRP3, were dramatically more susceptible to lung infection with *B. pseudomallei* than WT mice. The heightened susceptibility of *Nlrp3*$^{-/-}$ mice was due to decreased production of IL-18 and IL-1β. In contrast, *Nlrc4*$^{-/-}$ mice produced IL-1β and IL-18 in higher amount than WT mice and their high susceptibility was due to decreased pyroptosis and consequently higher bacterial burdens. Analyses of IL-18-deficient mice revealed that IL-18 is essential for survival primarily because of its ability to induce IFNγ production. In contrast, studies using IL-1RI-deficient mice or WT mice treated with either IL-1β or IL-1 receptor agonist revealed that IL-1β has deleterious effects during melioidosis. The detrimental role of IL-1β appeared to be due, in part, to excessive recruitment of neutrophils to the lung. Because neutrophils do not express NLRC4 and therefore fail to undergo pyroptosis, they may be permissive to *B. pseudomallei* intracellular growth. Administration of neutrophil-recruitment inhibitors IL-1ra or the CXCR2 neutrophil chemokine receptor antagonist antileukinate protected *Nlrc4*$^{-/-}$ mice from lethal doses of *B. pseudomallei* and decreased systemic dissemination of bacteria. Thus, the NLRP3 and NLRC4 inflammasomes have non-redundant protective roles in melioidosis: NLRC4 regulates pyroptosis while NLRP3 regulates production of protective IL-18 and deleterious IL-1β.

Citation: Ceballos-Olvera I, Sahoo M, Miller MA, del Barrio L, Re F (2011) Inflammasome-dependent Pyroptosis and IL-18 Protect against *Burkholderia pseudomallei* Lung Infection while IL-1β Is Deleterious. PLoS Pathog 7(12): e1002452. doi:10.1371/journal.ppat.1002452

Editor: Dana J. Philpott, University of Toronto, Canada

Received June 30, 2011; **Accepted** November 7, 2011; **Published** December 29, 2011

Copyright: © 2011 Ceballos-Olvera et al. This is an open-access article distributed under the terms of the Creative Commons Attribution License, which permits unrestricted use, distribution, and reproduction in any medium, provided the original author and source are credited.

Funding: This work was supported by National Institutes of Health grants AI076835, AI081861 (F.R.) and Department of Defense Army grant W81XHW-05-1-0227. The funders had no role in study design, data collection and analysis, decision to publish, or preparation of the manuscript.

Competing Interests: The authors have declared that no competing interests exist.

* E-mail: fre@uthsc.edu; fabio.re@rosalindfranklin.edu

¤ Current address: Department of Microbiology and Immunology, Chicago Medical School, Rosalind Franklin University of Medicine and Science, North Chicago, Illinois, United States of America

Introduction

The ability to detect infection by pathogenic microbes and to restrict their growth are fundamental for the wellbeing of multicellular organisms. Pattern recognition receptors, including the Toll-like receptor (TLR) and the NLR, recognize microbial products and "danger signals" released by stressed cells and, in turn, activate signaling pathways that initiate the inflammatory response and regulate development of adaptive immunity. TLR are expressed on the cell surface or in endosomal compartments and their stimulation results in activation of the NF-κB, MAPK, and IRF signaling pathways culminating in transcriptional induction of a large number of genes. NLR, in contrast, are located in the cytoplasm, which they survey for evidence of danger or infection (reviewed in ref. [1]). Some NLR control activation of the inflammasome, a multiprotein complex that contains, in addition to a NLR, the adaptor molecule ASC and the protease caspase-1. Activation of caspase-1 in the context of the inflammasome is responsible for the proteolytic processing of the immature forms of IL-1β and IL-18, a modification required for the secretion and bio-activity of these proinflammatory cytokines. Activation of caspase-1 also triggers a form of cell death, known as pyroptosis, that effectively restricts intracellular bacterial growth [2,3]. Production of IL-1β and IL-18 and induction of pyroptosis have been shown to be protective effector mechanisms against many infectious agents. NLRP3 and NLRC4 are the best characterized NLR molecules. NLRP3 controls caspase-1 activation in response to "danger signals", several particles and crystals, and various bacteria, virus, and fungi. Although the logic that oversees the activation of the NLRP3 inflammasome is still elusive, it appears that disruption of cell membrane integrity may be a common event triggered by the NLRP3 activators. The NLRC4 inflammasome is responsive to a narrower spectrum of activators including cytoplasmically delivered bacterial flagellin and the basal rod constituent of various bacterial Type III secretion systems (T3SS). The T3SS apparatus is used by several bacteria, including *Salmonella*, *Yersinia*, *Pseudomonas*, *Shigella*, *Legionella*, *and Burkholderia* to inject virulence factors into the cytoplasm of target cells. Recent

Author Summary

The disease melioidosis is caused by the intracellular bacterium *Burkholderia pseudomallei*, a potential bioterrorism agent. Here we examined the interaction of *B. pseudomallei* with the inflammasome, an important innate immune pathway that regulates at least two host responses protective against infections: 1) secretion of the proinflammatory cytokines IL-1β and IL-18 and 2) induction of pyroptosis, a form of cell death that restricts intracellular bacteria growth. Using a mouse model of melioidosis we show that two distinct inflammasomes are activated by *B. pseudomallei* infection. One, containing the Nod-like receptor (NLR) NLRP3, mediates IL-1β and IL-18 induction. The other contains a different NLR called NLRC4 and mediates pyroptosis. Pyroptosis and IL-18 production were equally important for resistance to *B. pseudomallei*. Surprisingly, IL-1β was found to be deleterious in melioidosis. The detrimental role of IL-1β during melioidosis was due, in part, to excessive recruitment of neutrophils to the lung. We show that neutrophils do not express NLRC4, fail to undergo pyroptosis, and, therefore, may be permissive to *B. pseudomallei* intracellular replication leading to increased bacterial burden and morbidity/mortality. Thus, the NLRP3 and NLRC4 inflammasomes have non-redundant protective roles in melioidosis: NLRC4 regulates pyroptosis while NLRP3 regulates production of protective IL-18 and deleterious IL-1β.

works demonstrated that the specificity of the mouse NLRC4 for flagellin or rod proteins is determined by its interaction with the NLR molecules NAIP5 or NAIP2, respectively [4,5].

Burkholderia pseudomallei is a Gram-negative flagellate bacterium that causes melioidosis, a disease endemic to South-East Asia and other tropical regions [6,7] and the most common cause of pneumonia-derived sepsis in Thailand. Because melioidosis carries a high fatality rate, *B. pseudomallei* is classified as category B potential bioterrorism agent by the Center for Disease Control and NIAID. *B. pseudomallei* infection can be contracted through ingestion, inhalation, or subcutaneous inoculation and leads to broad-spectrum disease forms including pneumonia, septicemia, and organ abscesses. Following infection of macrophages and other non-phagocytic cell types, *B. pseudomallei* is able to escape the phagosome and invade and replicate in the host cell cytoplasm, directly spreading from cell to cell using actin-tail propulsion. Macrophages and IFNγ have been shown to play a critical role in protection from melioidosis [8–10] and several *B. pseudomallei* virulence factors have been identified including the bacterial capsule [11], the lipopolysaccharide [12], and one of the three T3SS possessed by *B. pseudomallei* [13]. Analysis of mouse strains with different susceptibility to *B. pseudomallei* infection indicates that the early phases of the infection are crucial for survival [14,15], emphasizing the necessity for better understanding of innate immune responses during melioidosis. With this goal in mind, using a murine model of melioidosis we have performed a detailed analysis of the role of the inflammasome components NLRP3, NLRC4, ASC, and caspase-1 and the effector mechanisms IL-1β, IL-18, and pyroptosis.

Results

NLRP3 and NLRC4 differentially regulate production of IL-1β and pyroptosis

To identify the pathway responsible for IL-1β and IL-18 secretion in response to infection with *B. pseudomallei*, bone marrow-derived macrophages (BMDM) or dendritic cells (BMDC) derived from WT mice or mice deficient in the inflammasome components ASC, NLRP3, NLRC4, or caspase-1 were infected *in vitro* with *B. pseudomallei* and secretion of IL-1β in culture supernatants was measured. As shown in figure 1A, secretion of IL-1β by *Asc*$^{-/-}$, *Nlrp3*$^{-/-}$, and *Casp1*$^{-/-}$ BMDM was markedly reduced compared to WT BMDM. Production of IL-1β during the first hours of the infection was also significantly reduced in *Nlrc4*$^{-/-}$ cells. However, later in the infection process (8 hours) *Nlrc4*$^{-/-}$ cells secreted IL-1β at levels considerably higher than WT cells. Secretion of IL-18 followed a similar pattern (data not shown). Immunoblotting of the supernatants confirmed processing of IL-1β and of caspase-1 to the mature 17 kDa and p20 forms, respectively (figure 1B). Interestingly, although caspase-1 was activated in *Asc*$^{-/-}$ cells, processing and secretion of IL-1β was not observed. NLRC4 possesses an amino-terminal CARD domain that can recruit and activate caspase-1 independently of ASC. It is unclear at present why activation of caspase-1 in *Asc*$^{-/-}$ cells is not sufficient to trigger secretion of mature IL-1β, a phenomenon previously reported by other groups [16]. The differences in IL-1β and IL-18 secretion were observed regardless of the number of bacteria used to infect cells (MOI 10, 50, or 100, data not shown) and were not due to differential induction of pro-IL-1β, which was present at comparable amounts in all the cell lysates. Thus, the NLRC4 and NLRP3 inflammasomes are both mediating release of IL-1β and IL-18 by myeloid cells infected with *B. pseudomallei*.

Inflammasome-mediated induction of pyroptosis has been demonstrated to be a mechanism that restricts growth of certain intracellular bacteria [2,3]. To measure induction of pyroptosis in cells infected with *B. pseudomallei* we used a kanamycin protection assay that allows only replication of intracellular bacteria whereas cells that undergo pyroptosis expose the bacteria to the microbicidal action of the antibiotic present in the medium. Induction of pyroptosis and intracellular bacterial replication were measured in WT or inflammasome-deficient BMDM infected with *B. pseudomallei*. As shown in figure 1C (upper graph), pyroptosis of infected cells (as measured by release of LDH in culture supernatants) was significantly reduced in *Casp1*$^{-/-}$ and *Nlrc4*$^{-/-}$ cells compared to WT and *Nlrp3*$^{-/-}$. Importantly, induction of pyroptosis was not lost in *Asc*$^{-/-}$ cells. NLRC4-mediated pyroptosis induced by other bacteria is also reported to be ASC-independent [16–19]. Consistent with the role of pyroptosis as a mechanism to restrict intracellular bacteria growth, considerably less intracellular bacteria were recovered from WT, *Nlrp3*$^{-/-}$, and *Asc*$^{-/-}$ cells than *Casp1*$^{-/-}$ or *Nlrc4*$^{-/-}$ cells at all time points (figure 1C, lower graph). Similar results regarding IL-1β processing and secretion and induction of pyroptosis were obtained using BMDC derived from the inflammasome–deficient mice (supplementary figure S1).

Taken together these results show that infection of macrophages and dendritic cells with *B. pseudomallei* leads to activation of the NLRC4 and NLRP3 inflammasomes. NLRC4 contributes to IL-1β during the early phase of the infection and induction of pyroptosis that restricts bacterial growth. NLRP3 does not control pyroptosis and primarily controls IL-1β secretion. It should be noted that the defective IL-1β production of *Nlrc4*$^{-/-}$ and *Nlrp3*$^{-/-}$ cells cannot be ascribed to the difference in induction of pyroptosis: thus *Nlrp3*$^{-/-}$ cells produce less cytokine than WT cells despite undergoing pyroptosis to the same extent as WT cells. Conversely, *Nlrc4*$^{-/-}$ cells, which are resistant to pyroptosis, still produce less cytokine than WT cells at the early time point. However, at later time points *Nlrc4*$^{-/-}$ cells produce considerably more IL-1β than WT cells. This is likely due to the fact that WT cells rapidly die after infection while *Nlrc4*$^{-/-}$ cells remain viable and continue to synthesize and secrete IL-1β.

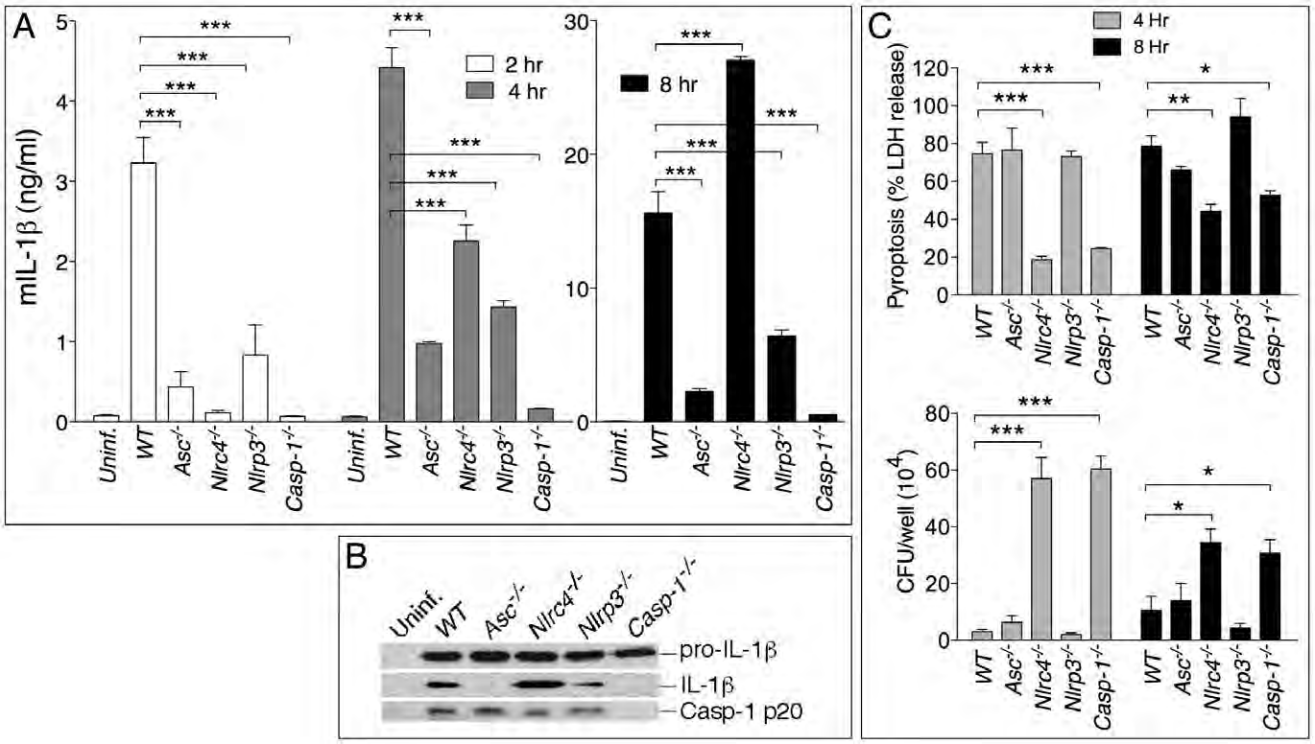

Figure 1. NLRP3 and NLRC4 differentially regulate production of IL-1β and pyroptosis. BMDM were infected with *B. pseudomallei* at MOI of 10. (A) Secretion of mature IL-1β was measured in conditioned supernatants of infected and uninfected cells at the indicated times. (B) Processing of IL-1β and caspase-1 was detected by immunoblot in 8 h conditioned supernatants from A. Pro-IL-1β was detected in cell lysate of the infected cells. (C) Induction of pyroptosis was measured as LDH release in conditioned supernatants of infected BMDM (MOI 10) (upper panel). Infected BMDM were lysed at the indicated time points after infection and intracellular bacteria growth was quantitated (lower panel). One experiment representative of three is shown. $*p<0.05$, $**p<0.01$, $***p<0.001$ (1way ANOVA).
doi:10.1371/journal.ppat.1002452.g001

Role of inflammasomes in murine melioidosis

The role of the inflammasome during *in vivo B. pseudomallei* infection was next analyzed using a mouse model of melioidosis (figure 2). WT mice or inflammasome-deficient mice were infected intranasally with *B. pseudomallei* (100 CFU) and their weight (not shown) and survival were monitored (figure 2A). All mice started to lose weight 2 days post-infection. Generally, mice that survived the infection started to recover weight 7 days post-infection. *Casp1*$^{-/-}$, *Nlrc4*$^{-/-}$, and *Asc*$^{-/-}$ mice were extremely susceptible to melioidosis compared to WT mice. *Nlrp3*$^{-/-}$ mice were also considerably more susceptible than WT mice but slightly more resistant than the other inflammasome deficient mice. Measurement of the bacterial burdens in lungs, spleens, and livers of infected mice 24 hours (data not shown) and 48 hours post-infection revealed that *Nlrc4*$^{-/-}$ and *Casp1*$^{-/-}$ mice carried considerably higher burdens in all three organs than WT mice (figure 2B). Surprisingly, the bacterial burden of *Asc*$^{-/-}$ and *Nlrp3*$^{-/-}$ mice was not significantly different from that of WT mice at the tested time points despite their higher mortality.

Cytokine levels were measured in bronchio-alveolar lavage fluids (BALF) obtained from infected mice (figure 2C). Confirming the *in vitro* results, IL-1β and IL-18 levels were severely reduced in *Asc*$^{-/-}$, *Casp1*$^{-/-}$ and *Nlrp3*$^{-/-}$ mice. In contrast, IL-1β and IL-18 were present in the lungs of *Nlrc4*$^{-/-}$ mice in amounts considerably higher than WT mice. Immunoblotting experiments confirmed that the IL-1β measured by ELISA was in fact the p17 mature form of IL-1β (figure 2D). Thus, although the *in vitro* experiments demonstrated that both the NLRP3 and the NLRC4 inflammasome contribute to IL-1β and IL-18 production in response to *B. pseudomallei* infection, it is the NLRP3 inflammasome that primarily mediates production of these cytokines *in vivo*. The levels of several other proinflammatory cytokines, including IL-1α (figure S2), were significantly elevated in *Nlrc4*$^{-/-}$ BALF. It is interesting to note that the levels of IL-18 in BALF of *Asc*$^{-/-}$ and *Casp1*$^{-/-}$ mice, although very low, were higher than uninfected mice suggesting the existence of inflammasome-independent mechanisms to produce IL-1β and IL-18, as it has been previously shown in models of highly neutrophilic inflammation [20-23].

Histological analysis of the infected lungs revealed extensive inflammatory cell infiltration in the lung parenchyma (data not shown). The area of the inflammatory nodules, relative to the total area of the lung lobe, was calculated for each given section and found to be significantly greater in *Nlrc4*$^{-/-}$ mice compared to WT mice (figure 2E). This result was consistent with the elevated levels of inflammatory cytokines and chemokines produced by *Nlrc4*$^{-/-}$ mice. Taken together these results suggest a scenario where failure of *Nlrc4*$^{-/-}$ infected macrophages to undergo pyroptosis results in higher bacterial burden and continued production of IL-1β and other factors that attract more inflammatory cells, perpetuating lung inflammation and promoting bacteria dissemination.

Thus, our results identified two distinct infammasome-mediated mechanisms that efficiently restrict *B. pseudomallei* growth and pathogenesis: production of the cytokines IL-1β and IL-18 and induction of pyroptosis. The high susceptibility of *Nlrp3*$^{-/-}$ and *Asc*$^{-/-}$ mice to meliodiosis is due to defective cytokine production while that of the *Nlrc4*$^{-/-}$ mice likely results from defective pyroptosis. *Casp1*$^{-/-}$ mice are impaired in both inflammasome effector mechanisms and, therefore, we predicted that they would

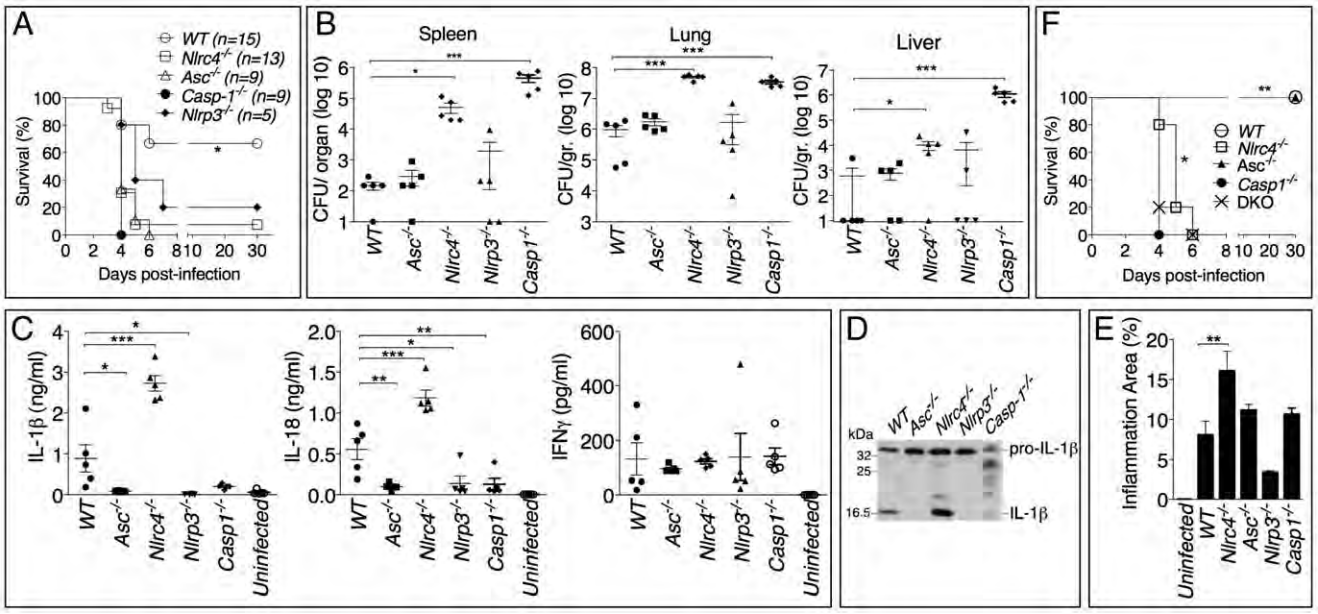

Figure 2. Differential contributions of NLRP3 and NLRC4 to melioidosis. (A) Mice were intranasally infected with *B. pseudomallei* (100 CFU) and their survival was monitored. *$p<0.05$ (Kaplan-Meier), WT compared to other genotypes (B) Mice were sacrificed 48 hours post-infection and the bacterial burdens were measured in organ homogenates. (C) Cytokines were measured in BALF obtained 48 hours post-infection. (D) Processing of IL-1β was detected by immunoblot in BALF from C. (E) Lung sections were stained with H&E and the total area of the inflammatory nodules was measured and expressed as percentage of the total lung lobe area. *$p<0.05$, **$p<0.01$, ***$p<0.001$ (1way ANOVA). (F) Mice were intranasaly infected with *B. pseudomallei* (25 CFU) and their survival was monitored. **$p<0.01$ WT compared to other genotypes and *p<0.05 *Casp-1*$^{-/-}$ compared to *Nlrc4*$^{-/-}$ (Kaplan-Meier).
doi:10.1371/journal.ppat.1002452.g002

be more vulnerable to *B. pseudomallei* than *Asc*$^{-/-}$ or *Il1-r1*$^{-/-}$*-Il-18*$^{-/-}$ double knock-out mice (DKO) (that are defective in cytokines but retain pyroptosis) or *Nlrc4*$^{-/-}$ mice (that retain IL-1β/IL-18 functionality but are deficient in pyroptosis). This prediction was found to be correct. As shown in figure 2F, when mice were infected with only 25 CFU (a non-lethal dose for WT mice) the mean time to death of *Nlrc4*$^{-/-}$ and *Il-1r1*$^{-/-}$*-Il-18*$^{-/-}$ DKO mice was slightly but significantly ($p<0.05$, Kaplan-Meier test) increased compared to *Casp1*$^{-/-}$ mice. Surprisingly, *Asc*$^{-/-}$ mice, which should be equivalent to DKO because of the absence of IL-1β or IL-18, survived the infection. This may be explained by the observation that IL-18, although drastically reduced, it is still detectable in *Asc*$^{-/-}$ mice at higher level than uninfected mice (figure 2C).

Role of IL-18 and IL-1β in murine melioidosis

We next analyzed the role of the inflammasome-dependent cytokines IL-1β and IL-18 during murine melioidosis. IL-18-deficient mice were extremely susceptible to *B. pseudomallei* infection even when infected with 25 CFU, a dose of bacteria that caused no mortality and only mild weight loss in WT mice (figure 3A). In contrast, *Il-1r1*$^{-/-}$ mice displayed increased resistance to *B. pseudomallei* infection compared to WT mice (figure 3A and see below). The survival of mice deficient in both IL-18 and IL-1RI (DKO) was indistinguishable from the *Il-18*$^{-/-}$ mice when the animals were infected with 100 CFU. However, in DKO mice infected with 25 CFU (figure 3A, right panel) the concomitant absence of IL-18 and IL-1RI provided a significant advantage over *Il-18*$^{-/-}$ mice ($p<0.05$) suggesting a detrimental role of IL-1RI-mediated signaling in melioidosis (see below).

Confirming the different susceptibilities of *Il-18*$^{-/-}$ and *Il-1r1*$^{-/-}$ mice to melioidosis, the bacterial burdens observed in the lungs, spleens, livers, and BALF of infected *Il-18*$^{-/-}$ mice were dramatically higher than that of WT mice even at early time points (24 hours post infection, figure 3B). In contrast, significantly lower amounts of bacteria were recovered 48 hours post infection from *Il-1r1*$^{-/-}$ mice compared to WT mice confirming their higher resistance.

Measurements of cytokines in the BALF obtained from mice at 24 and 48 hours post-infection (figure 3C) indicated that the levels of IFNγ were drastically reduced in *Il-18*$^{-/-}$ mice, a finding consistent with the established function of IL-18 as an IFNγ-inducing cytokine. Remarkably, IFNγ levels in *Il-1r1*$^{-/-}$ mice were greatly increased compared to WT mice. The levels of the neutrophil attractants Mip-2, KC, and IL-17 were also decreased in *Il-1r1*$^{-/-}$ mice and increased in *Il-18*$^{-/-}$ mice (figure S2). The number of inflammatory cells recovered from the BALF of infected *Il-1r1*$^{-/-}$ mice was significantly decreased compared to WT mice (see figure 4B, left panel). Histological analysis of the infected lungs revealed extensive inflammatory cell infiltration in the lung parenchyma of *Il-18*$^{-/-}$ mice (see figure 4C). The area of the inflammatory nodules, relative to the total area of the lung lobe, was calculated for each given section and found to be significantly greater in *Il-18*$^{-/-}$ mice compared to WT mice (figure 4D).

Considering that IFNγ is known to play a protective role during several bacterial infections, including *B. pseudomallei* [8–10], these results suggested that the reduced resistance of *Il-18*$^{-/-}$ mice to *B. pseudomallei* infection may be due to lack of IFNγ induction. To test this hypothesis, a group of *Il-18*$^{-/-}$ mice infected with *B. pseudomallei* were given daily intraperitoneal injections of either recombinant IFNγ or PBS. As shown in figure 3D, exogenous IFNγ completely protected the mice suggesting that IL-18 exerts its protective action primarily through induction of IFNγ.

Deleterious role of IL-1β in melioidosis

The results of figure 3 showed that *Il-1r1*$^{-/-}$ mice were more resistant to lung infection with *B. pseudomallei*. This appeared even

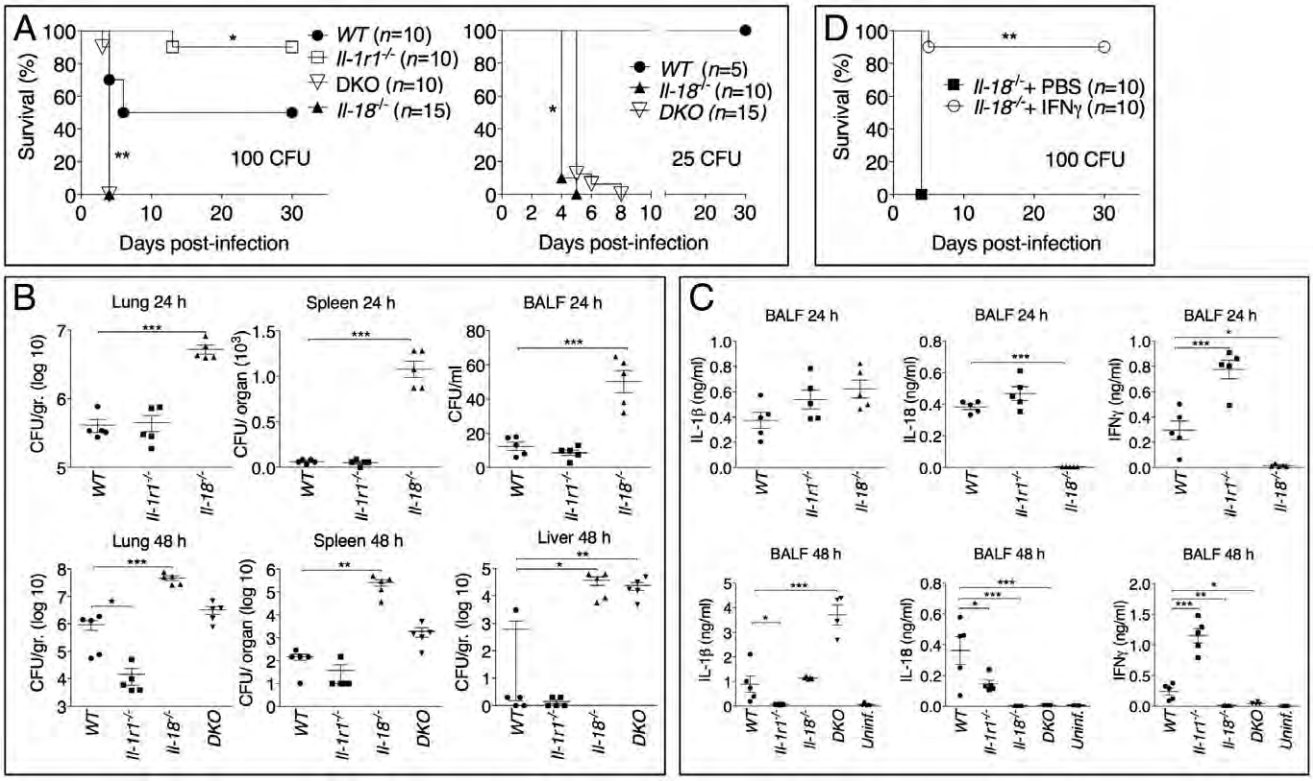

Figure 3. Differential contributions of IL-1 and IL-18 to melioidosis. (A) Mice were intranasaly infected with *B. pseudomallei* (100 CFU, left, or 25 CFU, right) and their survival was monitored. *$p<0.05$, **$p<0.01$ (Kaplan-Meier), WT compared to other genotypes (left), *Il-18*$^{-/-}$ compared to DKO (right). (B, C) Mice infected with *B. pseudomallei* (100 CFU) were sacrificed 24 hours or 48 hours postinfection and the bacterial burdens in organ homogenates and BALF (B) or cytokines levels in BALF (C) were measured. *$p<0.05$, **$p<0.01$, ***$p<0.001$ (1way ANOVA). (D) *Il-18*$^{-/-}$ mice were intranasally infected with *B. pseudomallei* (100 CFU) and their survival monitored. Mice were administered daily injections of PBS or IFNγ (1 μg) for the first 8 days. **$p<0.01$ (Kaplan-Meier).
doi:10.1371/journal.ppat.1002452.g003

more evident when mice were infected with higher doses of *B. pseudomallei* that killed all WT mice but only a fraction of the *Il-1r1*$^{-/-}$ mice (figure 4A). Recruitment of neutrophils, macrophages, and dendritic cells into alveolar spaces was decreased in *Il-1r1*$^{-/-}$ mice compared to WT mice (figure 4B, left graph). Lower levels of the neutrophil enzyme myeloperoxidase (MPO) were detected in the BALF of *Il-1r1*$^{-/-}$ mice compared to WT (figure S3). The extent of lung inflammation, as measured by the number and size of inflammatory nodules, was also significantly decreased in *Il-1r1*$^{-/-}$ mice (figure 4C, and 4D).

To further test the hypothesis that IL-1R-mediated signaling has a deleterious role in this model of melioidosis, WT mice were infected with 100 CFU *B. pseudomallei* and were given daily intraperitoneal injections of IL-1β or PBS (figure 4E). All mice that received the cytokine succumbed to the infection compared to significantly higher survival of the control group. Injection of IL-1β in non-infected mice had no deleterious effect aside from a transient, negligible weight loss (not shown). The bacteria burdens in organs of IL-1β-treated mice 72 hours post infection were dramatically higher than the control group and bacteremia was detected in IL-1β-treated mice but not control mice (figure 4F). Higher number of neutrophils, macrophages, and dendritic cells were found in the BALF of IL-1β-treated mice (figure 4B, center graph). This correlated with increased level of MPO in BALF (figure S3). The increased inflammatory cell recruitment to the lungs of IL-1β-treated mice was likely due to the induction, by IL-1β, of neutrophil chemoattractans KC (CXCL1) and MIP-2 (CXCL-2), which in fact were detected at very high levels in the BALF of IL-1β-treated mice (figure S2). Histological analysis of lung sections of mice treated with IL-1β showed a dramatic increase in the number and size of the foci of infiltrating inflammatory cells (figure 4C, lower left panels) and evidence of perivascular edema and airway obstruction (figure 4C, lower right panels).

If IL-1β in fact has a detrimental effect during melioidosis, inhibition of its activity should lower morbidity and mortality of mice infected with *B. pseudomallei*. As shown in figure 4G, administration of the IL-1 receptor antagonist IL-1ra protected mice from infection with lethal doses of *B. pseudomallei*. Mice treated with IL-1ra had decreased recruitment of inflammatory cells to the alveolar spaces (figure 4B, right graph) lower level of MPO in BALF (figure S3), and less severe lung pathology (data not shown).

Neutrophils fail to restrict *B. pseudomallei* intracellular growth and are resistant to pyroptosis

Surprisingly, in our experiments lower numbers of neutrophils in *Il-1r1*$^{-/-}$ mice correlated with lower bacterial burdens while IL-1β administration resulted in increased neutrophil recruitment *but also* increased bacterial burdens and systemic dissemination. These results would be consistent with the notion that neutrophils are not very effective at containing *B. pseudomallei* infection and, in fact, may foster its spread. In support of this idea, human neutrophils infected with *B. pseudomallei* underwent pyroptosis at a much slower rate than infected monocytes (figure 5A). Concomitantly, intra-

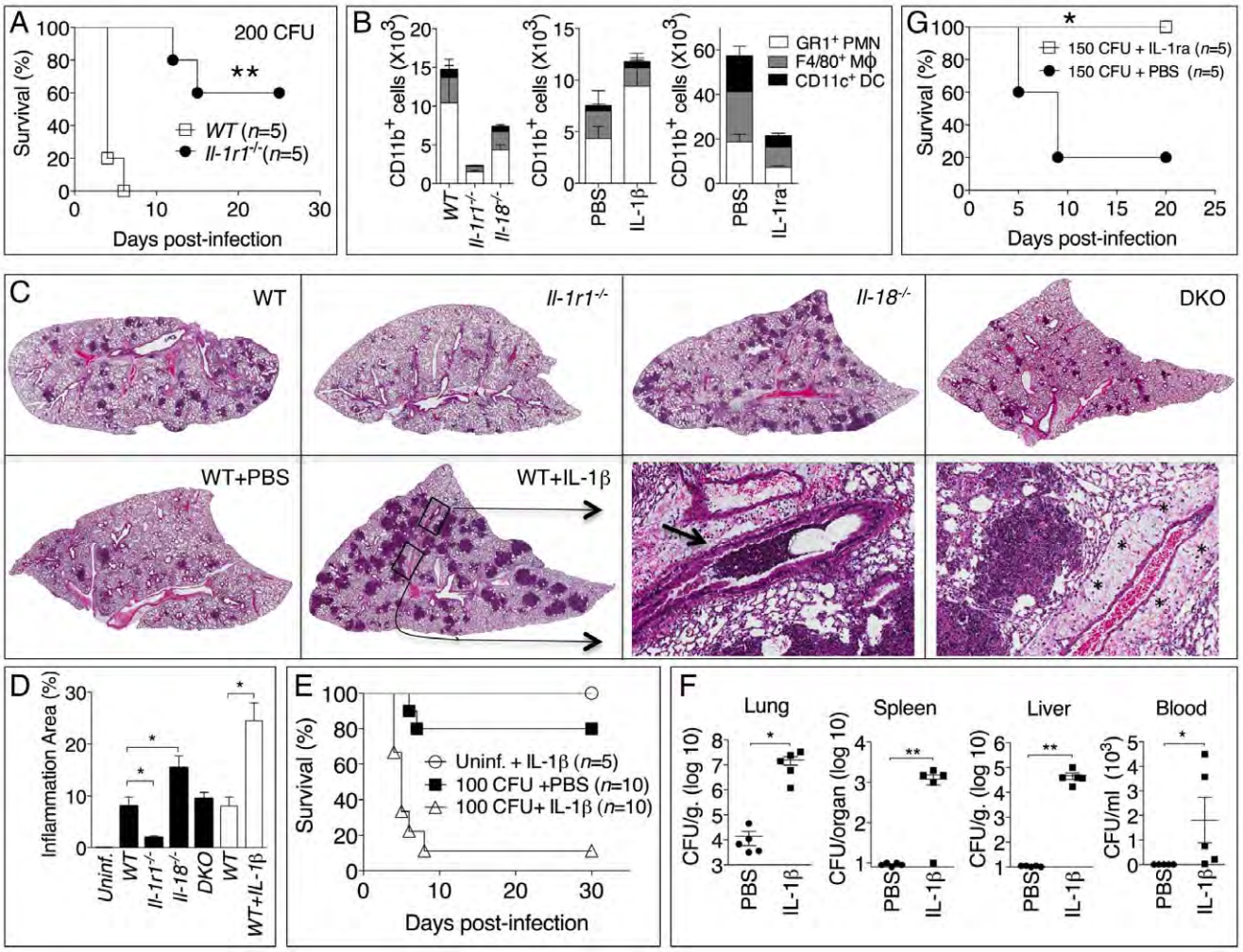

Figure 4. Deleterious role of IL-1β in melioidosis. (A) Mice were infected intranasally with *B. pseudomallei* (200 CFU) and their survival was monitored. (B) Flow cytometric analysis for myeloid cell composition of BALF obtained from the indicated infected mouse strains at 24 h (left); infected WT mice injected with IL-1β at 48 h (center graph); or infected WT mice injected with PBS or IL-1ra at 72 h. *$p<0.05$, ***$p<0.001$ (1way ANOVA). (C) Histopathology of lungs of infected mice of indicated genotype (0.8X magnification) at 48 h post-infection (upper row) or WT mice injected with PBS or IL-1β at 72 hrs post-infection (lower row). Bottom right panel shows 10X magnification of the indicated insets from WT+IL-1β showing airways obstruction (arrow head) and perivascular edema (asterisks). One image representative of five animals/experimental group. (D) The total area of the inflammatory nodules of lung sections of C was measured and expressed as percentage of the total lung lobe area. *$p<0.05$ (*t*-test). (E) WT mice were infected intranasally with *B. pseudomallei* (100 CFU) and received daily i.p. injections of PBS or IL-1β (1 μg). One group of mice were treated with IL-1β but not infected. **$p<0.01$, ***$p<0.001$ (Kaplan-Meyer). (F) Mice infected and IL-1β-injected as in E were sacrificed 72 h post-infection and the bacterial burden was measured in organs and blood. *$p<0.05$, **$p<0.01$ (1way ANOVA). (G) WT mice were infected intranasally with *B. pseudomallei* (150 CFU) and were administered daily injections of PBS or IL-1ra. *$p<0.05$ (Kaplan-Meyer).
doi:10.1371/journal.ppat.1002452.g004

cellular bacteria growth increased with time in infected neutrophils but decreased in monocytes. Consistent with previously published results [3], neutrophils did not express NLRC4 mRNA (figure 5B) suggesting they may be resistant to pyroptosis. Similar results were obtained using neutrophils and $CD11b^+$ monocytic cells isolated from mouse bone marrow (figure 5C). WT monocytes infected with *B. pseudomallei* underwent pyroptosis and failed to support bacteria replication whereas *Nlrc4*$^{-/-}$ cells were resistant to pyropotosis and supported *B. pseudomallei* intracellular replication. In contrast, both WT and *Nlrc4*$^{-/-}$ neutrophils did not undergo pyroptosis and supported *B. pseudomallei* intracellular replication to the same extent. These results suggest that the deleterious role of IL-1β during melioidosis may be due, in part, to excessive recruitment of neutrophils, a cell type that may be permissive for *B. pseudomallei* replication. We decided to test this hypothesis in *Nlrc4*$^{-/-}$ mice. As shown in figure 2E, infected *Nlrc4*$^{-/-}$ mice showed a significantly higher degree of lung inflammation. Consistent with higher neutrophil influx in the lung of *Nlrc4*$^{-/-}$ mice, the levels of the neutrophil enzyme MPO were significantly increased in their BALF compared to WT mice (figure 6A). To test the hypothesis that excessive neutrophil influx is deleterious during melioidosis, *Nlrc4*$^{-/-}$ mice were injected with IL-1ra or with antileukinate, a hexapeptide that acts as a CXCR2 neutrophil chemokine receptor antagonist. Both factors have been shown to inhibit neutrophil recruitment to inflammatory sites in different animal models including lung inflammation [24–26]. As shown in figure 6B, administration of IL-1ra or antileukinate protected *Nlrc4*$^{-/-}$ mice infected with low doses of *B. pseudomallei*. The number of inflammatory cells in the BALF of *Nlrc4*$^{-/-}$ mice treated with IL-1ra or antileukinate was reduced compared to mice who received

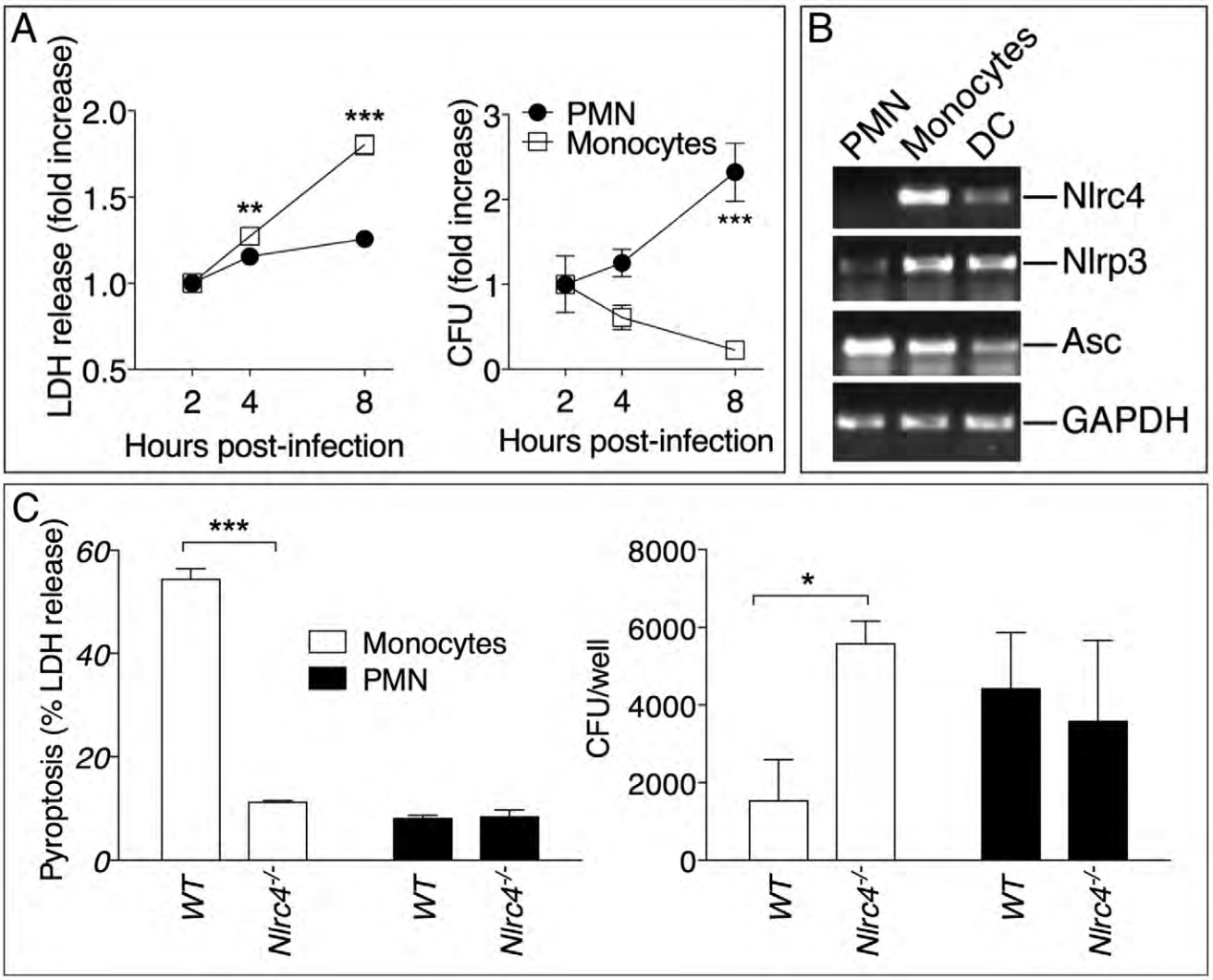

Figure 5. Neutrophils do not undergo pyroptosis and fail to restrict *B. pseudomallei* replication. (A) Human neutrophils or monocytes were infected with *B. pseudomallei* (MOI 50) and pyroptosis and intracellular bacterial growth were measured at the indicated time points. One experiment representative of two is shown. Data are shown as the fold increase normalized to the 2 h values. (B) RT-PCR analysis of total RNA from the indicated cell types. (C) WT or *Nlrc4*$^{-/-}$ mouse neutrophils and monocytic cells were infected with *B. pseudomallei* (MOI 50) and pyroptosis and intracellular bacterial growth were measured 8 hours post infection. * $p<0.05$, ** $p<0.01$, *** $p<0.001$ (2way ANOVA, post-test Bonferroni).
doi:10.1371/journal.ppat.1002452.g005

PBS injection (figure 6C) and lower levels of MPO were detected in the BALF of injected mice (figure S3). Moreover, systemic spread of bacteria to spleen or liver was reduced by administration of either drug (figure 6D).

Discussion

The inflammatory response to infection consists of several protective effector mechanisms that must be activated and orchestrated in order to maximize microbicidal functions and stimulation of adaptive immunity while, at the same time, minimize damage to the host tissues. Alteration in this balance may result in excessive and non-resolving inflammation that leads to severe morbidity and mortality [27]. It is becoming clear that to be effective but non-pathogenic the inflammatory response must be tailored to each specific pathogen. Here we have analyzed the role of a very important inflammatory pathway during infection with the lung pathogen *B. pseudomallei*. Using a murine model of melioidosis we have determined the role of various components of the inflammasome and the downstream effector mechanisms (production of IL-1β, IL-18, and pyroptosis) and we report several novel discoveries that greatly increase our understanding of the pathogenesis of melioidosis (see model in figure 7).

First, we found that both NLRC4 and NLRP3 play non-redundant roles during detection of *B. pseudomallei*. Analysis of *in vitro* infected macrophages or dendritic cells allowed us to estimate the relative contribution of NLRC4 and NLRP3 to IL-1β production. Our findings indicated that production of IL-1β is primarily dependent on the NLRP3 inflammasome. During the early phase of the infection the NLRC4 inflammasome also significantly contributes to IL-1β production. We posit that this pattern likely reflects the fact that the NLRC4 inflammasome responds to T3SS deployment, which occurs early in the infection cycle, while activation of NLRP3 may require escape from the phagosome, which is a relatively slower event [28]. *B. pseudomallei* , including the strain used in our study, possesses at least three T3SS

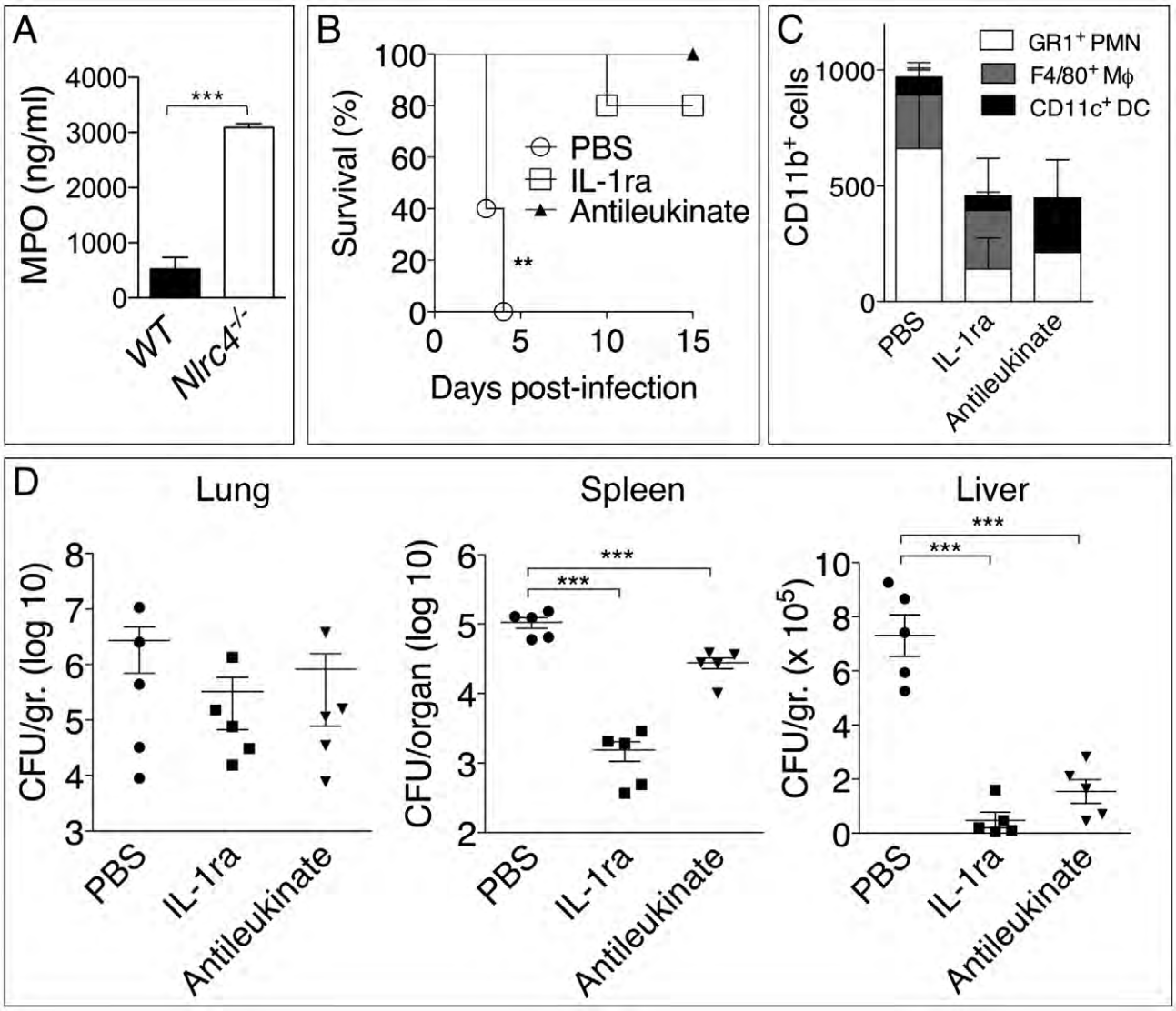

Figure 6. Inhibition of neutrophil recruitment to the lung protects *Nlrc4*$^{-/-}$ mice from melioidosis. (A) Myeloperoxidase was measured in BALF of WT and *Nlrc4*$^{-/-}$ mice. (B) *Nlrc4*$^{-/-}$ mice were infected intranasally with *B. pseudomallei* (25 CFU) and were administered daily injections of PBS or IL-1ra (i.p.) or antileukinate (s.c.). $^{**}p<0.01$, $^{***}p<0.001$ (Kaplan-Meyer). (C) Flow cytometric analysis for myeloid cell composition of BALF obtained from *Nlrc4*$^{-/-}$ mice infected and treated with IL-1ra or antileukinate. (D) *Nlrc4*$^{-/-}$ mice infected and treated with IL-1ra or antileukinate were sacrificed 48 h post-infection and the bacterial burden was measured in organs. $^{*}p<0.05$, $^{**}p<0.01$ (1way ANOVA).
doi:10.1371/journal.ppat.1002452.g006

gene clusters, one of which is similar to the *Salmonella* SP-1 pathogenicity island and has been shown to be an important virulence factor required for escape from the phagosome, induction of IL-1β production, and pathogenicity [13,28]. In addition to mediating host recognition of cytosol-delivered flagellin, NLRC4 also recognizes a structural motif found in the basal body rod components of the T3SS of various bacteria, including *B. pseudomallei* [29]. We have determined (data not shown) that transfection of *B. pseudomallei* flagellin protein into the cytoplasm of BMDC leads to NLRC4-dependent production of IL-1β. This result agrees with previously published evidence and indicates that *B. pseudomallei* (like some other bacteria) expresses multiple factors (e.g. flagellin, basal rods) that are recognized by the NLRC4 inflammasome. The mechanism responsible for NLRP3 activation by *B. pseudomallei* remains unclear.

In addition to controlling IL-1β and IL-18 production, NLRC4 also mediates pyroptosis, a form of cell death that is an effective mechanism to restrict growth and dissemination of intracellular bacteria [3]. Here we showed that *B. pseudomallei*-induced pyroptosis was caspase-1-dependent but ASC-independent, in agreement with works that showed ASC redundancy for pyroptosis induced by other bacteria [16–19]. However, the fact that production of IL-1β in response to *B. pseudomallei* infection is seriously compromised in *Asc*$^{-/-}$ cells indicates that this adaptor molecule plays a critical role in NLRC4-mediated cytokine production and suggests that NLRC4 can form two distinct inflammasomes: one that contains ASC and regulates IL-1β processing, and one devoid of ASC that activates caspase-1 and triggers pyroptosis, as recently proposed [30]. It has been recently shown [4,5] that NAIP molecules determine the specificity of NLRC4 for its activators and, we would further speculate, for its down-stream effector mechanisms. Whether NLRC4 relies on other molecules to recognize *B. pseudomallei* remains to be ascertained. We tested the susceptibility to *B. pseudomallei* of

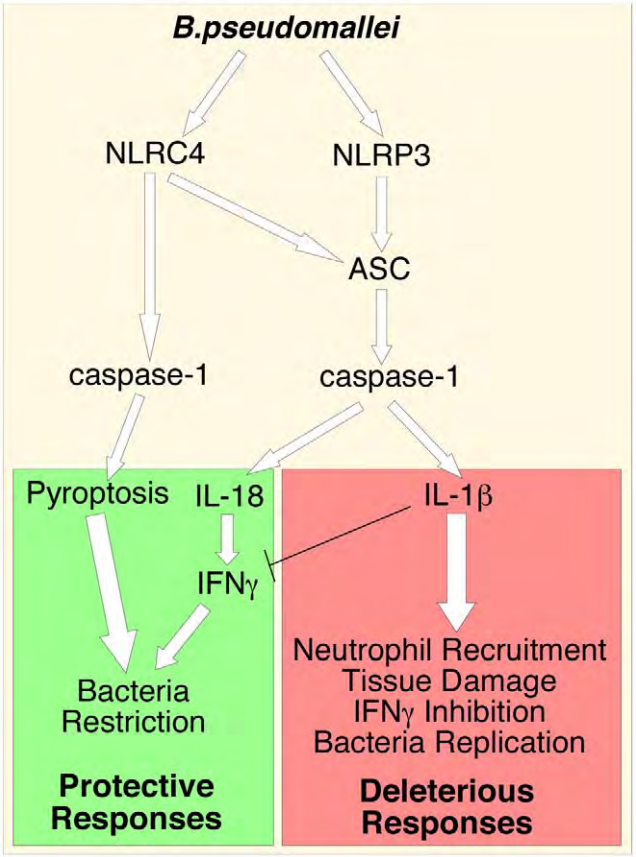

Figure 7. Inflammasomes-dependent protective and deleterious responses activated by *B. pseudomallei*. *B. pseudomallei* induces NLRC4-dependent pyroptosis that restricts intracellular bacterial growth. Activation of NLRP3-inflammasome leads to production of IL-18 and IL-1β. IL-18 is protective because of its induction of IFNγ. IL-1β deleterious role may be due to several reasons including excessive recruitment of neutrophils, which may support intracellular growth of *B. pseudomallei*, tissue damage, and inhibition of IFNγ production.
doi:10.1371/journal.ppat.1002452.g007

C57BL/6J-Chr13$^{A/J}$/NaJ mice, a consomic C57BL/6 strain that carries the A/J NAIP5 allele that renders them susceptible *to Legionella* infection [31-34], and found that they were indistinguishable from WT mice (data not shown).

Analysis of inflammasomes-deficient mice intranasaly infected with *B. pseudomallei* confirmed the importance of ASC, caspase-1, and both NLRP3 and NLRC4 inflammasomes for resistance to melioidosis. However, quite surprisingly, although production of IL-1β and IL-18 *in vitro* is mediated by both NLRP3 and NLRC4, *in vivo* it is exclusively dependent on the NLRP3-ASC-caspase-1 inflammasome (figure 2C). In contrast, *Nlrc4*$^{-/-}$ mice produce these cytokines in amounts that exceed even those detected in WT mice. Remarkably, despite the abundance of IL-1β and IL-18, *Nlrc4*$^{-/-}$ mice were dramatically more susceptible to melioidosis than WT mice, rapidly succumbed to the infection, and had very high organ's bacteria burden and worst neutrophilic lung inflammation. Thus, the critical role of NLRC4 during melioidosis is independent of IL-1β and IL-18 production. Rather, our results suggest that pyroptosis, which we show is defective in *Nlrc4*$^{-/-}$ cells, is a critical NLRC4 effector mechanism to fight *B. pseudomallei* and, in its absence, bacterial replication and IL-1β production proceeds unrestrained causing severe inflammation, morbidity and mortality. Moreover, our analysis indicates that pyroptosis and IL-18 are both required and contribute equally to resistance to melioidosis. Thus, deficiency of either is equally lethal while deficiency of both (*Casp1*$^{-/-}$ mice) further worsens the outcome. It is important to emphasize that our study is the first to demonstrate the importance of pyroptosis in the context of an infection with a clinically relevant human pathogen that has not been genetically manipulated, as opposed to the previous seminal work by Miao et al. [3] that elegantly employed genetically manipulated bacteria and mouse strains to identify pyroptosis as an effective innate immune defence mechanism against bacterial infections. Previous reports have demonstrated activation of both NLRP3 and NLRC4 inflammasomes in response to infection with *Legionella pneumophila* [16], *Listeria monocytogenes* [35], and *Salmonella typhimurium* [36]. However, in those infection models NLRP3 and NLRC4 appeared to play redundant roles while in our model we were able to assign distinct functions to each inflammasome.

A great number of publications have documented the role of IL-18 and IL-1β during infections with a variety of pathogens. Almost invariably, both cytokines were found to have a protective function. Remarkably, our results show that while *Il-18*$^{-/-}$ mice are profoundly vulnerable to melioidosis, as previously shown [37], *Il-1r1*$^{-/-}$ mice were unexpectedly more resistant than WT mice. The protective role of IL-18 during melioidosis appears to be related to its ability to induce IFNγ, as administration of exogenous IFNγ completely rescued the survival of *Il-18*$^{-/-}$ infected mice. IFNγ activates the microbicidal activity of macrophages and has been shown to be important for resistance against infection with many pathogens including *B. pseudomallei* [8–10]. It is interesting and surprising to see that *Asc*$^{-/-}$ and *Nlrp3*$^{-/-}$ mice, which are defective in IL-1β and IL-18 production, are more resistant to *B. pseudomallei* than mice lacking IL-18. It is worth noting that although IL-18 production is drastically reduced in *Asc*$^{-/-}$ and *Nlrp3*$^{-/-}$ mice, it is still detectable in these mice at higher level than uninfected mice. It is conceivable that this inflammasome-independent production of IL-18 may be sufficient to provide some level of protection to *Asc*$^{-/-}$ and *Nlrp3*$^{-/-}$ mice against infection with low *B. pseudomallei* CFU.

Our discovery that *Il-1r1*$^{-/-}$ mice were more resistant than WT to *B. pseudomallei* infection is quite surprising considering that this cytokine has been shown to be protective in several bacterial, viral, and fungal infection models [38]. Studies in humans have also shown that inhibition of the function of IL-1 using the IL-1R antagonist IL-1ra (Kineret) is associated with increased susceptibility to bacterial infection. Infected *Il-1r1*$^{-/-}$ mice had lower BALF levels of proinflammatory cytokines as well as a reduction of neutrophil influx into the lungs, bacterial burdens, and lung pathology. Consistent with a deleterious role of IL-1β in melioidosis, administration of recombinant IL-1β drastically increased mortality, inflammation, pathology, and bacteria burdens while administration of IL-1ra (Kineret) rescued the survival of WT mice infected with a lethal dose of *B. pseudomallei*.

The reason for the detrimental effect of IL-1β during melioidosis is unclear and it is likely that several factors determine this outcome. IL-1β is one of the most powerful proinflammatory cytokines, it affects virtually every organ, and several human pathologies are primarily driven by unrestrained IL-1β production. One possible mechanism to account for IL-1β's deleterious role in melioidosis may be related to its ability to inhibit IFNγ production through the induction of the cycloxigenase COX-2 and release of prostaglandin PGE_2 [39,40]. Our observation that the level of IFNγ, a protective factor against *B. pseudomallei*, was significantly higher in infected *Il-1r1*$^{-/-}$ than WT mice (figure 3C) supports this type of scenario in melioidosis. Interestingly IL-8, a potent neutrophil chemoattractant, was shown to enhance the

intracellular growth and survival of *B. cepacia* in bronchial epithelial cell lines [41]. Whether IL-1β promotes *B. pseudomallei* intracellular replication is not known but our preliminary results indicated that induction of pyroptosis by *B. pseudomallei* was not affected by IL-1β.

IL-1β regulates neutrophil recruitment to inflammatory sites through multiple mechanisms including induction of KC, MIP-2, and IL-17, inflammatory mediators whose expression in our experiments correlated with the presence/absence of IL-1RI-mediated signaling. Excessive PMN recruitment is known to cause tissue damage leading to functional impairment of multiple organs, including the lungs [42,43]. One of the most remarkable observations reported here is that the absence of IL-1 signaling was associated with reduced lung neutrophilic inflammation *but also* lower bacterial burdens in the lungs (figure 3B, 4B). Conversely, IL-1β administration resulted in increased neutrophil recruitment *but also* increased bacterial burdens and systemic dissemination. These results would be consistent with the idea that neutrophils are not very effective at containing *B. pseudomallei* infection and, in fact, may foster its spread despite their strong microbicidal activities. This notion is supported by our observation that human or mouse neutrophils infected with *B. pseudomallei* failed to undergo pyropotosis (figure 5), consistent with the finding that neutrophils do not express NLRC4 [3]. At the same time, intracellular *B. pseudomallei* replication proceeded unaffected in both WT and *Nlrc4*$^{-/-}$ neutrophils in agreement with a report that showed that *B. pseudomallei* is intrinsically resistant to killing by infected PMN [44]. In support for a deleterious role of neutrophils in melioidosis we found that inhibition of their recruitment by administration of IL-1ra or the CXCR2 neutrophil chemokine receptor antagonist antileukinate protected *Nlrc4*$^{-/-}$ mice from infection with low doses of *B. pseudomallei* and decreased systemic spread of bacteria (figure 6).

Taken together our results suggest the following scenario: failure of *Nlrc4*$^{-/-}$ infected macrophages to undergo pyroptosis results in higher bacteria burden and continued production of IL-1β and other factors that attract more inflammatory cells, including neutrophils, perpetuating excessive lung inflammation and promoting bacteria dissemination. It is tempting to speculate that IL-1β promotes *B. pseudomallei* growth possibly by increasing the local pool of infectable permissive cells, including PMN. Our conclusion that neutrophils are a permissive cell type for *B. pseudomallei* replication seems to contrast with a report [45] that indicated that depletion of neutrophils resulted in severe increase in mortality in a model of murine melioidosis. However, caution should be used in the interpretation of these types of experiments because systemic depletion of neutrophils devoids the host not only of their microbicidal function but also of the many immunomodulatory functions these cells exert [46]. Of note, mice deficient in osteopontin, a pleiotropic cytokine that is chemotactic for neutrophils, were shown to be more resistant to *B. pseudomallei* infection [47], supporting our conclusion that neutrophils have a detrimental role in melioidosis.

The notion that excessive inflammation may be detrimental in certain infection models is well accepted. For example, TLR-mediated signaling negatively affects the outcome of infections with West Nile Virus [48] or influenza virus [49]. The fact that IL-1β is deleterious in melioidosis but protective against other lung pathogens like *Klebsiella*, *Francisella*, *Mycobacterium*, Respiratory Syncytial Virus, and influenza virus likely reflects differences between the virulence strategy of *B. pseudomallei* and those other pathogens. The intensity, kinetics, and quality of the inflammatory response elicited by *B. pseudomallei* and its ability to suppress the induction of anti-inflammatory circuitries are phenomena that we are interested to investigate in detail. Despite an extensive literature search we could identify only a single report [26] where IL-1β was shown to be deleterious in bacterial infections. It was demonstrated that this cytokine had a negative effect on bacterial clearance in a model of pneumonia caused by *Pseudomonas aeruginosa*, an organism that shares features with *Burkholderia*, which was in fact previously classified in the *Pseudomonas* genus. Surprisingly, the same group also reported a deleterious role for IL-18 in this type of infection [50], a further indication that each pathogen displays unique virulence strategies. It has been shown that activation of the inflammasome exacerbates inflammation without restricting bacterial growth in a model of *Mycobacterial* infection [51]. That report did not examine the role of IL-1β but other work showed it is protective during tuberculosis [23].

This is the first report that has analyzed in detail the role of the inflammasome during melioidosis. Previous work has implicated caspase-1 [52] and IL-18 [37] in this infectious disease although the pathways that led to their activation were not investigated. Other species of *Burkholderia* have been used as model organisms to study aspects of inflammasome biology. Surprisingly, *B. thailandensis*, which is has been used as a model for melioidosis although it rarely causes disease in humans, was reported to cause similar disease in WT and IL-18- IL-1β-double deficient mice [3] suggesting that species of *Burkholderia* other than *B. pseudomallei* may not be reliable models for melioidosis.

In summary, our work shows that NLRP3 and NLRC4 play non-redundant roles during *B. pseudomallei* infection by differentially regulating pyroptosis and production of IL-1β and IL-18; it demonstrates that pyroptosis is an efficient effector mechanism to restrict *in vivo* bacterial growth and dissemination; it identifies a deleterious role of IL-1β in melioidosis possibly due to excessive recruitment of neutrophils, a cell type that may be permissive to replication of *B. pseudomallei*; and, finally, it indicates that inhibition of IL-1RI-mediated signaling may be a beneficial therapeutical approach for the treatment of melioidosis.

Materials and Methods

Ethics statement

All the animal experiments described in the present study were conducted in strict accordance with the recommendations in the *Guide for the Care and Use of Laboratory Animals* of the National Institutes of Health. All animal studies were conducted under a protocol approved by the University of Tennessee Health Science Center (UTHSC) Institutional Animal Care and Use Committee (IACUC, protocol #1854). All efforts were made to minimize suffering and ensure the highest ethical and humane standards. Research involving human blood is exempt from the human subjects regulations. Human neutrophils and monocytes were isolated from healthy donors Leukopacks obtained from Lifeblood Mid-South Regional Blood Center, Memphis TN. All leukopaks are obtained anonymously. The gender, race, and age of each donor are unknown to the investigators.

Mice

C57BL/6, *Il-1r1*$^{-/-}$, *Il-18*$^{-/-}$, C57BL/6J-Chr13$^{A/J}$/NaJ mice were purchased from Jackson lab. *Il-18*$^{-/-}$-*Il-1r1*$^{-/-}$ double deficient mice (DKO) were obtained by crossing the parental single knock-out mice. *Asc*$^{-/-}$, *Nlrp3*$^{-/-}$, *Nlrc4*$^{-/-}$ (from Vishva Dixit, Genentec) and *Casp1*$^{-/-}$ (from Fayyaz Sutterwala) were bred in our facility. All mouse strains were on C57BL/6 genetic background and were bred under specific pathogen-free conditions. Age-(8–12 weeks old) and sex-matched animals were used in all experiments. Generally, experimental groups were composed of at least 5 mice.

Animal and *in vitro* experiments involving *B. pseudomallei* were performed under biosafety level 3 conditions in accordance with standard operating procedures approved by the Regional Biocontainment Laboratory at UTHSC.

Bacteria, mice infection, and treatments

For all experiment the *B. pseudomallei* 1026b strain (a clinical virulent isolate) was used. Bacteria were grown in Luria broth (Difco) to mid-logarithmic phase, their titer was determined by plating serial dilutions on LB agar, and stocks were maintained frozen at −80°C in 20% glycerol. No loss in viability was observed over prolonged storage. For infections, frozen stocks were diluted in sterile PBS to the desired titer. Aliquots were plated on LB agar to confirm actual CFU. Mice were anesthetized with isoflurane using a Surgivet apparatus and 50 µl of bacteria suspension were applied to the nares. In some experiments, mice were injected i.p. daily with recombinant mouse IL-1β (1 µg) or IFNγ (1 µg). IL-1ra (Biovitrum) was administered by alternating s.c. and i.p. injections every 12 hours (60 mg/kg body weight). Antileukinate (American Peptide Company) was administered by s.c. injection (8 mg/kg body weight).

Generation of mouse BMDM and BMDC

Mouse macrophages or dendritic cells were generated by incubating bone marrow cells in RPMI 1640-10%FCS supplemented with either rmM-CSF or rmGM-CSF (20 ng/ml) for 8 days, respectively.

Isolation of mouse neutrophils

Neutrophils and monocytic cells were isolated from the bone marrow cells of WT or *Nlrc4*$^{-/-}$ mice using Miltenyi Ly6G microbeads. Flow-through cells, consisting mostly of monocytic cells, were further purified using Miltenyi CD11b microbeads.

Isolation of human neutrophils and monocytes

Human neutrophils and monocytes were isolated from healthy donors Leukopacks obtained from Lifeblood Mid-South Regional Blood Center, Memphis TN. Blood was mixed with Isolymph (CTL Scientific Supply Corp.) (5:1 ratio) and RBC were allowed to sediment for 60 min at RT. The leukocytes-enriched supernatant was washed, resuspended in PBS, and stratified over Isolymph cushion and centrifuged at 1,350 rpm for 40 min. The cell pellet containing RBC and neutrophils was treated with 0.2% NaCl for 30 seconds to lyse RBC and immediatedly treated with an equal volume of 1.6% NaCl. The PBMC containing ring from the Isolymph centrifugation step was collected, washed, and monocytes were purified using CD14 microbeads (Miltenyi). The procedure routinely yield populations of purity greater than 95%.

Pyroptosis and intracellular bacteria growth (kanamycin protection assay)

Release of LDH in tissue culture media, a reflection of pyroptosis, was measured using the Roche Cytotox detection kit. BMDM, PMN, or monocytes (5×10^5 cells) were plated in 24 well plates. Bacteria at different MOI were added to the cell culture and the plates were centrifuged at 1500 rpm for 10 minutes to maximize and synchronize infection and incubated for 30 minutes at 37°C. Cells were washed with PBS to remove extracellular bacteria and medium containing kanamycin (200 µg/ml) was added to inhibit extracellular bacteria growth. Media were collected at 1, 2, 4, 8, 12 hours post infection for LDH measurement. Cells were lysed in PBS-2% saponin-15% BSA and serial dilutions of the lysates were plated on LB agar plates containing streptomycin (100 µg/ml) using the Eddy Jet Spiral Plater (Neutec). Bacterial colonies were counted 48 hours later using the Flash & Grow Automated Bacterial Colony Counter (Neutec).

Determination of bacteria growth in tissue culture and organs

Organs aseptically collected were weighted and homogenized in 1 ml PBS using 1 mm zirconium beads and the Mini16 bead beater. Serial dilutions were plated as described above.

Western blot

Conditioned supernatants were separated by 12% PAGE electrophoresis, transferred to PVDF membranes, and probed with rabbit anti-caspase-1 (Upstate Biotechnologies) or goat anti-mIL-1β (R&D Systems).

BALF collection and cytokines measurements

BALF were collected from euthanized mice by intratracheal injection and aspiration of 1 ml PBS. Cytokines levels in tissue culture conditioned supernatants and BALF were measured using the Milliplex mouse cytokine/chemokine panel (Millipore) and confirmed by ELISA using the following paired antibodies kits: mIL-1β and mIFNγ (eBioscience), mIL-18 (MBL Nagoya, Japan). MPO level in BALF were measured using the HyCult Biotech ELISA kit.

Flow cytometry

Cells obtained from BALF were counted and stained with CD45, CD11b, CD11c, F4/80, GR1 (Ly6G), and analyzed with a LSRII BD flow cytometer.

Histology and measurement of area of inflammatory foci

Formalin-fixed paraffin-embedded lung sections were stained with H&E and scanned using the Aperio Scanscope XT. The Aperio ImageScope software was used to quantitate the area of the inflammatory foci compared to the total lung lobe area. Results from lungs from 5 animals per group were combined.

RT-PCR

Total RNA was extracted using Trizol (Invitrogen) and 100 ng were amplified (27 cycles) using Superscript III One-step RT-PCR (Invitrogen) and primers specific for human Nlrc4, Nlrp3, Asc, and GAPDH (primers' sequence available upon request).

Statistical analysis

All data were expressed as mean ± S.E.M. Survival curves were compared using the log rank Kaplan-Meier test. 1way ANOVA and Tukey Post-test was used for analysis of the rest of data unless specified in the figure legends. Significance was set at $p<0.05$. Statistical analyses were performed using the GraphPad Prism 5.0.

Accession numbers

UniProtKB/Swiss-Prot ID: IL-1β, P10749; IL-1R1, P13504; IL-18, P70380; NLRP3, Q8R4B8; NLRC4, Q3UP24; ASC, Q9EPB4; Casp-1, P29452; NAIP5, Q8CGT2.

Supporting Information

Figure S1 NLRP3 and NLRC4 differentially regulate production of IL-1β and IL-18 and pyroptosis. BMDC were infected with *B. pseudomallei* at MOI of 10. (A) Secretion of mature IL-1β was measured in conditioned supernatants at the

indicated times. (B) Processing of IL-1β and caspase-1 were detected by immunoblot in 8h conditioned supernatants from A. (C) BMDC infected with *B. pseudomallei* (MOI 10) were lysed at the indicated time points after infection and intracellular bacterial growth was quantitated (upper panel). Induction of pyroptosis was measured as LDH release in conditioned supernatants (lower panel). One experiment representative of four (A) or three (C) is shown. *$p<0.05$, **$p<0.01$, ***$p<0.001$ (1way ANOVA).
(TIF)

Figure S2 Cytokines and chemokines were measured in BALF obtained from the indicated mouse strains 48 hours or 72 hours post-infection, as shown. *$p<0.05$, **$p<0.01$, ***$p<0.001$ (1way ANOVA).
(TIF)

Figure S3 Myeloperoxidase (MPO) was measured in BALF of the indicated mouse strains corresponding to the experiments of figures 3B, 4F, and 6D. *p<0.05, **p<0.01, ***p<0.001 (1way ANOVA).
(TIF)

Acknowledgments

The authors wish to thank Jennifer Stabenow and Lilian Zalduondo at the UTHSC Regional Biocontainment Laboratory for help and training on biocontainment techniques and Hossam Abdelsamed for flow cytometry analysis.

Author Contributions

Conceived and designed the experiments: FR. Performed the experiments: ICO MS MAM LdB FR. Analyzed the data: ICO MS MAM LdB FR. Wrote the paper: FR.

References

1. Davis BK, Wen H, Ting JP (2011) The inflammasome NLRs in immunity, inflammation, and associated diseases. Annu Rev Immunol 29: 707–735.
2. Brodsky IE, Medzhitov R (2011) Pyroptosis: macrophage suicide exposes hidden invaders. Curr Biol 21: R72–75.
3. Miao EA, Leaf IA, Treuting PM, Mao DP, Dors M, et al. (2010) Caspase-1-induced pyroptosis is an innate immune effector mechanism against intracellular bacteria. Nat Immunol 11: 1136–1142.
4. Kofoed EM, Vance RE (2011) Innate immune recognition of bacterial ligands by NAIPs determines inflammasome specificity. Nature 477: 592–595.
5. Zhao Y, Yang J, Shi J, Gong YN, Lu Q, et al. (2011) The NLRC4 inflammasome receptors for bacterial flagellin and type III secretion apparatus. Nature 477: 596–600.
6. Cheng AC, Currie BJ (2005) Melioidosis: epidemiology, pathophysiology, and management. Clin Microbiol Rev 18: 383–416.
7. Wiersinga WJ, van der Poll T, White NJ, Day NP, Peacock SJ (2006) Melioidosis: insights into the pathogenicity of Burkholderia pseudomallei. Nat Rev Microbiol 4: 272–282.
8. Miyagi K, Kawakami K, Saito A (1997) Role of reactive nitrogen and oxygen intermediates in gamma interferon-stimulated murine macrophage bactericidal activity against Burkholderia pseudomallei. Infect Immun 65: 4108–4113.
9. Santanirand P, Harley VS, Dance DA, Raynes JG, Drasar BS, et al. (1997) Interferon-gamma mediates host resistance in a murine model of melioidosis. Biochem Soc Trans 25: 287S.
10. Jones AL, Beveridge TJ, Woods DE (1996) Intracellular survival of Burkholderia pseudomallei. Infect Immun 64: 782–790.
11. Reckseidler SL, DeShazer D, Sokol PA, Woods DE (2001) Detection of bacterial virulence genes by subtractive hybridization: identification of capsular polysaccharide of Burkholderia pseudomallei as a major virulence determinant. Infect Immun 69: 34–44.
12. DeShazer D, Brett PJ, Woods DE (1998) The type II O-antigenic polysaccharide moiety of Burkholderia pseudomallei lipopolysaccharide is required for serum resistance and virulence. Mol Microbiol 30: 1081–1100.
13. Warawa J, Woods DE (2005) Type III secretion system cluster 3 is required for maximal virulence of Burkholderia pseudomallei in a hamster infection model. FEMS Microbiol Lett 242: 101–108.
14. Liu B, Koo GC, Yap EH, Chua KL, Gan YH (2002) Model of differential susceptibility to mucosal Burkholderia pseudomallei infection. Infect Immun 70: 504–511.
15. Hoppe I, Brenneke B, Rohde M, Kreft A, Haussler S, et al. (1999) Characterization of a murine model of melioidosis: comparison of different strains of mice. Infect Immun 67: 2891–2900.
16. Case CL, Shin S, Roy CR (2009) Asc and Ipaf Inflammasomes direct distinct pathways for caspase-1 activation in response to Legionella pneumophila. Infect Immun 77: 1981–1991.
17. Mariathasan S, Newton K, Monack DM, Vucic D, French DM, et al. (2004) Differential activation of the inflammasome by caspase-1 adaptors ASC and Ipaf. Nature 430: 213–218.
18. Suzuki T, Franchi L, Toma C, Ashida H, Ogawa M, et al. (2007) Differential regulation of caspase-1 activation, pyroptosis, and autophagy via Ipaf and ASC in Shigella-infected macrophages. PLoS Pathog 3: e111.
19. Franchi L, Stoolman J, Kanneganti TD, Verma A, Ramphal R, et al. (2007) Critical role for Ipaf in Pseudomonas aeruginosa-induced caspase-1 activation. Eur J Immunol 37: 3030–3039.
20. Fantuzzi G, Ku G, Harding MW, Livingston DJ, Sipe JD, et al. (1997) Response to local inflammation of IL-1 beta-converting enzyme- deficient mice. J Immunol 158: 1818–1824.
21. Coeshott C, Ohnemus C, Pilyavskaya A, Ross S, Wieczorek M, et al. (1999) Converting enzyme-independent release of tumor necrosis factor alpha and IL-1beta from a stimulated human monocytic cell line in the presence of activated neutrophils or purified proteinase 3. Proc Natl Acad Sci U S A 96: 6261–6266.
22. Guma M, Ronacher L, Liu-Bryan R, Takai S, Karin M, et al. (2009) Caspase 1-independent activation of interleukin-1beta in neutrophil-predominant inflammation. Arthritis Rheum 60: 3642–3650.
23. Mayer-Barber KD, Barber DL, Shenderov K, White SD, Wilson MS, et al. (2010) Caspase-1 independent IL-1beta production is critical for host resistance to mycobacterium tuberculosis and does not require TLR signaling in vivo. J Immunol 184: 3326–3330.
24. Maus U, von Grote K, Kuziel WA, Mack M, Miller EJ, et al. (2002) The role of CC chemokine receptor 2 in alveolar monocyte and neutrophil immigration in intact mice. Am J Respir Crit Care Med 166: 268–273.
25. Hayashi S, Yatsunami J, Fukuno Y, Kawashima M, Miller EJ (2002) Antileukinate, a hexapeptide inhibitor of CXC-chemokine receptor, suppresses bleomycin-induced acute lung injury in mice. Lung 180: 339–348.
26. Schultz MJ, Rijneveld AW, Florquin S, Edwards CK, Dinarello CA, et al. (2002) Role of interleukin-1 in the pulmonary immune response during Pseudomonas aeruginosa pneumonia. Am J Physiol Lung Cell Mol Physiol 282: L285–290.
27. Nathan C, Ding A (2010) Nonresolving inflammation. Cell 140: 871–882.
28. Burtnick MN, Brett PJ, Nair V, Warawa JM, Woods DE, et al. (2008) Burkholderia pseudomallei type III secretion system mutants exhibit delayed vacuolar escape phenotypes in RAW 264.7 murine macrophages. Infect Immun 76: 2991–3000.
29. Miao EA, Mao DP, Yudkovsky N, Bonneau R, Lorang CG, et al. (2010) Innate immune detection of the type III secretion apparatus through the NLRC4 inflammasome. Proc Natl Acad Sci U S A 107: 3076–3080.
30. Broz P, von Moltke J, Jones JW, Vance RE, Monack DM (2010) Differential requirement for Caspase-1 autoproteolysis in pathogen-induced cell death and cytokine processing. Cell Host Microbe 8: 471–483.
31. Ren T, Zamboni DS, Roy CR, Dietrich WF, Vance RE (2006) Flagellin-deficient Legionella mutants evade caspase-1- and Naip5-mediated macrophage immunity. PLoS Pathog 2: e18.
32. Molofsky AB, Byrne BG, Whitfield NN, Madigan CA, Fuse ET, et al. (2006) Cytosolic recognition of flagellin by mouse macrophages restricts Legionella pneumophila infection. J Exp Med 203: 1093–1104.
33. Lightfield KL, Persson J, Trinidad NJ, Brubaker SW, Kofoed EM, et al. (2011) Differential requirements for NAIP5 in activation of the NLRC4 inflammasome. Infect Immun 79: 1606–1614.
34. Zamboni DS, Kobayashi KS, Kohlsdorf T, Ogura Y, Long EM, et al. (2006) The Birc1e cytosolic pattern-recognition receptor contributes to the detection and control of Legionella pneumophila infection. Nat Immunol 7: 318–325.
35. Warren SE, Mao DP, Rodriguez AE, Miao EA, Aderem A (2008) Multiple Nod-like receptors activate caspase 1 during Listeria monocytogenes infection. J Immunol 180: 7558–7564.
36. Broz P, Newton K, Lamkanfi M, Mariathasan S, Dixit VM, et al. (2010) Redundant roles for inflammasome receptors NLRP3 and NLRC4 in host defense against Salmonella. J Exp Med 207: 1745–1755.
37. Wiersinga WJ, Wieland CW, van der Windt GJ, de Boer A, Florquin S, et al. (2007) Endogenous interleukin-18 improves the early antimicrobial host response in severe melioidosis. Infect Immun 75: 3739–3746.
38. Dinarello CA (2009) Immunological and inflammatory functions of the interleukin-1 family. Annu Rev Immunol 27: 519–550.
39. Lemos HP, Grespan R, Vieira SM, Cunha TM, Verri WA, Jr., et al. (2009) Prostaglandin mediates IL-23/IL-17-induced neutrophil migration in inflammation by inhibiting IL-12 and IFNgamma production. Proc Natl Acad Sci U S A 106: 5954–5959.
40. Lee JK, Kim SH, Lewis EC, Azam T, Reznikov LL, et al. (2004) Differences in signaling pathways by IL-1beta and IL-18. Proc Natl Acad Sci U S A 101: 8815–8820.

41. Kaza SK, McClean S, Callaghan M (2008) IL-8 released from human lung epithelial cells induced by cystic fibrosis pathogens Burkholderia cepacia complex affects the growth and intracellular survival of bacteria. Int J Med Microbiol 301: 26–33.
42. Abraham E (2003) Neutrophils and acute lung injury. Crit Care Med 31: S195–199.
43. Zemans RL, Colgan SP, Downey GP (2009) Transepithelial migration of neutrophils: mechanisms and implications for acute lung injury. Am J Respir Cell Mol Biol 40: 519–535.
44. Chanchamroen S, Kewcharoenwong C, Susaengrat W, Ato M, Lertmemongkolchai G (2009) Human polymorphonuclear neutrophil responses to Burkholderia pseudomallei in healthy and diabetic subjects. Infect Immun 77: 456–463.
45. Easton A, Haque A, Chu K, Lukaszewski R, Bancroft GJ (2007) A critical role for neutrophils in resistance to experimental infection with Burkholderia pseudomallei. J Infect Dis 195: 99–107.
46. Cassatella MA, Locati M, Mantovani A (2009) Never underestimate the power of a neutrophil. Immunity 31: 698–700.
47. van der Windt GJ, Wiersinga WJ, Wieland CW, Tjia IC, Day NP, et al. (2010) Osteopontin impairs host defense during established gram-negative sepsis caused by Burkholderia pseudomallei (melioidosis). PLoS Negl Trop Dis: 4 pii. pp e806.
48. Wang T, Town T, Alexopoulou L, Anderson JF, Fikrig E, et al. (2004) Toll-like receptor 3 mediates West Nile virus entry into the brain causing lethal encephalitis. Nat Med 10: 1366–1373.
49. Le Goffic R, Balloy V, Lagranderie M, Alexopoulou L, Escriou N, et al. (2006) Detrimental contribution of the Toll-like receptor (TLR)3 to influenza A virus-induced acute pneumonia. PLoS Pathog 2: e53.
50. Schultz MJ, Knapp S, Florquin S, Pater J, Takeda K, et al. (2003) Interleukin-18 impairs the pulmonary host response to Pseudomonas aeruginosa. Infect Immun 71: 1630–1634.
51. Carlsson F, Kim J, Dumitru C, Barck KH, Carano RA, et al. (2010) Host-detrimental role of Esx-1-mediated inflammasome activation in mycobacterial infection. PLoS Pathog 6: e1000895.
52. Breitbach K, Sun GW, Kohler J, Eske K, Wongprompitak P, et al. (2009) Caspase-1 mediates resistance in murine melioidosis. Infect Immun 77: 1589–1595.

OPEN ACCESS Freely available online

PLoS one

Coronavirus Papain-like Proteases Negatively Regulate Antiviral Innate Immune Response through Disruption of STING-Mediated Signaling

Li Sun[1☯], Yaling Xing[1☯], Xiaojuan Chen[1], Yang Zheng[1], Yudong Yang[1], Daniel B. Nichols[2], Mark A. Clementz[2], Bridget S. Banach[2], Kui Li[3], Susan C. Baker[2]*, Zhongbin Chen[1]*

1 Division of Infection and Immunity, Department of Electromagnetic and Laser Biology, Beijing Institute of Radiation Medicine, Beijing, China, **2** Department of Microbiology and Immunology, Loyola University of Chicago Stritch School of Medicine, Maywood, Illinois, United States of America, **3** Department of Microbiology, Immunology and Biochemistry, University of Tennessee Health Science Center, Memphis, Tennessee, United States of America

Abstract

Viruses have evolved elaborate mechanisms to evade or inactivate the complex system of sensors and signaling molecules that make up the host innate immune response. Here we show that human coronavirus (HCoV) NL63 and severe acute respiratory syndrome (SARS) CoV papain-like proteases (PLP) antagonize innate immune signaling mediated by STING (stimulator of interferon genes, also known as MITA/ERIS/MYPS). STING resides in the endoplasmic reticulum and upon activation, forms dimers which assemble with MAVS, TBK-1 and IKKε, leading to IRF-3 activation and subsequent induction of interferon (IFN). We found that expression of the membrane anchored PLP domain from human HCoV-NL63 (PLP2-TM) or SARS-CoV (PLpro-TM) inhibits STING-mediated activation of IRF-3 nuclear translocation and induction of IRF-3 dependent promoters. Both catalytically active and inactive forms of CoV PLPs co-immunoprecipitated with STING, and viral replicase proteins co-localize with STING in HCoV-NL63-infected cells. Ectopic expression of catalytically active PLP2-TM blocks STING dimer formation and negatively regulates assembly of STING-MAVS-TBK1/IKKε complexes required for activation of IRF-3. STING dimerization was also substantially reduced in cells infected with SARS-CoV. Furthermore, the level of ubiquitinated forms of STING, RIG-I, TBK1 and IRF-3 are reduced in cells expressing wild type or catalytic mutants of PLP2-TM, likely contributing to disruption of signaling required for IFN induction. These results describe a new mechanism used by CoVs in which CoV PLPs negatively regulate antiviral defenses by disrupting the STING-mediated IFN induction.

Citation: Sun L, Xing Y, Chen X, Zheng Y, Yang Y, et al. (2012) Coronavirus Papain-like Proteases Negatively Regulate Antiviral Innate Immune Response through Disruption of STING-Mediated Signaling. PLoS ONE 7(2): e30802. doi:10.1371/journal.pone.0030802

Editor: Karen L. Mossman, McMaster University, Canada

Received November 11, 2011; **Accepted** December 21, 2011; **Published** February 1, 2012

Copyright: © 2012 Sun et al. This is an open-access article distributed under the terms of the Creative Commons Attribution License, which permits unrestricted use, distribution, and reproduction in any medium, provided the original author and source are credited.

Funding: National Natural Science Foundation of China (No. 30972761, No. 30870536, No. 81172799 to ZC), Beijing Natural Science Foundation (No. 7092075 to ZC) and National S&T Major Project (2008ZX10004-015 to ZC) and Chinese National High-Tech R&D Program ("863" Program) (2006AA02Z412 to ZC), and the National Institutes of Health, USA (AI060915 to SCB), and the U.S. Department of Defense (W81XWH-09-01-0391 to KL). The funders had no role in study design, data collection and analysis, decision to publish, or preparation of the manuscript.

Competing Interests: The authors have declared that no competing interests exist.

* E-mail: chenzb@bmi.ac.cn (ZC); sbaker1@lumc.edu (SCB)

☯ These authors contributed equally to this work.

Introduction

The innate immune system is the first line of defense that protects the host against viral infection. Viral infections are sensed by pattern-recognition receptors (PRRs) of the innate immune system that recognize pathogen-associated molecular patterns (PAMPs) and then trigger an antiviral response [1]. Viral nucleic acids, such as the viral genome or replicative intermediates produced during viral replication, can be recognized by toll-like receptors (TLR3/7/8/9) or the retinoid acid-inducible gene (RIG)-I-like helicase (RLH) family members RIG-I and melanoma differentiation-associated protein 5 (MDA-5) [2,3]. Viral double stranded RNA can be sensed by membrane bound TLRs or cytosolic sensors like MDA-5, whereas RIG-I detects intracellular viral RNAs bearing 5′-triphosphate ends with base-paired structures to activate antiviral signaling [4–7]. Upon engagement with viral RNA, these PRRs recruit different adaptor proteins (MAVS/IPS-1/VISA/Cardif for RIG-I, and TRIF for TLR3 and MyD88 for TLR7/8/9), and transduce signals to the downstream kinase complexes which activate IFN regulatory factor-3 (IRF-3), nuclear factor κB (NF-κB) and ATF-2/c-jun. These transcription factors coordinately regulate the expression of type I Interferons (IFN-β and -α). Type I IFNs induce the activation of STAT transcription factors that induce the expression of hundreds of IFN-stimulated genes (ISGs) which establish an antiviral state in surrounding cells, thereby limiting viral replication and spread.

Recent investigations into the induction of the type I IFN response identified a new player in the pathway, designated here as STING (stimulator of interferon genes; also called MITA, ERIS and MPYS) [8–11]. STING was identified by investigators screening cDNA libraries for genes that, when overexpressed, were sufficient to activate production of IFN. Further studies revealed that STING-knockout mice are susceptible to lethal infection with herpes simplex virus 1 and vesicular stomatitis virus, demonstrating the critical role of STING in facilitating immune

responses to viral pathogens [12]. STING, with four transmembrane domains in the N-terminal region, is detected in the endoplasmic reticulum (ER) and upon activation complexes with signaling components including TBK1, leading to phosphorylation of IRF-3 [8]. In addition, activation of STING induces its dimerization and ubiquitination, which are proposed to play important roles in the activation of IRF-3 signaling [9].

Coronaviruses (CoV) are positive strand RNA viruses that replicate in the cytoplasm of infected cells and produce a nested-set of double-stranded RNA intermediates during viral RNA synthesis [13]. Despite the generation of dsRNA intermediates, CoV infection generally does not induce high levels of IFN production [14–18]. The new-emerging and most pathogenic CoV, severe acute respiratory syndrome coronavirus (SARS-CoV) inhibits the induction of IFN-β through blocking translocation of the transcription factor interferon regulatory factor 3 (IRF-3) from the cytoplasm to the nucleus at a later time point in infection [15]. However, activation of innate immunity in specific cell types is likely essential for generating a protective immune response. Studies using knockout mice or siRNA treatment of cell lines indicate that PRR TLR-7 in plasmacytoid dendridric cells [19]; MDA5 in brain macrophages [20], MDA5 and RIG-I in oligodendrocytes [21], and the adapter protein MyD88 are critical for activation of the innate response and protection from lethal coronavirus infection [22]. These studies are consistent with the idea that coronavirus infection induces a type I interferon response in a subset of cells and that the ability to mount an effective innate immune response is essential for clearing the viral infection and generating protective immunity. Furthermore, recent studies indicate that the inefficient activation of the innate immune response may contribute to development of more severe disease [23], [24]. At least two mechanisms have been proposed to explain the low level of type I interferon response to coronavirus infection: the sequestering of viral RNA in double membrane vesicles [25], [26] which prevents or reduces recognition by PRRs; and/or the expression of viral proteins that antagonize the innate response (reviewed in [13]). The most pathogenic CoV, severe acute respiratory syndrome coronavirus (SARS-CoV), which resulted in a 10% mortality rate, encodes at least 6 innate immune antagonists, including nonstructural protein 1 (nsp1) [27], the papain-like protease domain in nsp3 [17], nucleocapsid protein [28,30], membrane protein [29] and the products of open reading frame 6 (ORF6) and ORF3b [30]. Another important human CoV is NL63, which causes croup in children and is associated with pneumonia in the elderly [31]. HCoV-NL63 also encodes a papain-like protease, termed PLP2, which antagonizes IFN induction [14]. These coronavirus papain-like protease domains (PLPs) are contained within the nonstructural protein 3 (nsp3), which is expressed as part of a replicase polyprotein. The PLPs along with a 3C-like protease (3CLpro) cleave the replicase polyprotein to generate nonstructural proteins (nsp's) that associate with ER membranes to generate convoluted membranes and double membrane vesicles (DMVs), which are the site of viral replication [25,26]. The CoV PLPs are tethered to the DMVs by a transmembrane domain (Figure 1A). Analysis of enzymatic activity and structural studies revealed that SARS-CoV PLpro and HCoV-NL63 PLP2 function as both proteases and deubiquitinating (DUB) enzymes [14,32–35]. Initially, we speculated that CoV PLPs may act as IFN antagonists via their protease or DUB activities, however we found that both catalytic dependent and catalytic independent mechanisms contribute to PLP-mediated IFN antagonism [14,17]. Our previous studies indicated that SARS-CoV PLpro inhibits host antiviral innate immune response by inhibiting phosphorylation, dimerization and nuclear translocation of IRF-3, likely by forming a complex with IRF-3 [17]. However, the precise mechanism by which CoV PLPs inhibit IRF-3 activation is still unclear. In this work, we demonstrate that CoV PLPs antagonize IRF-3 signaling by targeting the IRF-3 scaffolding protein STING for inhibition. We also characterize both catalytic-dependent and catalytic-independent roles for PLPs in blocking the activation of IFN response.

Results

CoV PLPs antagonize STING-mediated activation of IRF-3

To determine if CoV PLPs are capable of blocking STING-mediated activation of an IRF-3 dependent promoter [36,37], we assessed the level of IFN stimulated response element reporter (ISRE-Luc) activity in the presence of STING with increasing amounts of coronavirus PLPs. Stimulation of HEK-293T cells with STING alone resulted in greater than 20-fold increase in activity of the ISRE-dependent reporter. Co-expression of STING with wild-type PLP2-TM or PLpro-TM resulted in a dose dependent decrease in ISRE activity indicating that these PLPs can antagonize STING-mediated activation of an IRF-3 dependent promoter (Fig. 1 B and C and supporting information (SI) Fig. S1). To determine if this antagonism is dependent on PLP catalytic activity, cells were co-transfected with plasmid DNA expressing STING and catalytic cysteine mutants of either PLP2-TM or PLpro-TM. Consistent with previous studies, CoV PLP catalytic mutants also act as antagonists, although they are less effective than wild-type PLPs in antagonizing the IFN response [14,17]. The effect of PLP2-TM on STING-mediated activation was also visualized using confocal microscopy. HEK-293T cells were transfected with STING-HA in the absence or presence of PLP2-TM and the localization of IRF-3 was monitored by immunofluorescence assay. In cells expressing STING-HA, IRF-3 translocates to the nucleus. However, in cells co-expressing PLP2-TM, IRF-3 remains in the cytoplasm (Fig. 1D). In addition, STING-HA and PLP2-TM co-localize in the cytoplasm of transfected cells. These results indicate that CoV PLPs antagonize STING-mediated activation of IRF-3.

CoV PLPs associate with STING

One possible mechanism for HCoV PLPs antagonism of STING-mediated activation of IFN is to associate with STING, either directly or as part of a multi-protein complex. Co-immunoprecipitation experiments were performed to determine if CoV PLPs associate with STING. HEK-293T cells were co-transfected with plasmid DNA expressing an epitope tagged version of STING (STING-Flag) in the presence or absence of PLP2-TM and cell lysates were subjected to immunoprecipitation with anti-Flag antibody. The products of the immunoprecipitation were separated by SDS-PAGE and visualized by immunoblotting (Fig. 2A). The results show that both NL63 wild-type and catalytic mutant PLPs are detected in association with STING. Similar co-immunoprecipitation results were obtained using PLpro-TM (Fig. S2) Next, we wanted to determine if STING is sequestered in HCoV-NL63-infected cells. HEK293-ACE2 cells, which express angiotensin-converting enzyme 2 (ACE2), a key receptor for SARS and NL63 coronaviruses, were transfected with STING-V5, infected with HCoV-NL63 and analyzed by confocal microscopy at 24 hrs postinfection. HCoV-NL63 replicase protein nsp3 which contains the PLP2-TM region is detected as punctate, perinuclear staining in virus-infected cells [35,38]. Interestingly, we detected partial co-localization of STING and nsp3 in virus-infected cells suggesting that STING may be sequestered in the viral replication

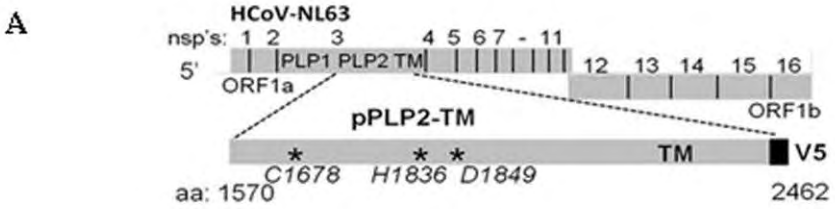
A
HCoV-NL63
nsp's: 1 2 3 4 5 6 7 - 11 12 13 14 15 16
5'
PLP1 PLP2 TM
ORF1a
ORF1b
pPLP2-TM
TM
V5
C1678 H1836 D1849
aa: 1570
2462

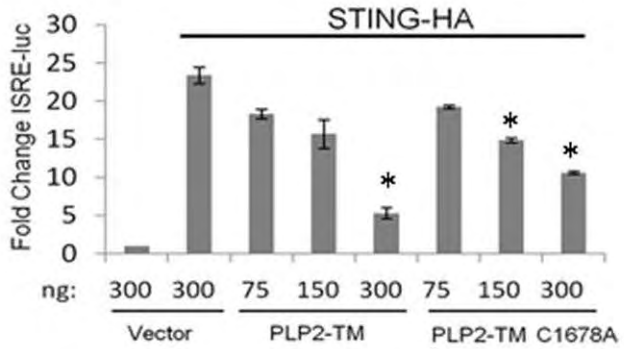
B
STING-HA
Fold Change ISRE-luc
30
25
20
15
10
5
0
ng: 300 300 75 150 300 75 150 300
Vector
PLP2-TM
PLP2-TM C1678A

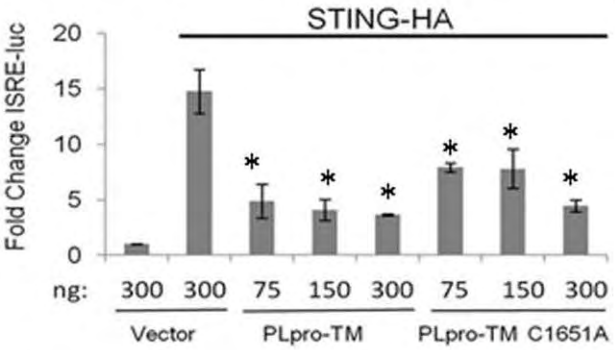
C
STING-HA
Fold Change ISRE-luc
20
15
10
5
0
ng: 300 300 75 150 300 75 150 300
Vector
PLpro-TM
PLpro-TM C1651A

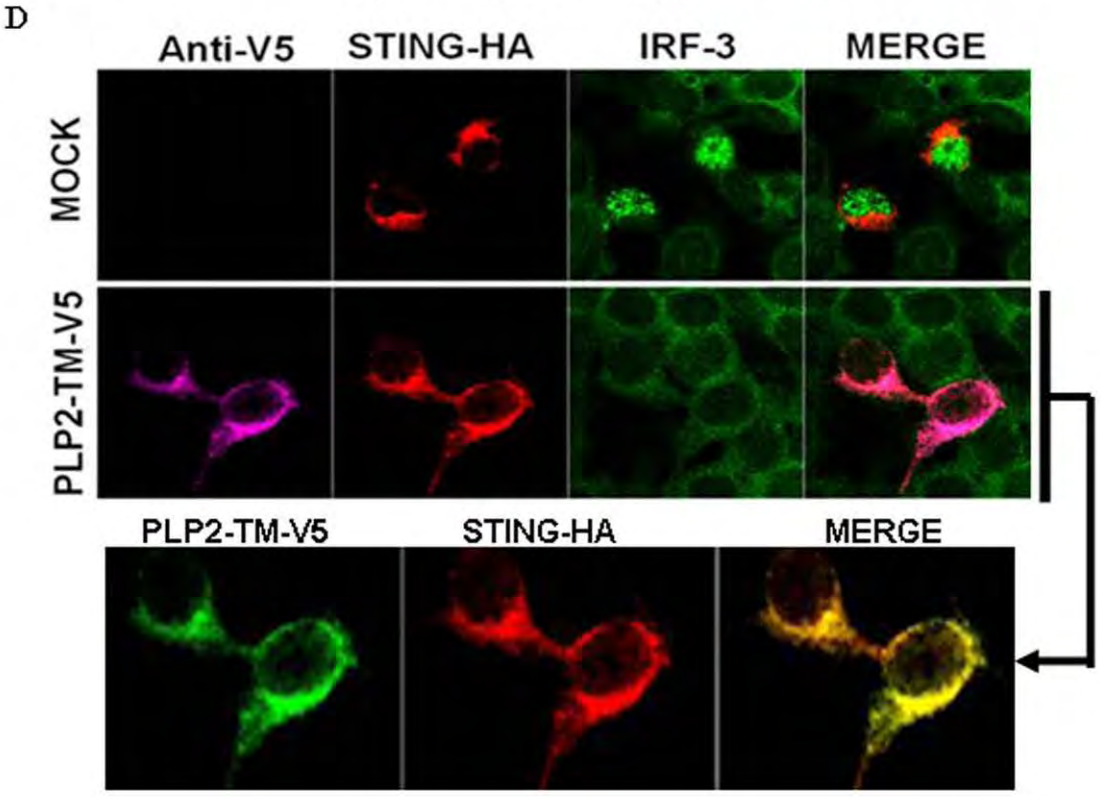
D
Anti-V5
STING-HA
IRF-3
MERGE
MOCK
PLP2-TM-V5
PLP2-TM-V5
STING-HA
MERGE

Figure 1. Expression of coronavirus PLPs blocks STING-mediated activation of the interferon stimulated response element (ISRE). (**A**) Schematic diagram of human coronaviruses (HCoV) NL63 illustrating the processing of replicase polyproteins to generate nonstructural proteins (nsp's). The papain-like protease domains, the catalytic residues that essential for protease catalytic activity [35], and the transmembrane (TM) domain within nsp3 are indicated. (**B** and **C**) HEK293T cells were transfected with the STING-HA, ISRE-luc reporter and either wild-type or catalytic mutants of HCoV-NL63 PLP2-TM or SARS-CoV PLpro-TM. Asterisks indicate statistical significance ($P<0.05$) in comparison with ISRE-reporter activity stimulated with STING. (**D**) Immunofluorescence microscopy of HEK-293T cells expressing STING-HA and PLP2-TM-V5. Cells were fixed at 24 hrs post-transfection and the localization of endogenous IRF-3 (anti-IRF-3, green) and the epitope-tagged products was visualized by confocal microscopy.
doi:10.1371/journal.pone.0030802.g001

complex and unable to mediate signaling (Fig. 2B). These results indicate that these CoV PLPs associate with STING either directly or as part of a multi-protein complex.

STING dimerization is reduced in the presence of CoV PLPs

Recent studies indicate that activation of the innate immune response signaling pathway induces dimerization and phosphorylation of STING, which are required for activation of the IFN response [9]. STING dimers can be visualized as a band at 80 kDa when resolved on SDS-PAGE [9]. We hypothesize that PLPs inhibit STING-mediated signaling through the disruption of assembly or stability of STING dimers. To test this hypothesis, cells were co-transfected with plasmid DNA expressing STING-Flag in the presence or absence of PLP2-TM and Sendai virus (SeV), and cell lysates were evaluated for STING dimers by immunoblotting with anti-Flag (Figure 3A). We detected STING dimers in STING-transfected and SeV-infected cells (Fig. 3A, lanes 2 and 4). In contrast, STING dimers were reduced in cells co-expressing PLP2-TM (Fig. 3A, lanes 3 and 5). Similar results were obtained when we evaluated PLpro-TM for disruption of STING dimers (Fig. S3), indicating that these CoV PLPs either prevent assembly or promote dissociation of STING dimers. A similar reduction in STING dimers was seen in cells transfected with STING-HA and infected with SARS-CoV (Fig. 3B, lane 2). In contract, STING dimers were not reduced when infected with SeV (Fig. 3B, lane 3). Collectively, these results indicate that STING dimerization was reduced in the presence of CoV PLPs, and was also substantially reduced in cells infected with SARS-CoV.

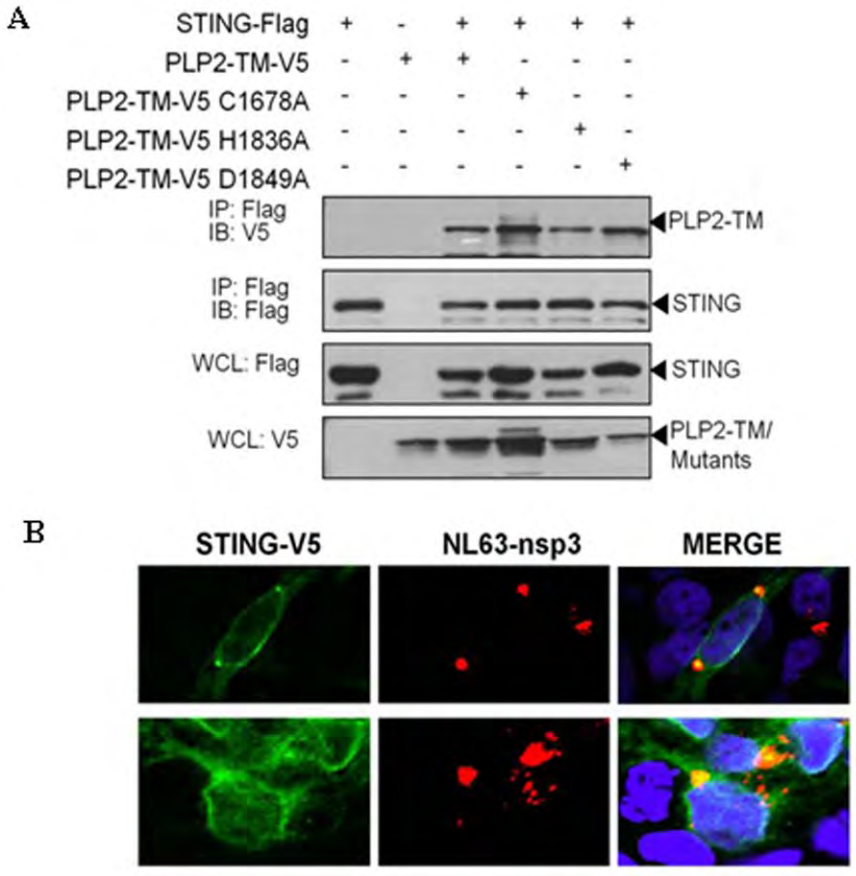

Figure 2. Coronavirus NL63 PLP2-TM associates with STING and nsp3 co-localizes with STING in virus-infected cells. (**A**) HEK293T cells were cotransfected with plasmid DNAs expressing STING-Flag and either wild type or catalytic mutants of NL63-PLP2-TM-V5. Cell lysates were prepared at 28 hrs post-transfection and subjected to immunoprecipitation (IP) with anti-Flag antibody. The products of the immunoprecipitation were separated by SDS-PAGE and subjected to immunoblotting (IB). STING-Flag, PLP2-TM-V5 and the catalytic mutant expression were selectively detected from whole cell lysates (WCL) using anti-Flag and anti-V5 antibodies. (**B**) HEK293-ACE2 cells were transfected with STING-V5 for 4 hours and then infected with HCoV-NL63 for 24 hrs and evaluated for expression of and localization of replicase product nsp3 (anti-nsp3, red) and STING-V5 (anti-V5, green).
doi:10.1371/journal.pone.0030802.g002

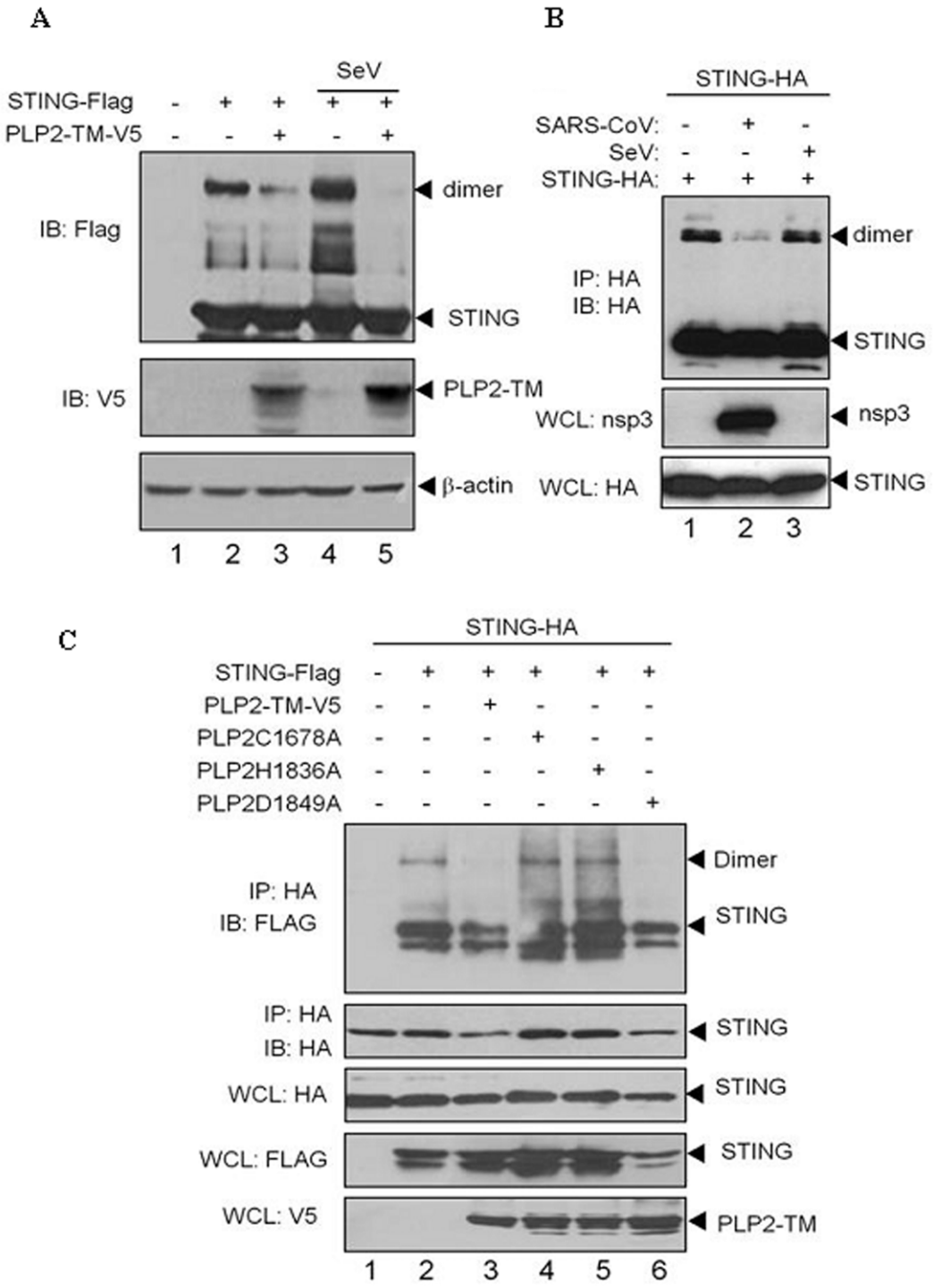

Figure 3. NL63 PLP2-TM interacts with STING and disrupts STING dimers. (**A**) HEK293T cells were co-transfected with plasmid DNA expressing STING-Flag, and/or PLP2-TM and/or infected with Sendai virus (SeV) as indicated above. The cell lysates were separated by SDS-PAGE and subjected to immunoblotting with antibodies as indicated on the left. (**B**) HEK293-ACE2 cells were transfected with plasmid DNA expressing STING-HA and infected with SARS-CoV as indicated and cell lysates were subjected to immunoprecipitation with anti-HA. The immunoprecipitated products were analyzed by SDS-PAGE and immunoblotted to access STING monomers and dimers. Whole cell lysates were immunoblotted to detected SARS-CoV replicase protein nsp3 and STING-HA. (**C**) Cells were co-transfected with STING-HA and STING-Flag with either wild-type or the indicated catalytic mutant of PLP2-TM and lysates were immunoprecipitated (IP) and immunoblotted (IB) to detect expression of each product.
doi:10.1371/journal.pone.0030802.g003

To determine if PLP catalytic activity is important for disruption of STING dimers, cells were co-transfected with plasmid DNA expressing STING-HA and STING-Flag and plasmid DNA expressing wt or catalytic mutants of PLP2-TM. Disruption of dimers was assessed by immunoprecipitation and immunoblotting (Fig. 3C). If STING-HA and STING-Flag form heterodimers,

then immunoprecipitation with anti-HA and immunoblotting with anti-Flag will allow detection of these heterodimers, as shown in Fig. 3C, lane 2. A reduction in STING dimers was detected in cells expressing wt PLP2-TM and the D1849A mutant which retains DUB activity (lanes 3 and 6), but not in cells expressing the C1678A or H1836A mutants which do not possess DUB activity [33]. These results indicate that PLP2 DUB activity is important for disruption of STING dimers. Similar results were obtained when we evaluated PLpro-TM for disruption of STING dimers (Fig. S3) A previous report indicates that only the dimer form of STING is ubiquitinated [9], which coupled with our observation that PLPs with DUB activity reduce the accumulation of STING dimers, supports a role for DUB activity in negatively regulating STING. Thus, these results are consistent with a role for viral DUB activity in antagonizing either the assembly or stability of STING dimers.

PLP2-TM disrupts MAVS-STING-IKKε interaction

Next, we wanted to determine if PLP2-TM altered the assembly of complexes required for activation of IRF-3 and the IFN response. MAVS, a mitochondrial-associated adaptor protein is a critical player in viral activation of the IFN response. Activation of MAVS mediates the assembly of a multi-protein complex that activates TBK-1/IKKε to phosphorylate IRF-3 [39]. Recent studies revealed that STING associates with MAVS to recruit TBK-1/IKKε and IRF-3 to a complex [8], and that activation of STING is critical for activation of IRF-3 [11,12]. Therefore, we investigated if PLP2-TM had any effect on assembly of these signaling complexes. HEK-293T cells were co-transfected with plasmid DNAs expressing STING-HA along with Flag-RIG-I, Flag-MAVS or Flag-IKKε in the presence or absence of PLP2-TM. Cell lysates were harvested and evaluated for co-immunoprecipitation of complexes by immunoblotting. We found that expression of PLP2-TM had no effect on co-immunoprecipitation of RIG-I with STING (Fig. 4A), but that co-immunoprecipitation of MAVS and IKKε was disrupted by expression of PLP2-TM (Fig. 4B, lane 4 and Fig. 4C, lane 4). Overall, these results are consistent with an important role for CoV PLPs in blocking activation of IFN by disrupting STING-mediated activation and complex formation.

PLP2-TM blocks ubiquitination of signaling molecules

Modification of signaling molecules by ubiquitination plays a critical role in activation of the IFN response [40–42]. Here, we asked if PLP2-TM can recognize and deubiquitinate key complexes in the IFN signaling pathway. HEK-293T cells were transfected with HA-Ub and epitope-tagged versions of either RIG-I, TBK-1, IRF-3 or STING and cell lysates were subjected to immunoprecipitation and immunoblotting to determine the ubiquitination status of the immunoprecipitated proteins (Fig. 5). We found that there was a dramatic reduction in the amount of ubiquitinated RIG-I (A), TBK-1 (B), IRF-3 (C) and STING (D) in cells expressing PLP2-TM. We also investigated the role of the PLP2-TM catalytic activity in mediating deubiquitination. Cells were transfected with HA-Ub and either wild-type or catalytic mutants of PLP2-TM and as expected, we detected a reduction in the level of ubiquitinated STING in the presence of wt and the D1849A mutant of PLP2-TM (Fig. 5D, lanes 4 and 7). Interestingly, expression of the PLP2-TM C1678A and H1836A mutants, which are catalytically inactive [35], still resulted in reduced levels of ubiquitined STING compared to the control (Fig. 5D, lanes 5 and 6). These results suggest that the catalytically inactive mutants of PLP2-TM may block access of STING to the ubiquitination machinery, thereby resulting in reduced levels of

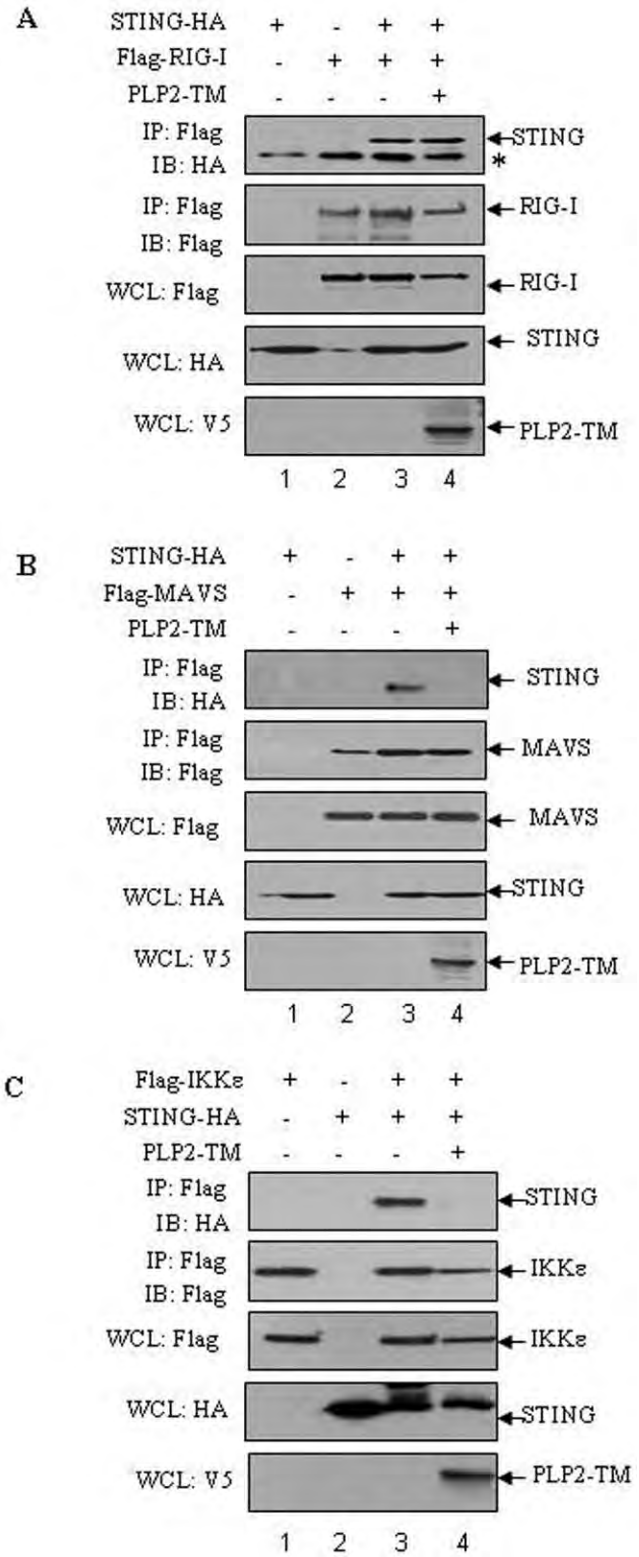

Figure 4. NL63 PLP2-TM disrupts signaling complex formation. HEK293T cells were co-transfected with STING-HA together with either Flag-tagged RIG-I (**A**), Flag-tagged MAVS (**B**) or Flag-tagged IKKε (**C**), and PLP2-TM-V5. At 28 h after transfection, cell lysates were prepared and subjected to immunoprecipitate (IP) and immunoblot (IB) with the indicated antibodies. The asterisk indicates the nonspecific band.
doi:10.1371/journal.pone.0030802.g004

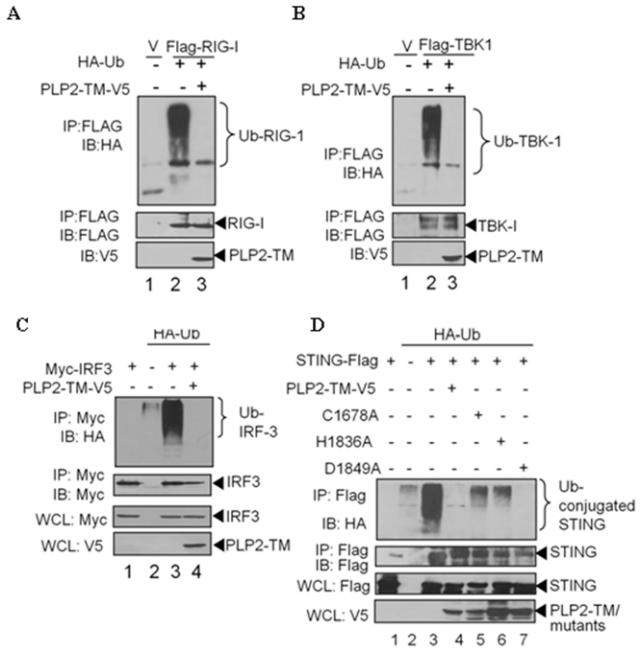

Figure 5. Reduction of ubiquitinated forms of RIG-I, STING, TBK1 and IRF-3 in the presence of NL63 PLP2-TM. HEK293 cells were transfected with Flag-tagged RIG-I(**A**), TBK1(**B**), myc-IRF-3(**C**), or STING-Flag (**D**) together with plasmid DNA expressing HA-tagged Ub in the presence or absence of V5-tagged PLP2-TM-V5. Cells were incubated for 24 hours after transfection and treated with 25 μM MG132 for 4 hours prior to harvesting lysates. Lysates were immunoprecipitated with the indicated antibody and the products were subjected to immunoblotting with anti-HA to evaluate ubiquitinated proteins (upper panels). The whole cell lysates (WCL) were blotted to evaluate expression of each epitope-tagged product (bottom panels).
doi:10.1371/journal.pone.0030802.g005

Ub-conjugated STING. Thus, the IFN antagonism of the catalytic mutants may be due to physical interaction with STING which blocks access of ubiquitin chains or Ub-ligases or other modifying enzymes that are required for efficient signaling [43,44]. A previous report indicates that only the dimer form of STING is ubiquitinated [9], which coupled with our observation that PLPs with DUB activity reduce the accumulation of STING dimers, supports a role for DUB activity in negatively regulating STING. Thus, these results are consistent with a role for viral DUB activity in antagonizing either the assembly or stability of STING dimers.

Discussion

In this study, we investigated the mechanisms of the IFN antagonism imposed by the coronavirus papain-like proteases (CoV PLPs). Previous studies suggested that CoV PLPs block IFN synthesis by inhibiting virus-activated IRF-3 phosphorylation and nuclear translocation, but the underlying mechanism was unclear [14,17,32]. Here we show that both SARS-CoV PLpro-TM and HCoV-NL63 PLP2-TM associate with an ER-associated protein, STING and block assembly or stability of STING dimers which are important for downstream signaling and induction of the IFN response. Importantly, we have demonstrated that STING colocalizes with nsp3 (which contains PLPs) in HCoV-NL63 infected cells, and that STING dimerization was substantially reduced in cells infected with SARS-CoV. In addition, we found that ubiquitination of signaling molecules is dramatically reduced in the presence of HCoV-NL63 PLP2-TM, which may contribute to destabilizing the signaling complex. Targeting of the signaling complex by blocking ubiquitination and disruption of STING dimers presents yet another mechanism used by coronaviruses to prevent activation of innate immunity and illustrates how coronavirus PLPs negatively regulate the IFN antiviral immune response in host cells.

Targeting the stimulator of IFN genes, STING

Recent studies have revealed the arsenal of proteins that viruses use to evade and subvert recognition by pattern-recognition receptors (PRRs) or activation of signaling molecules that are designed to respond to infectious agents [45]. STING is a key scaffolding protein that links the cytosolic viral RNA sensors RIG-I, rather than the MDA5, to the mitochondria protein MAVS [8,11]. These cytosolic sensors have been shown to be important for recognition of coronavirus RNA in oligodendrocytes [21] and brain macrophages/microglia [20]. Activation of STING, either by expression of N-RIG, the constitutive active caspase recruitment domain of RIG-I or ectopic expression of STING itself, induces the formation of STING dimers, which are modified by phosphorylation and ubiquitylation [9]. The activation of STING facilitates the recruitment of IRF-3 and TBK-1 into a complex where IRF-3 is phosphorylated. Phosphorylated IRF-3 forms dimers and is transported to the nucleus to activate transcription of type I IFN genes. CoV PLPs target STING and prevent this key scaffolding protein from activating IRF-3. Previously, we showed that PLpro blocks NF-κB-dependent promoter activity and that antagonism is abrogated using protease inhibitors [14]. Thus, CoV PLPs interact with key signaling molecules and exploit both catalytic dependent and catalytic-independent mechanisms to block the innate immune response. CoV-PLPs disrupt signal transduction to both IRF-3 and NF-κB, the key transcription factors required for activation of IFN-β (Fig. 6). Interestingly, CoV PLPs seem to exploit both catalytic dependent and independent mechanisms to block STING activity and a catalytic-dependent mechanism to disrupt NF-κB activity.

Previous studies have shown a role for viral proteases in cleavage of key IFN signaling molecules [45]. For example, the NS3/4A protease of hepatitis C virus and GB virus B and the 3ABC precursor of hepatitis A virus cleave MAVS/IPS-1, the mitochondria-associated signaling molecule, which blocks activation of IFN synthesis [46–51]. Therefore, it seemed reasonable to hypothesize that CoV PLPs exploited their protease or DUB activity to antagonize the innate immune response. However, we had previously shown that catalytically defective PLP mutants were still capable of inhibiting IRF-3 activation [17]. Furthermore, addition of a protease inhibitor that blocks both protease and DUB activity [52] failed to abrogate the PLP inhibition on activation of IRF-3 dependent promoters [14]. This led us to suspect that CoV PLPs were interacting with a component in the IFN signaling pathway. The fact that CoV PLPs are expressed as a polyprotein that localizes to the ER [25,26] led us to evaluate ER resident signaling molecules as targets of antagonism. The results presented in this study indicate that CoV PLPs are particularly potent antagonists because they can block: 1) STING dimerization; 2) the MAVS-STING-IKKε interaction required for signaling and 3) the ubiquitination of key signaling molecules such as RIG-I, STING, IRF-3 and TBK-1. Interestingly, catalytically inactive mutants of PLPs can interact, either directly or as part of a signaling complex, with STING and moderately inhibit IRF-3 activation for IFN induction, but wild type PLPs exhibit the most robust inhibition. We found that catalytic activity was important for blocking either the assembly or the stability of STING dimers. In addition, we found that PLP2-TM either

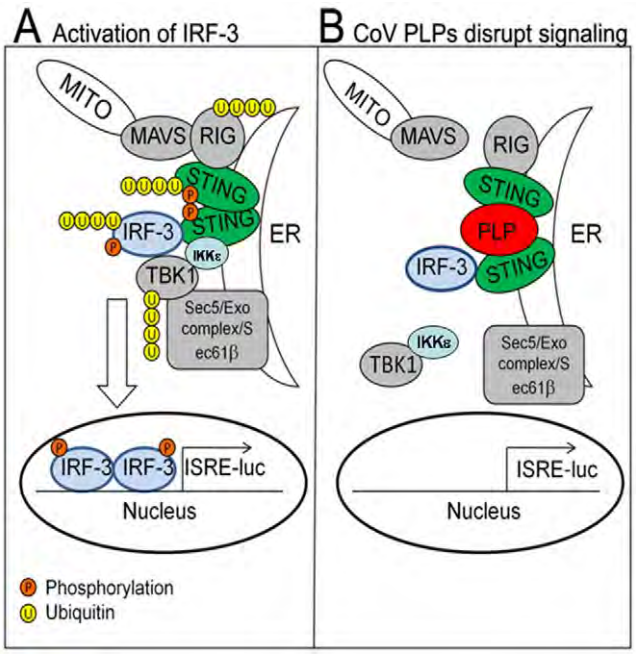

Figure 6. Model depicting the mechanisms used by CoV PLPs to block STING from signaling the activation of the IFN-β induction pathway. (**A**) Activation of sensors such as RIG-I induces interaction with the signaling complex including MAVS, STING, IRF-3 and TBK-1. Activated MAVS interacts with STING, which dimerizes, leading to the activation of IKK complex, TBK1 and IKKε [8]. The activation of this complex leads to the ubiquitination of RIG-I, STING, IRF-3 and TBK1 and the phosphorylatin of STING and IRF-3. Activated the transcription factor IRF-3 translocates to the nucleus inducing production of IFN. (**B**) Coronavirus papain-like protease domains (depicted here as PLP) interact with STING to block signaling by blocking assembly or stability of STING dimers and preventing the ubiquitination of signaling proteins, such as RIG-I, TBK1, and IRF-3.
doi:10.1371/journal.pone.0030802.g006

actively deubiquitinates or blocks the ubiquitination of the signaling molecules. This is consistent with these reported works that STING dimers were modified by ubiquitin [9]. By associating with STING, either directly or as part of a signaling complex, CoV PLPs can target and either block or deubiquitinate this important signaling molecule. Of course the question still remains if the PLP-STING interaction is direct or indirect, and what region(s) of the PLP are required for this potential interaction. These studies are currently ongoing. Understanding how to negatively regulate STING-mediated innate antiviral signaling by CoV PLPs may lead to the development of novel antiviral therapies and new insights for regulating the IFN response during acute and chronic infections.

DUBs as negative regulators of IFN activation

One of the striking findings in this report is the similarity in the function of CoV PLPs and cellular DUBs such as the NF-κB responsive gene A20, deubiquitinating enzyme A (DUBA), and the tumor suppressor protein associated with cylindromatosis (CYLD) [53–55]. Like CoV PLPs, cellular DUBs were identified as negative regulators of the innate immune response. A20 is considered a "central gatekeeper in inflammation and immunity" [56] because of its ability to interact with and mediate ubiquitin-editing on signaling molecules such as RIP1, TRAF6, RIP2 and NEMO. A20 DUB activity removes K-63 linked polyubiquitin chains from RIP1, TRAF6, RIP2 and NEMO which results in negative regulation of the innate immune response. In addition, A20 has been shown to act by antagonizing interactions between signaling molecules and ubiquitin conjugating enzymes [57]. Interestingly, both A20 and CoV PLPs can act on K-63 linked ubiquitin chains [14,58]. Further experiments are needed to determine if recognition, processing or sequestering of K-63 linked ubiquitin is important for CoV PLPs negative regulation of the IFN response. Cellular proteins DUBA and CYLD also negatively regulate the innate immune response. Kayagaki and co-workers found that DUBA targets and deubiquitinates TRAF3, a signaling molecule required for activation of IRF-3 [55]. They showed that reducing the expression of DUBA augments the IFN response to poly(I:C) whereas ectopic expression of DUBA blocks the IFN response. CYLD has been shown to deubiquitinate RIG-I to inhibit IFN production [53,54]. Ectopic expression of CYLD antagonizes the IFN response whereas siRNA-mediated knock-down of CYLD expression allows for a more robust IFN response. It seems that CoV PLPs are usurping the function of cellular DUBs by behaving as negative regulators of the innate immune response through targeting STING for both deubiquitination and dimer disruption.

Another possibility is that CoV PLPs function by sequestering STING as a mechanism of blocking activation of IFN. Both catalytically active and inactive CoV PLPs could interact and sequester STING and thereby prevent activation of IRF-3. Coronavirus PLPs are part of the viral replicase polyprotein that associates with ER membranes to form convoluted membranes and double membrane vesicles (DMVs) which are the sites of viral RNA synthesis [25,26,59]. Interestingly, STING also resides in the ER and upon activation assembles with Sec5 into exocyst vesicles [12]. The interaction of STING with PLP2-TM may block the signals required for STING to translocate to exocyst vesicles. Thus, further studies with CoV PLPs may reveal specific targets of STING that modulate this arm of the innate immune response.

In summary, the results of this study indicate that HCoV-NL63 and SARS-CoV PLPs inhibit host IFN-β production by targeting and nullifying STING. Blocking this key scaffolding protein prevents activation of IRF-3 and subsequent transcription of IFN-β. The antagonism functions of CoV PLPs are important negative regulators of the innate immune response and may be important in the virulence and pathogenesis of human coronavirus infection. Further characterization of the PLP-STING interaction may provide new targets for antiviral interventions.

Materials and Methods

Cells and virus

HEK293T cells [44] were cultured using Dulbecco's modified Eagle's medium containing 10% (v/v) fetal calf serum, supplemented with penicillin (100 U/ml) and streptomycin (100 μg/ml). HEK293-ACE2 cells, which express angiotensin-converting enzyme 2 (ACE2), a key receptor for SARS and NL63 coronaviruses, were kindly provided by Dr. Kui Li (University of Tennessee Health Science Center, Memphis, USA) and cultured as above with the addition of puromycin (10 μg/ml). HCoV-NL63 was propagated in LLC-MK2 cells [35] which were kindly provided by Lia van der Hoek (University of Amsterdam, The Netherlands) and as previously described [35]. SARS-CoV was propagated in VeroE6 cells as previously described [52]. All work with SARS-CoV was performed in a biosafety level 3 facility using approved protocols. Sendai virus was kindly provided to the Chen lab by Dr. Shaobo Xiao (Huazhong Agricultural University, Wuhan, China) or purchased from Charles River Laboratories.

Plasmid DNAs

DNA constructs containing wild type and catalytic mutants of NL63 PLP2-TM SARS-CoV PLpro-TM and plasmids of IFN-β-Luc, PRD(III-I)4-Luc, ISRE-Luc and HA-tagged Ub were previously described [14,17]. Flag-hIPS-1(MAVS), BOS-Myc-hIRF3, Flag-hTBK1, Flag-hRIG-I were kindly provided by Dr. Himanshu Kuma and Shizuo Akira (Immunology Frontier Research Center Osaka University, Osaka, Japan). pcDNA3.1-HA-ERIS (designated here as STING-HA) and pCMV14-Flag-ERIS (designated STING-Flag) were kindly provided by Dr. Zhengfan Jiang (School of Life Sciences, Peking University, Beijing, China).

Luciferase reporter gene assay

HEK293T cells were transfected with the indicated stimulator plasmid DNA (STING-HA), reporter plasmid DNA [pRL-TK, ISRE-Luc, IFN-β-Luc, or PRD(III-I)4-Luc] and either NL63 PLP2-TM or SARS-CoV PLpro-TM using either Lipofectamine 2000 or Mirus LT1 according to the manufacturer's protocol and incubated for 24 hours. Firefly luciferase and *Renilla* luciferase activities were assayed using the Dual Luciferase Reporter Assay Kit (Promega). Data were shown as mean relative luciferase (firefly luciferase activity divided by Renilla luciferase activity) with standard deviation from a representative experiment carried out in triplicate. For statistical analysis, the data between Vector (300 ng) and PLP (PLpro)-TM with various concentrations were subjected to unpaired, two-tailed Student's t test using the Microsoft SPSS 12.0 software, and P values of <0.05 were considered to indicate statistical significance.

Immunofluorescence assays

HEK293 or HEK293-ACE2 cells were plated on fibronectin treated glass coverslips in 12-well plates. To evaluate localization of STING and NL63 PLP2-TM, plasmid DNA expressing STING-HA (225 ng per well) was transfected in the presence or absence of 300 ng of PLP2-TM using Mirus LT1 according to the manufacturer's protocol. At 16 hours post transfection, cells were fixed with 3.7% formaldehyde for 10 min at room temperature. Cells were then incubated with 1:200 dilution of rabbit anti-IRF-3 (Active Motif), mouse anti-HA (Covance), and goat anti-V5 (Genscript) in ADPS (PBS+0.1% Triton-×100+5% fetal calf serum) for 1 hour at room temperature. Cells were washed three times with PBS and incubated with 1:200 dilution of chicken anti-rabbit Alexa Fluor (AF) 488, donkey anti-mouse AF568, and donkey anti-goat AF647 (Molecular Probes) in ADPS for 1 hour in the dark. Following the incubation, cells were washed three times with PBS, mounted, and imaged with the Zeiss LSM-510 confocal microscope.

To evaluate STING localization in NL63 infected cells, HEK293-ACE2 cells were transfected with 100 ng of a plasmid expressing human STING-V5 for 4 hours. Cells were subsequently infected with 200 µl of HCoV-NL63 (1×10^4 pfu/ml). At 24 hours post infection, cells were fixed with 3.7% formaldehyde for 10 minutes at room temperature. Cells were then diluted with a 1:1000 dilution of rabbit anti-nsp3 [35] and 1:1000 dilution of mouse anti-V5 for 1 hour at room temperature in ADPS. Cells were washed three times with PBS and incubated with a 1:200 dilution of goat anti-rabbit AF568 and chicken anti-mouse AF488, and 1:1000 dilution of DAPI for 30 minutes at room temperature in the dark. The cells were then washed three times with PBS, mounted, and imaged with the Zeiss LSM-510 confocal microscope.

Co-immunoprecipitation (Co-IP) analysis

HEK293T cells were seeded on 100-mm dishes at a density of 1×10^6 cells/dish. 12 hours later, cells were transiently transfected with a total of 10 µg of empty plasmid or indicated expression plasmids using Lipofectamine 2000 (Invitrogen). At 28 hours after transfection, cells were lysed in buffer containing 0.5% Triton-X-100, 150 mM NaCl, 12.5 mM β-glycerolphosphate, 1.5 mM MgCl2, 2 mM EGTA, 10 mM NaF, 1 mM Na_3VO_4, 2 mM DTT plus protease inhibitor cocktail (Sigma). The cell extracts were spun down at 5000× g for 10 minutes at 4°C. The protein concentration of each lysate was determined using the BCA Protein Assay (Bio-Rad) and the concentration was adjusted to 1 µg/µl, with 500 µl of lysate used for each IP. The lysates were precleared by adding 20 µl protein A+G Agarose (Beyotime Institute of Biotechnology, China) and 1 µg of normal IgG and incubating for 2 hours at 4°C, followed by spinning down the beads. The precleared supernatant was incubated with the designated antibody [Anti-Flag (Sigma) or anti-HA (MBL)/anti-Myc (MBL)] with rocking overnight at 4°C. The beads-antibody-antigen complex was spun down and washed 3 times with 1 ml of lysis buffer. The proteins were eluted from the beads in 30 µl of 2× SDS-PAGE sample buffer subjected to boiling for 10 min. The sample was separated by SDS-PAGE and transferred to PVDF membrane for western blotting.

Assessing ubiquitination of signaling molecules in cultured cells

The effect of HCoV-NL63 PLP2-TM on ubiquitinated proteins in cultured cells was assessed as described previously [53,55]. Briefly, Flag-tagged RIG-I, TBK1, STING, IRF-3 were co-transfected into HEK293T cells together with pcDNA3.1-HA-Ub, plus wild type or catalytic mutant PLP2-TM DNA using Lipofectamine 2000 according to the manufacturer's instructions. Empty vector pcDNA3.1/V5-HisB was used to standardize the total amount of DNA used for transfection. 24 post-transfection, cells were incubated with 25 µM MG132 for 4 hours, and then lysed in 300 µl of RIPA buffer (50 mM Tris-HCl pH 7.4, 150 mM NaCl, 2 mM EDTA, 1% NP-40, 0.1% SDS) containing protease inhibitor cocktail (1 mM, Roche) and 10 µM NEM, Non-covalently bound proteins were dissociated by boiling in 1% SDS, and samples diluted 1:10 in lysis buffer (50 mM Tris-HCl pH 7.4, 150 mM NaCl, 2 mM EDTA, 1% NP-40) containing protease inhibitor cocktail and 10 µM NEM. The soluble lysates were then immunoprecipitated with anti-Flag antibody followed by washing with RIPA buffer for three times. Flag-tagged proteins were resolved by SDS-PAGE and sequentially blotted with anti-HA and anti-Flag antibodies. 150 µl of lysate was used for each immunoprecipitation reaction. To confirm the PLP and the catalytic mutant expression level, western blotting with anti-V5 antibody (Invitrogen) was used to detect wild type and catalytic mutant PLP2-TM-V5 protein expression.

Detection of STING dimers

To assess STING dimers, HEK293T cells were transfected with STING-HA or STING-Flag (0.5 µg per 100 mm dish) and lysates subjected to immunoprecipitation and western blotting as described [9] with the indicated antibodies. To detect STING dimers induced by Sendai Virus (SeV) infection, HEK293T cells were transfected with STING-Flag and then infected with SeV (HAU = 100). 24 hours later, cells were lysed and immunoblotted with anti-Flag antibodies. To assess STING dimers in transfected and SARS-CoV- or Sendai Virus (SeV)- infected cells, HEK293-ACE2 cells were seeded at 10^5 cells/well in twelve well plates. 24 hours later, cells were transfected with either 0.5 µg of mSTING-HA expressing plasmid DNA or 0.5 µg pcDNA3.1V5-HisB vector DNA (Invitrogen). Following six hours of incubation, the cells were infected with either SARS-CoV Urbani (MOI = 0.1)

or SeV (HAU = 100). 24 hours later, the cells were lysed in 300 µl of lysis buffer containing 0.5% Triton-X-100, 150 mM NaCl, 12.5 mM β-glycerolphosphate, 1.5 mM MgCl2, 2 mM EGTA, 10 mM NaF, 1 mM Na_3VO_4, 2 mM DTT plus protease inhibitor cocktail (Sigma). 150 µl of lysate was used for each immunoprecipitation reaction. After preclearing the lysate with protein G magnetic beads (Millipore), 0.5 µg of rabbit anti-HA antibodies (Invitrogen) was incubated with the lysate overnight at 4°C. 25 µl protein G magnetic beads was added to the immunoprecipitation reactions and incubated for 2 hours at 4°C. Protein G magnetic beads were precipitated and washed 3 times with 1 ml lysis buffer. 80 µl of 2× sample buffer containing 10% glycerol, 5% -mercaptoethanol, 3% SDS, 12.5% upper buffer (0.5 M Trizma base and 0.4% SDS), and 0.01 mg bromophenol blue was added to the beads, and protein-antibody complexes were eluted by incubating at 37°C for 30 min. Samples were separated on SDS-PAGE gel and transferred to a PVDF membrane. Blots were incubated with mouse anti-HA antibody (Sigma) or anti-nsp3 antisera [17] at 0.5 µg/µl and 0.125 µg/µl concentrations, respectively. After washing three times in TBS-T buffer, blots were subsequently incubated with either goat-anti-mouse-HRP or donkey-anti-rabbit-HRP (Southern Biotech). Antibody-antigen reactions were detected using the Western Lighting Plus-ECL chemiluminescence reagents from Perkin Elmer.

Supporting Information

Figure S1 (**A**) Schematic diagram of SARS-CoV illustrating the processing of replicase polyproteins to generate nonstructural proteins (nsp's). The papain-like protease domains, the catalytic residues, and the transmembrane (TM) domain within nsp3 are indicated. (**B**) Western blot detection of STING-V5 and dose response of PLP2-TM-V5 and PLpro-TM-V5.
(TIF)

Figure S2 SARS-CoV PLpro-TM associates with STING. HEK293T cells were cotransfected with plasmid DNAs expressing STING-Flag and either wild type or catalytic mutants of PLpro-TM-V5. Cell lysates were prepared at 28 hrs post-transfection and subjected to immunoprecipitation (IP) with anti-Flag antibody. The products of the immunoprecipitation were separated by SDS-PAGE and subjected to immunoblotting (IB). STING-Flag, PLpro-TM-V5 and the catalytic mutant expression were selectively detected from whole cell lysates (WCL) using anti-Flag and anti-V5 antibodies.
(TIF)

Figure S3 SARS-CoV PLpro-TM interacts with STING and disrupts STING dimers. HEK293T cells were co-transfected with plasmid DNAs expressing STING-HA, and/or PLpro-TM and/or GFP-V5 as indicated above. At 24 hrs post-transfection, cell lysates were subjected to immunoprecipitation with the indicated antibody and the products were separated by SDS-PAGE and subjected to immunoblotting to detect STING monomer and dimer (upper panel). Whole cell lysates (WCL) were immunoblotted to detected expression of STING-HA, PLpro-TM-V5, and GFP-V5 (lower panel).
(TIF)

Acknowledgments

We would like to thank Dr. Himanshu Kuma, Dr. Shizuo Akira, Dr. Zhengfan Jiang, Dr. Min-Jung Kim, Dr. Robert M. Krug and Dr. Edward W. Harhaj for kindly providing the reporter plasmids and expression constructs. We also would like to thank Dr. Zhengfan Jiang for the helpful suggestion of STING dimer detection.

Author Contributions

Conceived and designed the experiments: ZC SCB KL. Performed the experiments: LS YX XC YZ YY DBN MAC BSB. Analyzed the data: LS YX ZC SCB. Wrote the paper: SCB ZC.

References

1. Kawai T, Akira S (2007) Antiviral signaling through pattern recognition receptors. J Biochem 141: 137–145.
2. Yoneyama M, Fujita T (2009) RNA recognition and signal transduction by RIG-I-like receptors. Immunol Rev 227: 54–65.
3. Barral PM, Sarkar D, Su ZZ, Barber GN, DeSalle R, et al. (2009) Functions of the cytoplasmic RNA sensors RIG-I and MDA-5: key regulators of innate immunity. Pharmacol Ther 124: 219–234.
4. Hornung V, Ellegast J, Kim S, Brzózka K, Jung A, et al. (2006) 5′-Triphosphate RNA is the ligand for RIG-I. Science 314: 994–997.
5. Pichlmair A, Schulz O, Tan CP, Näslund TI, Liljeström P, et al. (2006) RIG-I-mediated antiviral responses to single-stranded RNA bearing 5′-phosphates. Science 314: 997–1001.
6. Schmidt A, Schwerd T, Hamm W, Hellmuth JC, Cui S, et al. (2009) 5′-triphosphate RNA requires base-paired structures to activate antiviral signaling via RIG-I. Proc Natl Acad Sci U S A 106: 12067–12072.
7. Rehwinkel J, Tan CP, Goubau D, Schulz O, Pichlmair A, et al. (2010) RIG-I detects viral genomic RNA during negative-strand RNA virus infection. Cell 140: 397–408.
8. Zhong B, Yang Y, Li S, Wang YY, Li Y, et al. (2008) The adaptor protein MITA links virus-sensing receptors to IRF3 transcription factor activation. Immunity 29: 538–550.
9. Sun W, Li Y, Chen L, Chen H, You F, et al. (2009) ERIS, an ER IFN stimulator, activates innate immune signaling through dimerization. Proc Natl Acad Sci U S A 106: 8653–8658.
10. Jin L, Waterman PM, Jonscher KR, Short CM, Reisdorph NA, et al. (2008) MPYS, a novel membrane tetraspanner, is associated with major histocompatibility complex class II and mediates transduction of apoptotic signals. Mol Cell Biol 28: 5014–5026.
11. Ishikawa H, Barber GN (2008) STING is an endoplasmic reticulum adaptor that facilitates innate immune signalling. Nature 455: 674–678.
12. Ishikawa H, Ma Z, Barber GN (2009) STING regulates intracellular DNA-mediated, type I interferon-dependent innate immunity. Nature 461: 788–792.
13. Perlman S, Netland J (2009) Coronaviruses post-SARS: update on replication and pathogenesis. Nat Rev Microbiol 7: 439–450.
14. Clementz MA, Chen Z, Banach BS, Wang Y, Sun L, et al. (2010) Deubiquitinating and interferon antagonism activities of coronavirus papain-like proteases. J Virol 84: 4619–4629.
15. Spiegel M, Pichlmair A, Martinez-Sobrido L, Cros J, Garcia-Sastre A, et al. (2005) Inhibition of Beta interferon induction by severe acute respiratory syndrome coronavirus suggests a two-step model for activation of interferon regulatory factor 3. J Virol 79: 2079–2086.
16. Zhou H, Perlman S (2006) Mouse Hepatitis Virus Does Not Induce Beta Interferon Synthesis and Does Not Inhibit Its Induction by Double-Stranded RNA. J Virol 81: 568–574.
17. Devaraj SG, Wang N, Chen Z, Tseng M, Barretto N, et al. (2007) Regulation of IRF-3-dependent Innate Immunity by the Papain-like Protease Domain of the Severe Acute Respiratory Syndrome Coronavirus. J Biol Chem 282: 32208–32221.
18. Versteeg GA, Bredenbeek PJ, van den Worm SH, Spaan WJ (2007) Group 2 coronaviruses prevent immediate early interferon induction by protection of viral RNA from host cell recognition. Virology 361: 18–26.
19. Cervantes-Barragan L, Zust R, Weber F, Spiegel M, Lang KS, et al. (2007) Control of coronavirus infection through plasmacytoid dendritic-cell-derived type I interferon. Blood 109: 1131–1137.
20. Roth-Cross JK, Bender SJ, Weiss SR (2008) Murine coronavirus mouse hepatitis virus is recognized by MDA5 and induces type I interferon in brain macrophages/microglia. J Virol 82: 9829–9838.
21. Li J, Liu Y, Zhang X (2010) Murine coronavirus induces type I interferon in oligodendrocytes through recognition by RIG-I and MDA5. J Virol 84: 6472–6482.
22. Sheahan T, Morrison TE, Funkhouser W, Uematsu S, Akira S, et al. (2008) MyD88 is required for protection from lethal infection with a mouse-adapted SARS-CoV. PLoS Pathog 4: e1000240.
23. Zhao J, Zhao J, Perlman S (2010) T cell responses are required for protection from clinical disease and for virus clearance in severe acute respiratory syndrome coronavirus-infected mice. J Virol 84: 9318–9325.
24. Rose KM, Elliott R, Martinez-Sobrido L, Garcia-Sastre A, Weiss SR (2010) Murine coronavirus delays expression of a subset of interferon-stimulated genes. J Virol 84: 5656–5669.

25. Gosert R, Kanjanahaluethai A, Egger D, Bienz K, Baker SC (2002) RNA replication of mouse hepatitis virus takes place at double-membrane vesicles. J Virol 76: 3697–3708.
26. Knoops K, Kikkert M, Worm SH, Zeverhover-Dobbe JC, van der Meer Y, et al. (2008) SARS-coronavirus replication is supported by a reticulovesicular network of modified endoplasmic reticulum. PLoS Biol 6: e226.
27. Narayanan K, Huang C, Lokugamage K, Kamitani W, Ikegami T, et al. (2008) Severe acute respiratory syndrome coronavirus nsp1 suppresses host gene expression, including that of type I interferon, in infected cells. J Virol 82: 4471–4479.
28. Lu X, Pan J, Tao J, Guo D (2010) SARS-CoV nucleocapsid protein antagonizes IFN-β response by targeting initial step of IFN-β induction pathway, and its C-terminal region is critical for the antagonism. Virus Genes 42(1): 37–45.
29. Siu KL, Kok KH, Ng MH, Poon VK, Yuen KY, et al. (2009) Severe Acute Respiratory Syndrome Coronavirus M Protein Inhibits Type I Interferon Production by Impeding the Formation of TRAF3.TANK.TBK1/IKKε Complex. J Biol Chem 284: 16202–16209.
30. Kopecky-Bromberg SA, Martinez-Sobrido L, Frieman M, Baric RA, Palese P (2007) Severe acute respiratory syndrome coronavirus open reading frame (ORF) 3b, ORF 6, and nucleocapsid proteins function as interferon antagonists. J Virol 81: 548–557.
31. van der Hoek L, Sure K, Ihorst G, Stang A, Pyrc K, et al. (2005) Croup Is Associated with the Novel Coronavirus NL63. PLoS Med 2: e240.
32. Frieman M, Ratia K, Johnston RE, Mesecar AD, Baric RS (2009) Severe acute respiratory syndrome coronavirus papain-like protease ubiquitin-like domain and catalytic domain regulate antagonism of IRF3 and NF-kappaB signaling. J Virol 83: 6689–6705.
33. Lindner HA, Fotouhi-Ardakani N, Lytvyn V, Lachance P, Sulea T, et al. (2005) The papain-like protease from the severe acute respiratory syndrome coronavirus is a deubiquitinating enzyme. J Virol 79: 15199–15208.
34. Ratia K, Saikatendu KS, Santarsiero BD, Barretto N, Baker SC, et al. (2006) Severe acute respiratory syndrome coronavirus papain-like protease: structure of a viral deubiquitinating enzyme. Proc Natl Acad Sci USA 103: 5717–5722.
35. Chen Z, Wang Y, Ratia K, Mesecar AD, Wilkinson KD, et al. (2007) Proteolytic processing and deubiquitinating activity of papain-like proteases of human coronavirus NL63. J Virol 81: 6007–6018.
36. Andersen J, VanScoy S, Cheng TF, Gomez D, Reich NC (2008) IRF-3-dependent and augmented target genes during viral infection. Genes Immun 9: 168–175.
37. Grandvaux N, Servant MJ, tenOever B, Sen GC, Balachandran S, et al. (2002) Transcriptional profiling of interferon regulatory factor 3 target genes: direct involvement in the regulation of interferon-stimulated genes. J Virol 76: 5532–5539.
38. Banach BS, Orenstein JM, Fox LM, Randell SH, Rowley AH, et al. (2009) Human Airway Epithelial Cell Culture to Identify New Respiratory Viruses: Coronavirus NL63 as a Model. J Virol Methods 156: 19–26.
39. Seth RB, Sun L, Chen ZJ (2006) Antiviral innate immunity pathways. Cell Res 16: 141–147.
40. Bibeau-Poirier A, Servant MJ (2008) Roles of ubiquitination in pattern-recognition receptors and type I interferon receptor signaling. Cytokine 43: 359–367.
41. Bhoj VG, Chen ZJ (2009) Ubiquitylation in innate and adaptive immunity. Nature 458: 430–437.
42. Isaacson MK, Ploegh HL (2009) Ubiquitination, ubiquitin-like modifiers, and deubiquitination in viral infection. Cell Host Microbe 5: 559–570.
43. Xia ZP, Sun L, Chen X, Pineda G, Jiang X, et al. (2009) Direct Activation of Protein Kinases by Unanchored Polyubiquitin Chains. Nature 461: 114–119.
44. Zeng W, Sun L, Jiang X, Chen X, Hou F, et al. (2010) Reconstitution of the RIG-I pathway reveals a signaling role of unanchored polyubiquitin chains in innate immunity. Cell 141: 315–330.
45. Bowie AG, Unterholzner L (2008) Viral evasion and subversion of pattern-recognition receptor signalling. Nat Rev Immunol 8: 911–922.
46. Meylan E, Curran J, Hofmann K, Moradpour D, Binder M, et al. (2005) Cardif is an adaptor protein in the RIG-I antiviral pathway and is targeted by hepatitis C virus. Nature 437: 1167–1172.
47. Loo YM, Owen DM, Li K, Erickson AK, Johnson CL, et al. (2006) Viral and therapeutic control of IFN-beta promoter stimulator 1 during hepatitis C virus infection. Proc Natl Acad Sci U S A 103: 6001–6006.
48. Lin R, Lacoste J, Nakhaei P, Sun Q, Yang L, et al. (2006) Dissociation of a MAVS/IPS-1/VISA/Cardif-IKKepsilon molecular complex from the mitochondrial outer membrane by hepatitis C virus NS3-4A proteolytic cleavage. J Virol 80: 6072–6083.
49. Chen Z, Benureau Y, Rijnbrand R, Yi J, Wang T, et al. (2007) GB virus B disrupts RIG-I signaling by NS3/4A-mediated cleavage of the adaptor protein MAVS. J Virol 81: 964–976.
50. Yang Y, Liang Y, Qu L, Chen Z, Yi M, et al. (2007) Disruption of innate immunity due to mitochondrial targeting of a picornaviral protease precursor. Proc Natl Acad Sci U S A 104: 7253–7258.
51. Li XD, Sun L, Seth RB, Pineda G, Chen ZJ (2005) Hepatitis C virus protease NS3/4A cleaves mitochondrial antiviral signaling protein off the mitochondria to evade innate immunity. Proc Natl Acad Sci U S A 102: 17717–17722.
52. Ratia K, Pegan S, Takayama J, Sleeman K, Coughlin M, et al. (2008) A noncovalent class of papain-like protease/deubiquitinase inhibitors blocks SARS virus replication. Proc Natl Acad Sci U S A 105: 16119–16124.
53. Friedman CS, O'Donnell MA, Legarda-Addison D, Ng A, Cárdenas WB, et al. (2008) The tumour suppressor CYLD is a negative regulator of RIG-I-mediated antiviral response. EMBO Rep 9: 930–936.
54. Zhang M, Wu X, Lee AJ, Jin W, Chang M, et al. (2008) Regulation of IkappaB kinase-related kinases and antiviral responses by tumor suppressor CYLD. J Biol Chem 283: 18621–18626.
55. Kayagaki N, Phung Q, Chan S, Chaudhari R, Quan C, et al. (2007) DUBA: a deubiquitinase that regulates type I interferon production. Science 318: 1628–1632.
56. Coornaert B, Carpentier I, Beyaert R (2009) A20: central gatekeeper in inflammation and immunity. J Biol Chem 284: 8217–8221.
57. Shembade N, Ma A, Harhaj EW (2010) Inhibition of NF-kappaB signaling by A20 through disruption of ubiquitin enzyme complexes. Science 327: 1135–1139.
58. Wertz IE, O'Rourke KM, Zhou H, Eby M, Aravind L, et al. (2004) De-ubiquitination and ubiquitin ligase domains of A20 downregulate NF-kappaB signalling. Nature 430: 694–699.
59. Stertz S, Reichelt M, Spiegel M, Kuri T, Martínez-Sobrido L, et al. (2007) The intracellular sites of early replication and budding of SARS-coronavirus. Virology 361: 304–315.

OPEN ACCESS Freely available online

PLoS one

Host Genetics and Chlamydia Disease: Prediction and Validation of Disease Severity Mechanisms

Isao Miyairi[1,2,6]*, Jesse Ziebarth[1], Jonathan D. Laxton[1], Xiaofei Wang[1], Nico van Rooijen[4], Robert W. Williams[3], Lu Lu[3,5], Gerald I. Byrne[1], Yan Cui[1]*

1 Department of Microbiology, Immunology & Biochemistry, University of Tennessee Health Science Center, Memphis, Tennessee, United States of America, **2** Department of Pediatrics, University of Tennessee Health Science Center, Memphis, Tennessee, United States of America, **3** Department of Anatomy and Neurobiology, University of Tennessee Health Science Center, Memphis, Tennessee, United States of America, **4** Department of Molecular Cell Biology,Vrije Universiteit Medical Center, Amsterdam, The Netherlands, **5** Jiangsu Key Laboratory of Neuroregeneration, Nantong University, Nantong, China, **6** Division of Infectious Diseases, National Center for Child Health and Development, Tokyo, Japan

Abstract

Genetic mapping studies may provide association between sequence variants and disease susceptibility that can, with further experimental and computational analysis, lead to discovery of causal mechanisms and effective intervention. We have previously demonstrated that polymorphisms in immunity-related GTPases (IRG) confer a significant difference in susceptibility to *Chlamydia psittaci* infection in BXD recombinant mice. Here we combine genetic mapping and network modeling to identify causal pathways underlying this association. We infected a large panel of BXD strains with *C. psittaci* and assessed host genotype, IRG protein polymorphisms, pathogen load, expression of 32 cytokines, inflammatory cell populations, and weight change. Proinflammatory cytokines correlated with each other and were controlled by a novel genetic locus on chromosome 1, but did not affect disease status, as quantified by weight change 6 days after infection In contrast, weight change correlated strongly with levels of inflammatory cell populations and pathogen load that were controlled by an IRG encoding genetic locus (*Ctrq3*) on chromosome 11. These data provided content to generate a predictive model of infection using a Bayesian framework incorporating genotypes, immune system parameters, and weight change as a measure of disease severity. Two predictions derived from the model were tested and confirmed in a second round of experiments. First, strains with the susceptible IRG haplotype lost weight as a function of pathogen load whereas strains with the resistant haplotype were almost completely unaffected over a very wide range of pathogen load. Second, we predicted that macrophage activation by *Ctrq3* would be central in conferring pathogen tolerance. We demonstrated that macrophage depletion in strains with the resistant haplotype led to neutrophil influx and greater weight loss despite a lower pathogen burden. Our results show that genetic mapping and network modeling can be combined to identify causal pathways underlying chlamydial disease susceptibility.

Citation: Miyairi I, Ziebarth J, Laxton JD, Wang X, van Rooijen N, et al. (2012) Host Genetics and Chlamydia Disease: Prediction and Validation of Disease Severity Mechanisms. PLoS ONE 7(3): e33781. doi:10.1371/journal.pone.0033781

Editor: Bernhard Kaltenboeck, Auburn University, United States of America

Received October 27, 2011; **Accepted** February 17, 2012; **Published** March 16, 2012

Copyright: © 2012 Miyairi et al. This is an open-access article distributed under the terms of the Creative Commons Attribution License, which permits unrestricted use, distribution, and reproduction in any medium, provided the original author and source are credited.

Funding: This work was funded by AI081050 (IM, YC, LL), 09GBIA2050135 (IM), Children's Infection and Defense Center Grant (IM), BAA08-1 (GIB, IM), AI19782 (GIB), AI30040 (GIB). The funders had no role in study design, data collection and analysis, decision to publish, or preparation of the manuscript.

Competing Interests: The authors have declared that no competing interests exist.

* E-mail: miyairi-i@ncchd.go.jp (IM); ycui2@uthsc.edu (YC)

Introduction

The genus *Chlamydia* comprises a number of species of highly related obligate intracellular prokaryotic pathogens that cause clinical disease in humans ranging from blinding trachoma [1] and sexually transmitted infection by *Chlamydia trachomatis* [2], community acquired pneumonia by *Chlamydia pneumoniae* [3] and life-threatening respiratory and systemic zoonosis by *Chlamydia psittaci* [4]. In a previous study, we determined that a known QTL on chromosome 11 (*Ctrq3*) [5,6] containing two polymorphic innate immune genes (*Irgm2* and *Irgb10*) in the family of immunity-related GTPases (IRG) were responsible for the innate difference in susceptibility to a systemic infection to *C. psittaci* among the BXD recombinant inbred strains [7]. Each member of this mouse reference strain set inherits a unique and approximately equal fraction of their genomes from two fully inbred progenitors—strain C57BL/6J (B6 or B) and DBA/2J (D2 or D). These two parental strains differ at roughly 5 million sites across the genome. The set of 80 BXD strains is being used for systematic multiscalar genetic studies of host-pathogen interactions [8,9,10]. This large set of genetically related strains can provide comparatively high precision mapping, with a resolution of 1–2 Mb in several cases [7,11]. Characterization of the disease susceptibility differences between the B6 and D2 parental strains revealed significant differences in *C. psittaci* load, inflammatory responses, and cytokine profiles. While the IRGs have been shown to control *Chlamydia* load [6,7,12], alternative immunomodulatory functions of these genes have also been reported [13,14,15] making it unclear if IRGs influence disease outcome by regulating pathogen load or by influencing other immunomodulatory functions [16].

Recent advances in high-throughput genomic technologies and computational methods allow us to formulate and test genetic network models without explicit data on molecular function. Translating large-scale genomic data into network models with

predictive power is a challenging task. The most valid approach is to systematically evaluate the possible hypothetical network models against data and then select the most probable models for experimental validation. The probability of a genetic network model conditioned on the data can be calculated using Bayesian network methods. A Bayesian network is a graphic probabilistic model representing the dependence structure among multiple interacting variables [17,18,19]. The probabilistic modelling provides a natural treatment for the stochastic aspects of biological processes and noisy measurements [20]. Bayesian networks can be used to integrate prior knowledge and new data to capture and express causal relationships [21,22,23].

We combined forward genetics and Bayesian network analysis to model the biological pathway of how *Ctrq3* or polymorphisms in immunity-related GTPases (IRGs) confer susceptibility and resistance to *Chlamydia* infection in strains of mice with different genetic backgrounds. We then predicted how individual mice would respond to different intervention and validated these predictions. The model predicted that *Ctrq3* confer protection against disease through macrophage activation, which then controls pathogen load and neutrophil influx. The factor with the greatest impact on disease severity, as quantified by weight change in strains infected with *Chlamydia*, was predicted to be neutrophil influx rather than pathogen load. We validated these predictions experimentally. Thus, our work provides an experimentally validated model for an immune-regulatory function of the IRG containing *Ctrq3* locus in contributing to the control of systemic *C. psittaci* infection.

Results

Immune responses and disease severity to *Chlamydia psittaci* infection is controlled by two major genetic loci

We infected the C57BL/6J parental strain and 40 BXD strains intraperitoneally, and measured peak *C. psittaci* load, levels of macrophages and neutrophils in the peritoneal cavity, 32 cytokines on days 3 and 6; and disease status as quantified by the weight change from the day of infection. Strains exhibited a spectrum of disease ranging from 30% weight loss to 10% weight gain over 6 days. Significant variation in cytokine protein expression was detected for 17 of 32 cytokines (all results will be deposited and will be accessible in GeneNetwork, www.genenetwork.org). We confirmed that the previously mapped and cloned *Ctrq3* locus on chromosome 11 is a major controller of weight change, macrophage activation status (MAS), level of neutrophil recruitment, and *C. psittaci* load on day 6 (Figure 1). A novel secondary locus was mapped to distal Chr 1 at ~190 Mb. This locus modulates levels of several key cytokines—GM-CSF, IL1a, MIP1a, MIP1b, MIP2—but has no effect on disease severity as measured by weight changes (Figure 2). To further investigate the influence of the genetic polymorphisms at *Ctrq3*, we analyzed the expression pattern of the IRGM2 protein in the peritoneal lavage specimens from infected BXD strains and found that it had two distinct band sizes that are directly correlated with the *Ctrq3* genotype [7].

Correlation network analysis reveals the immune phenotypes associated with disease severity

We constructed a correlation network, including cytokines, genotypes, immune parameters and disease phenotypes (Figure 3). The network nodes clustered into two groups. The first group correlated tightly with the *Ctrq3* genotype, IRGM2 expression pattern and several disease-related parameters, including weight change, macrophage activation status (MAS), pathogen load, and neutrophil recruitment. A single cytokine, G-CSF, had a high correlation with weight change and neutrophil level, but was not controlled by *Ctrq3* (Figure 1E. no significant QTL). The second group comprised the cytokines, many of which are highly correlated with each other, and the genotype at rs13476293, a marker located at ~190 Mb on Chr 1, but not directly with disease-related parameters.

Bayesian network model identifies the central role of macrophages in the disease pathway

We constructed a Bayesian network model to identify casual pathways through which genotype at *Ctrq3* influences disease outcome after infection with *C. psittaci* (Figure 4). The Bayesian network included variables that were highly correlated with weight change and influenced by the genotype at *Ctrq3*: IRGM2 expression pattern, macrophage activation status, neutrophils, and pathogen load. Because of the perfect correlation between the *Ctrq3* genotype and IRGM2 expression pattern, these variables were combined into a single node. In the most likely model structure, the genotype at *Ctrq3* was the immediate parent of all of the other variables in the model, signifying that each of these variables is directly influenced by the genotype. However, the model also suggests that *Ctrq3* genotype was not sufficient in explaining these variables, as there were additional conditional dependencies in the model structure. Weight change, for example, was directly influenced by neutrophil recruitment and macrophage activation status (MAS) in addition to genotype at *Ctrq3*, indicating that the levels of neutrophils and MAS influences weight change independent of the *Ctrq3* genotype. The model also suggested that macrophage activation influences weight change via regulation of neutrophil recruitment but not by pathogen load restriction.

Macrophage and neutrophil influx levels defines disease severity

We used the Bayesian network model to investigate the effect of depletion of macrophages on neutrophil influx, *C. psittaci* load, and weight change (Figure 5 network C and D). To discretize the predictions of the model, a threshold was determined by averaging the mean value of strains with a B genotype and the mean value of strains with a D genotype for the original data sample. Then, the probability that the predicted value for each variable was greater than (High) or less than (Low) this threshold was calculated from the conditional Gaussian distributions learned from the network for the original data and after macrophage depletion (Methods). Nodes with a yellow background have been assigned the value to represent data for only a given genotype and status of intervention on MAS. The magnitude of these changes is expected to be much more pronounced in strains with a B genotype at *Ctrq3* than in strains with a D genotype at this locus. (Figure 5 and Figure S2) Strains with the D genotype at *Ctrq3* typically have innately low macrophage activation, and as a result the model predicts only slight changes in the levels of neutrophils, pathogen load, and weight after depleting macrophages.

We tested these predictions by performing chemical depletion of macrophages with clodronate before infecting B6 and D2 strains with *C. psittaci*. The experiments validated many of the model's predictions (Figure 6). In the D2 strain, depletion of macrophages increased neutrophil influx, *C. psittaci* load, and induced a more rapid decline in weight and mice were therefore euthanized on day 4 post infection. Pathogen load in the liver was greater in macrophage depleted mice by nearly 2 logs (PBS control: 1.21×10^5 IFU/gram, Clodronate treated; 9.37×10^6 IFU/gram, $p = 0.03$). As predicted, in the resistant B6 strain, depletion of

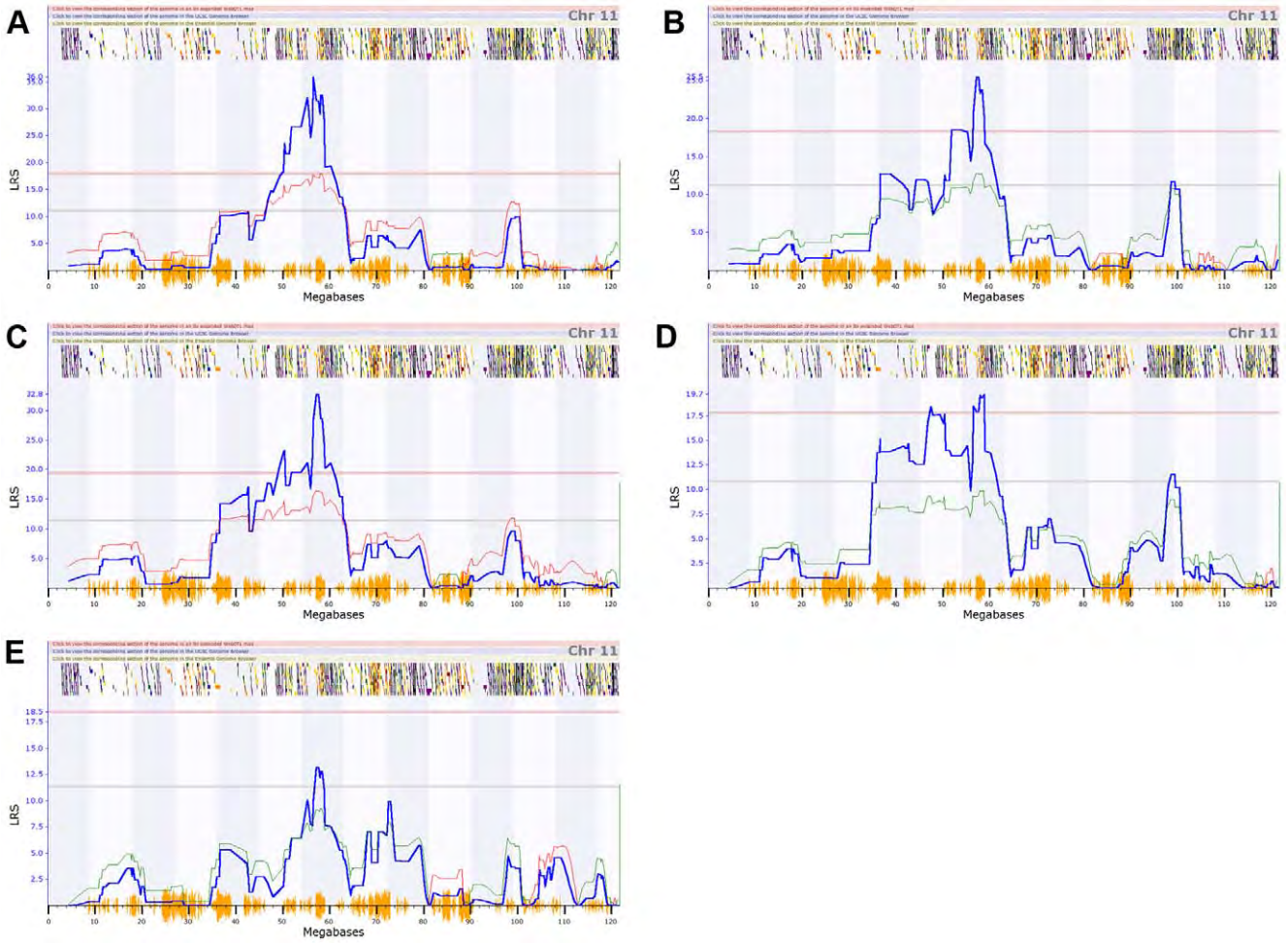

Figure 1. Association of the *Ctrq3* locus with immune parameters and disease status. QTL mapping results for (A) day 6 weight, (B) neutrophils, (C) macrophage activation status, (D) *C. psittaci* load, and (E) G-CSF on chromosome 11. *Ctrq3* is located near 58 Mb on chr 11. Significant (genome-wide adjusted $p<0.05$) and suggestive (adjusted $p<0.63$) QTLs are indicated by the solid red and grey lines, respectively. Blue lines indicate the likelihood-ratio statistic (LRS) that the phenotype is associated with the genomic locus. The colored lines following the trend of the LRS show the additive effect of the influence of the locus, with red lines indicating that D alleles increase trait values, while green alleles indicate that B alleles increase trait values.
doi:10.1371/journal.pone.0033781.g001

macrophages increased neutrophils and exacerbated the weight loss. These mice were moribund 5 days post-infection. Pathogen load in the liver was similar in B6 irrespective of whether macrophages were depleted or not (PBS control: 4.26×10^6 IFU/gram, Clodronate treated; 3.81×10^6 IFU/gram, $p=0.06$) but their peritoneal pathogen load was decreased after depleting macrophages, suggesting that pathogen load restriction may not be entirely responsible for controlling disease severity.

Ctrq3 confers genetic resistance and tolerance to Chlamydia

Several reports have documented that IRGs reduce pathogen burden in vitro and in vivo, which is expected to influence disease severity [6,7,12,24]. To investigate the possibility that the status of the *Ctrq3* genotype switches disease modality, we performed the Bayesian analysis for strains with the B genotype at the *Ctrq3* locus separately from strains with the D genotype. The influence of load on weight change was much stronger for strains with the susceptible D genotype than strains with the resistant B genotype (described further in Methods). Because of the genotype-specific switching between pathogen load and weight change in the model, we expanded this analysis to 197 BXD mice and correlated the weight loss with pathogen load in individual mice according to the genotype at the *Ctrq3* locus (Figure 7). Overall, mice with the B genotype had lower pathogen load compared to mice with a D genotype, although a considerable overlap existed. The mice with the B genotype were tolerant of increases in pathogen burden whereas mice with D genotype lost more weight with increases in pathogen burden as demonstrated by the differences in the slope of the load to weight linear regression lines ($p=0.02$).

Discussion

Individualized medicine requires the capability of predicting an individual's susceptibility to diseases and response to medical treatments, based on genetic profile. Individual differences in disease susceptibility and response to therapeutic interventions are complex phenotypes modulated by genetic factors. We formulated an approach using Bayesian networks to model the pathways through which gene variants operate on phenotypes. Results of our study demonstrate experimental validation of the combined

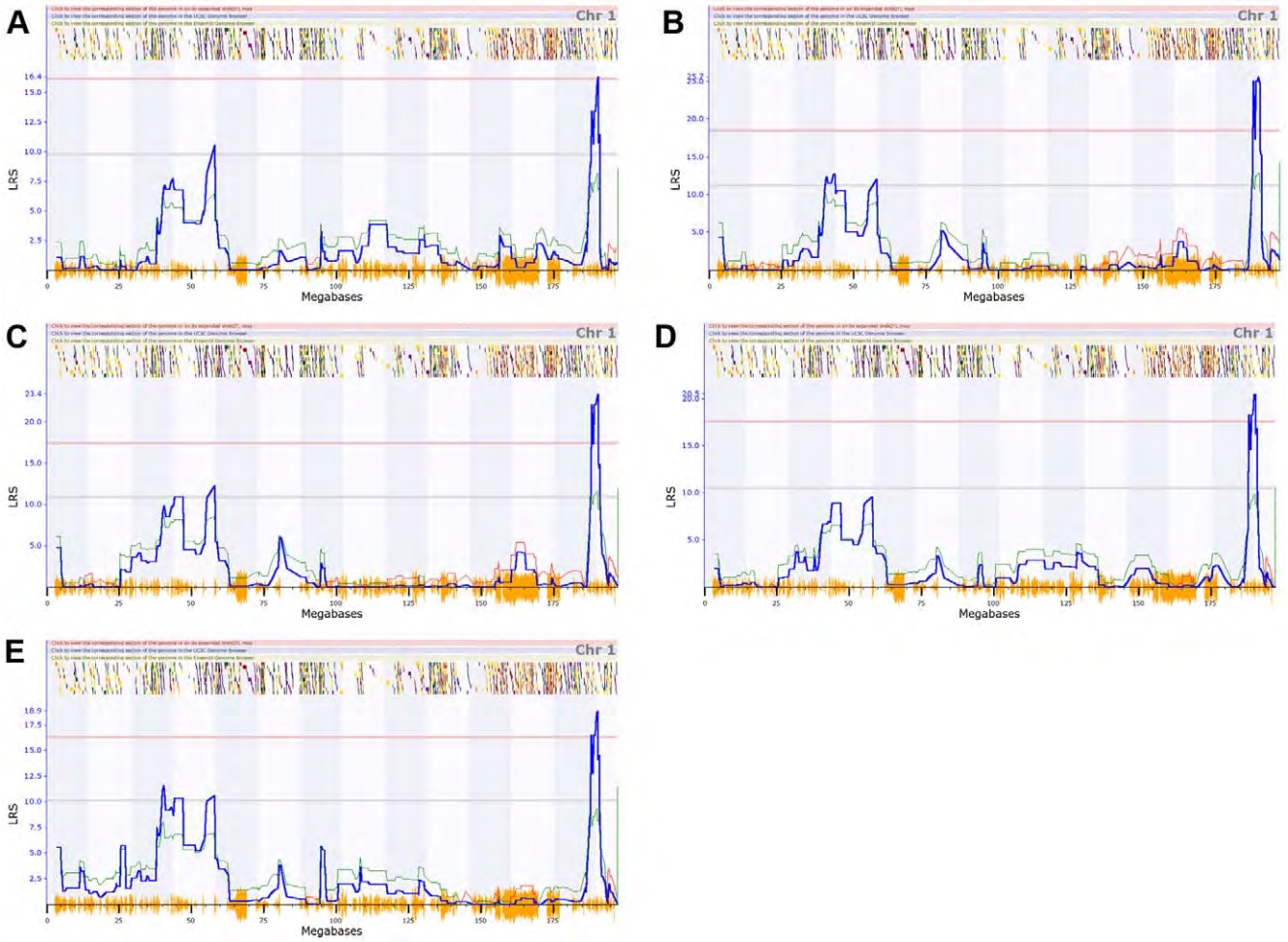

Figure 2. A QTL on chromosome 1 regulating cytokines. QTL mapping results for (A) GM-CSF, (B) IL-1a, (C) MIP-1a, (D) MIP-1b, and (E) MIP-2 on chromosome 1. Significant (genome-wide adjusted $p<0.05$) and suggestive (adjusted $p<0.63$) QTLs are indicated by the solid red and grey lines, respectively. Blue lines indicate the likelihood-ratio statistic (LRS) that the phenotype is associated with the genomic locus. The colored lines following the trend of the LRS show the additive effect of the influence of the locus, with red lines indicating that D alleles increase trait values, while green alleles indicate that B alleles increase trait values.
doi:10.1371/journal.pone.0033781.g002

systems genetics and Bayesian network approaches to immune pathway modeling and disease prediction. This approach provides a way to develop models for designing genetic association studies that can define causal pathways with the predictive power required in individualized medicine.

We had previously demonstrated that *Ctrq3* controls systemic *C. psittaci* disease outcome and found an association with IRG polymorphisms. While IRGs have cell autonomous functions of pathogen restriction, the immunological pathway that links this genotype to phenotype has not been defined. It has recently been reported that infected hosts employ two different strategies to defend themselves against pathogens—resistance and tolerance [25,26,27]. Resistance is defined as the ability to limit pathogen burden, whereas tolerance is defined as the ability to limit the damage caused by a given pathogen burden [28,29]. While most studies on genetic susceptibility to infectious diseases implicate resistance as a mechanism of host protection, there are several examples of genetic tolerance to infection in animal models [29,30,31].

In this study, we predicted that *Ctrq3* conferred resistance but with relatively little impact on weight change. We also predicted an expanded role for *Ctrq3* that included macrophage activation and weight change. Indeed mice with a B6 genotype at the *Ctrq3* locus tended to have a lower pathogen load than mice with D2 genotype and thus were more resistant. However, there was significant variability in the pathogen load within mice with the same genotype suggesting the presence of other factors that affect resistance. The mechanism of resistance by *Ctrq3* is likely to be due to the cell autonomous bactericidal functions of the B6 derived *Irgb10* and *Irgm2* genes given results of our previous ex vivo siRNA experiments [5,6,7]. On the other hand, we found that mice with a B6 genotype at the *Ctrq3* locus can maintain body weight over a wide range of pathogen load and thus have tolerance to *C. psittaci* infection. In contrast, mice with a D2 genotype lost weight as a function of increased pathogen burden and were thus less tolerant. The molecular basis of tolerance is still unclear.

An obvious limitation of our model is that we are assessing the function of the 2 MB *Ctrq3* locus. This locus encodes three IRGs (*Irgb10*, *Irgm2*, and *Irgm3*), 18 other genes, as well as non-coding regions with unknown functions. While IRGs remain a primary candidate given its association with immunoregulatory functions [13,14,15,16,32,33], it is possible that resistance and tolerance is

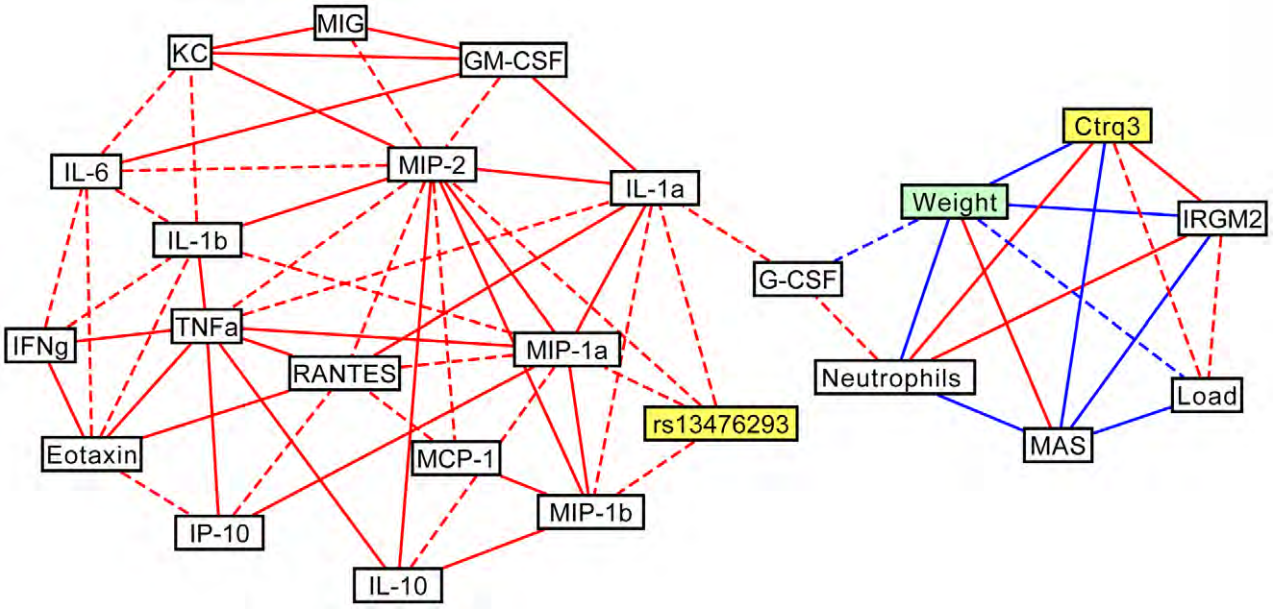

Figure 3. The correlation network of immune parameters during Chlamydia infection in BXD mice. Correlation network linking BXD genotypes (*Ctrq3* and rs13476293), *C. psittaci* load, inflammatory responses, cytokine profiles, IRGM2 protein expression pattern, and weight change after *C. psittaci* infection in BXD strains. Positive (red) and negative (blue) correlations between variables with magnitudes of Pearson's correlation coefficient greater than 0.6 (dashed lines) and 0.7 (solid lines) are shown.
doi:10.1371/journal.pone.0033781.g003

conveyed by one or more of the other genes in this interval. Furthermore, the exact nature of the B6 and D2 Irgm2 alleles (e.g. "wildtype," loss-of-function, hypomorph, constitutively active, etc) is unclear and warrant additional biological validation.

While the mechanism of tolerance is unclear, our model suggests that mice that do not recruit activated macrophages to the site of infection have an increased number of recruited neutrophils and more severe disease as evidenced by greater weight loss. Specifically, Bayesian analysis predicted that mice with a D genotype at the *Ctrq3* locus would lose less weight if neutrophils were depleted (day 6 to day 0 weight ratio: 0.83 for mice without neutrophil depletion and 0.89 with neutrophils depleted) without any change in pathogen load. This prediction was consistent with our previous observations where *Cxcr2* knockout mice that cannot recruit neutrophils to the site of infection, survived challenge without any detectible changes in pathogen load. In contrast, the BALB/c wild type strain succumbed to infection with significant neutrophil recruitment in a manner similar to the D2 strain [7]. We speculate that in our model, loss of tolerance leads to uncontrolled inflammation and severe disease high-lighted by neutrophil influx.

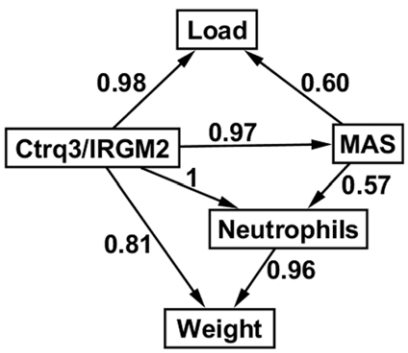

Figure 4. Structure of Bayesian network (BN) model of *C. psittaci* infection. The number next to each directed arc of the BN indicates the confidence (posterior probability) in the arc after model averaging as described in the Methods.
doi:10.1371/journal.pone.0033781.g004

Interestingly, we found that macrophage depleted B6 mice have a reduced number of *C. psittaci* in the infected peritoneal cavity; whereas macrophage depleted D2 mice had a greater number. We also found that after macrophage depletion, *C. psittaci* load in the liver of D2 mice increased by 2 logs whereas loads were similar in the liver of B6 mice. We speculate that in B6 mice, loss of a growth niche led to a decrease in pathogen load, whereas the apparent increase in pathogen load in the peritoneal cavity in D2 mice is being supported by an increase in *C. psittaci* growth in the surrounding tissues. While this indicates there may be a difference in tissue/cell tropism between B6 and D2 mice, the underlying mechanism is unknown at this point.

There are clear limitations of our model and approach. First, we are limited by the variables we chose to screen, which did not account for various other cell types, cytokines, physiological parameters, etc. Second, we are limited by the dynamic process of infectious diseases, which include the important variable of time, where our longitudinal analyses were limited (<1 week) due to the severity of disease in D2 mice. Third, we are limited by the nature of the intervention we can employ. In our model, we found that macrophage activation, which occurs gradually over the course of infection, was an important variable that determines disease outcome. In our validation experiment, we eliminated macrophages prior to infection in order to simulate the extreme end of this variable, which may have led to activation of alternative pathways or immune cells. Despite these limitations, our results demonstrate a proof of principal model of how genetic mapping and network modeling can be combined to identify causal pathways underlying infectious disease susceptibility.

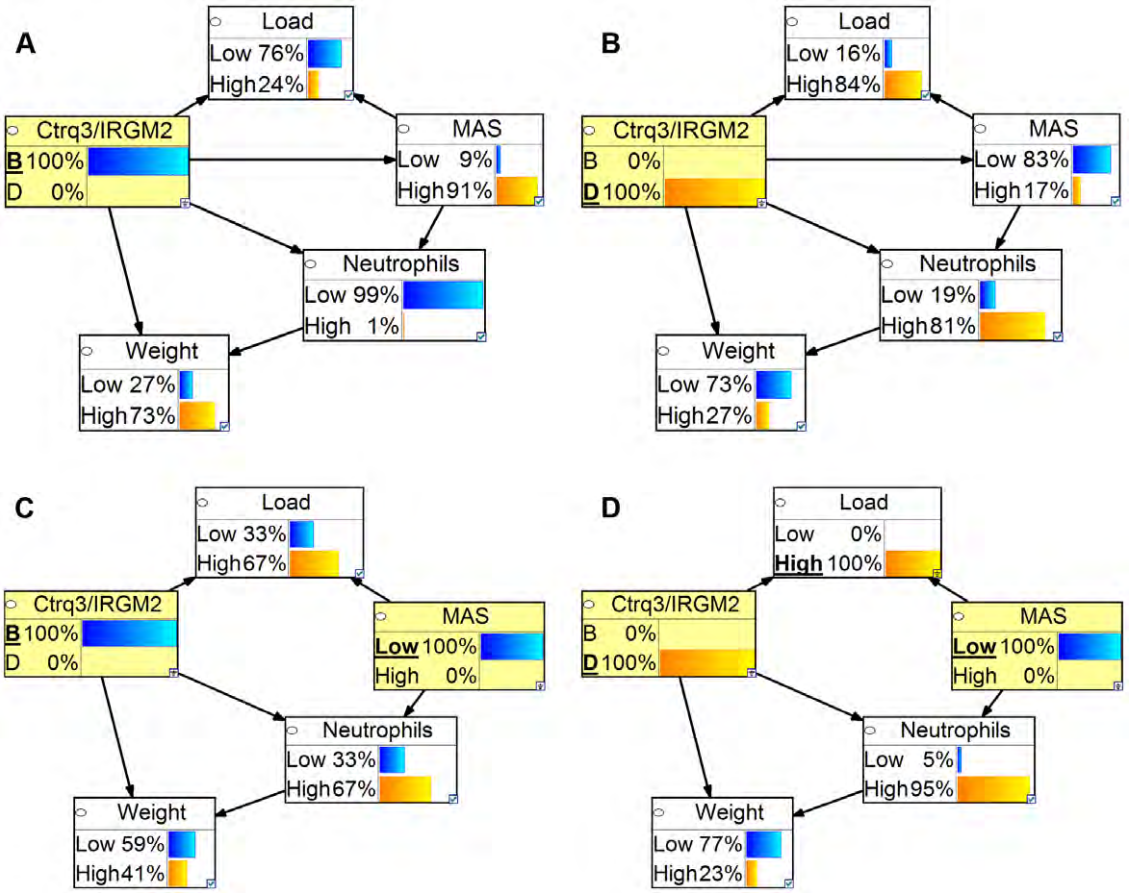

Figure 5. Predictions of the BN as a function of genotype and macrophage intervention. (A and B) Discretized p of the BN as a function of genotype at *Ctrq3*. BXD strains with the susceptible, D, genotype at the IRG locus tend to have lower MAS and weights and higher levels of neutrophils and pathogen load. (C and D) Discretized p effect of interventional depletion of macrophages on the values of variables in the BN.
doi:10.1371/journal.pone.0033781.g005

Materials and Methods

Ethics Statement

This study was carried out in strict accordance with the recommendations in the Guide for the Care and Use of Laboratory Animals of the National Institutes of Health. The protocol (internal protocol number 1709R1) was approved by the Animal Care and Use Committee of the University of Tennessee Health Science Center (PHS assurance# - A-3325-01). No surgical procedures were performed. All efforts were made to minimize suffering.

Infection and sample collection

Chlamydia psittaci infection: *C. psittaci* 6BC was propagated in L cells, titrated and stored at −80C°. Intraperitoneal infection with *C. psittaci* 6BC (10^4 IFU) was performed using the same stock source to minimize variations across experiments. 8–16 week old male mice (C57BL/6J, and 40 BXD strains) were infected in groups of 2 mice/strain. Infected mice were monitored daily for weight changes. On days 3 or 6-post infection, mice were euthanized to obtain peritoneal lavage samples for pathogen load, flow cytometry, and cytokine analysis. Additional mice, totaling 197 mice representing 56 BXD strains, were infected with *C. psittaci* 6BC (10^4 IFU) and monitored for weight changes and euthanized on day 6 for IFU analysis.

Assessment of immune phenotypes

***Chlamydia psittaci* load.** Titration was performed by a cell culture based IFU assay for day 6 samples as previously described [7]. DNA was extracted from 1 ml of peritoneal lavage fluid from day 3 and *C. psittaci* load was measured as a ratio of *C. psittaci* ompA DNA/host GAPDH by quantitative DNA PCR.

Flow cytometry. Standard methods were used as described previously [7]. Briefly, murine peritoneal exudates were blocked with Fc block and incubated with fluorochrome-conjugated antibodies. The following antibodies were used: Macrophage marker; F4/80-APC, Neutrophil marker; Ly6G (clone IA8)-PE, and MHC class II marker; IA/IE-PE. Data was expressed as percent of macrophages or neutrophils in the entire population. MHC class II expression was used as a marker for macrophage activation status and data was expressed as percent of F4/80 positive cells that were also positive for IA/IE.

Cytokine analysis. Peritoneal lavage supernatants were analyzed using the Luminex based Mouse 32-plex kit to analyze levels of 32 cytokines (CATALOG).

Western blot analysis. Peritoneal lavage specimens were analyzed by Western blot analysis using standard methods with GTPI antibody (M-14) Santa Cruz (sc-11088) and secondary antibody using Goat true blot (eBioscience 18-8814-31).

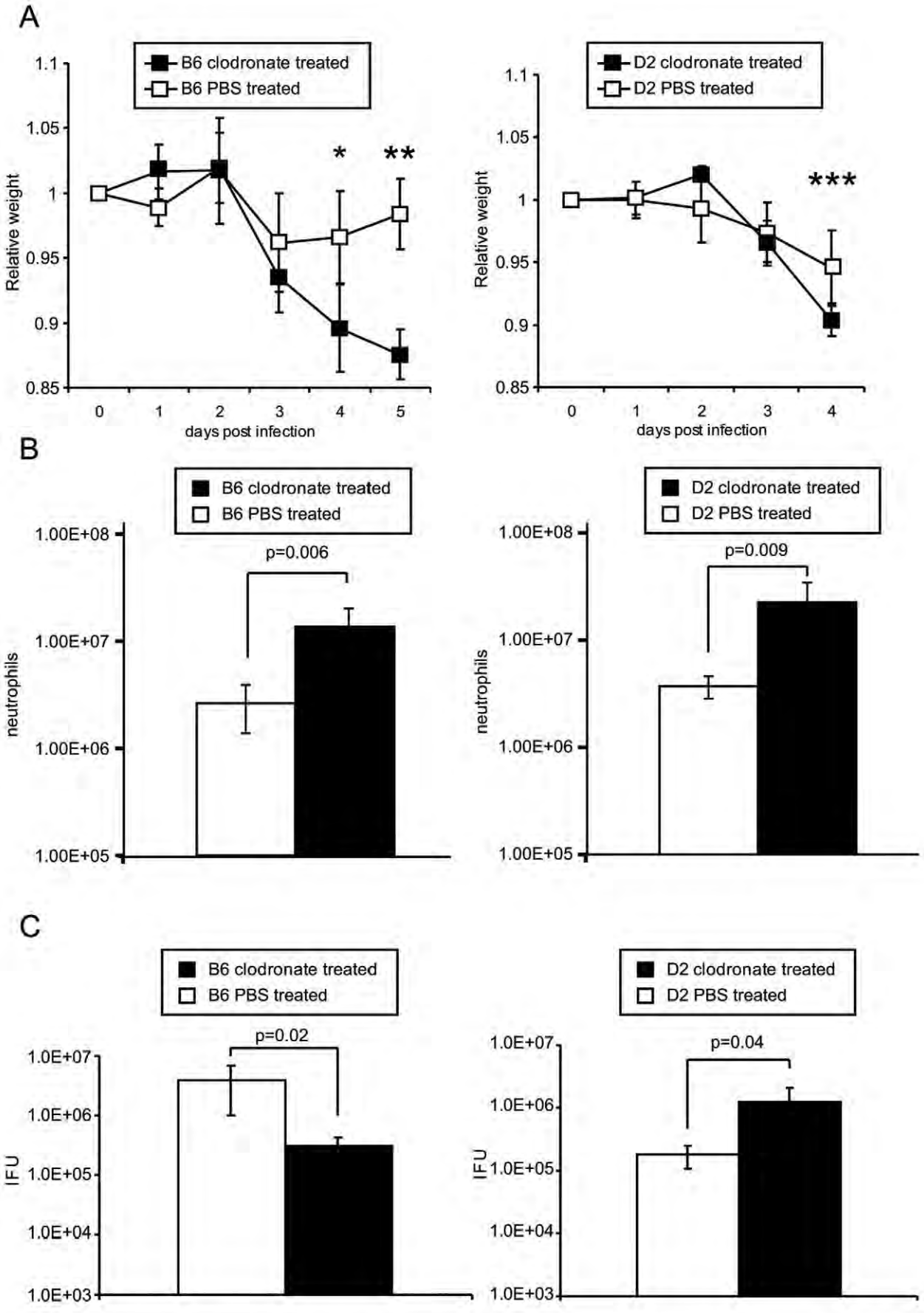
A
B6 clodronate treated
B6 PBS treated
Relative weight
days post infection
*
**
D2 clodronate treated
D2 PBS treated
***
B
neutrophils
p=0.006
p=0.009
C
IFU
p=0.02
p=0.04

Figure 6. Impact of macrophage depletion on the course of *C. psittaci* infection in B6 and D2 strains. B6 and D2 mice received either liposome clodronate or liposome PBS iv (day −1 post infection) and i.p. (day −1, 1, and 3 post infection) and infected with *C. psittaci* 10^4 IFU intraperitoneally (N = 5/group). Mice were monitored daily for weight (A) and appearance. Data points where differences in weight met statistical significance are indicated in asterix (* p = 0.003, ** p = 3.7×10E-5, p = 0.04). Clodronate treated D2 strain became moribund on day 4 and B6 on day 5 post infection and were euthanized. Brackets and p values are provided to indicate differences in, number of neutrophils (B), and *C. psittaci* load (C) between clodronate (black) and liposome (white) treated mice for both B6 and D2 strains. Data is representative of two experiments.
doi:10.1371/journal.pone.0033781.g006

Data analysis

QTL mapping. Quantitative trait locus (QTL) mapping was performed for 17 cytokine profiles that exhibited variation across strains; immune responses including levels of neutrophils, macrophages, and macrophage activation status (MAS); and weight change of BXD strain infection with *C. psittaci* with the GeneNetwork (www.genenetwork.org). Single marker regression was performed across the entire mouse chromosome at 3795 markers typed across BXD strains. A likelihood ratio statistic (LRS) was calculated at each marker comparing the hypothesis that the marker is associated with the phenotype with the null hypothesis that there is no association between marker and phenotype. Genome-wide significance was determined by performing 1000 permutations. Two significant (genome-wide p-value$<$0.05) QTLs were found: one QTL was located near 55 Mb on chromosome 11 and was associated with weight change, MAS, pathogen load, and neutrophil levels (Figure 1), while the other significant QTL was located on chromosome 1 near 190 Mb and was associated with several cytokines (Figure 2).

Bayesian network modeling. Structural learning of the Bayesian network was performed using the R package *deal* (http://cran.r-project.org/web/packages/deal/index.html). The network was constructed from data for C57BL/6J and 40 BXD strains using one discrete node, representing the *Ctrq3* genotype and IRGM2 protein expression pattern, and four continuous nodes (neutrophils, *C. psittaci* load, macrophage activation status, and the ratio of the weight of the mice 6 days after infection to the weight before infection), which were modeled with conditional Gaussian distributions. The Bayesian network score [34], which is basically a version of the BDe scoring metric [35] extended to include

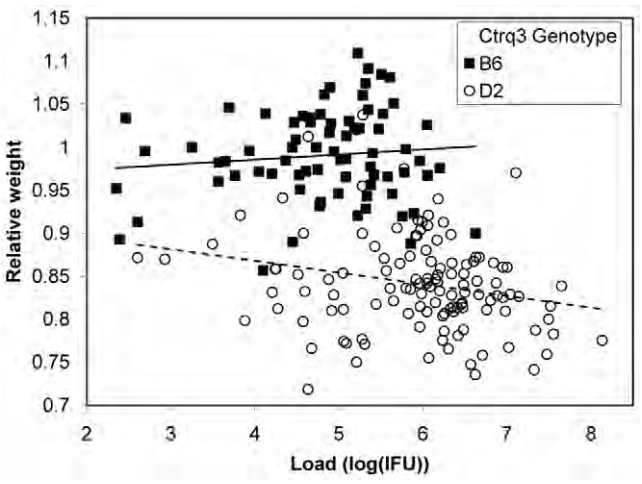

Figure 7. Genetic resistance and tolerance to Chlamydia infection in mice. Plot of weight change as a function of IFU for 197 BXD mice infected with *C. psittaci*. Mice with the susceptible D genotype at the *Ctrq3* (open symbols) lose weight as pathogen load increases, while mice with the resistant B genotype at the *Ctrq3* marker (filled circles) do not. The slopes of the linear regression lines for the B (solid line) and D (dashed line) data are significantly different (p = 0.02).
doi:10.1371/journal.pone.0033781.g007

conditional Gaussian distributions, was calculated in *deal* for all, except those that violated two restrictions. First, potential models in which the genotype node was the child of any other nodes in the network were not considered. This restriction does not require that the genotype node be the parent of the other nodes, as model structures in which continuous nodes were independent of genotype were allowed. Second, the weight node could not be the parent of any other node. The Bayesian score metric inherently handles the problem of over fitting data to complex models [36]. However, selecting a single best network model and ignoring all other models may still lead to over-fitting the data. Model averaging can be used to reduce this risk [37]. An indicator function f is defined as: if a network G learned from data D has the feature (here a feature is a directed edge representing a regulatory relationship), $f(G)=1$, otherwise, $f(G)=0$. The posterior probability of a feature is $P(f(G)|D)=\sum_G f(G)P(G|D)$. This probability reflects our confidence in the feature f. We calculated the posterior probability of features by averaging over all possible models, with the restrictions noted above. All features with a posterior probability greater than 0.5 were included in the network.

The reproducibility of the structure learning method was investigated with the use of simulated data. Briefly, the model learned for the original network was used to generate simulated data sets. Then, the structure learning method was repeated with the simulated data sets and the network structures learned from the simulated data sets were compared to the structure of the original network. A high correspondence between the simulated structures and the original structure indicates that the size of the original data set was sufficient to learn the structure of the network. To create the simulated data, parameter learning of the network was performed with the maximum likelihood estimator provided in the Bayes Net Toolbox [38], available for download at: http://code.google.com/p/bnt/. Before the parameters of the network were learned, the data for the four continuous nodes was normalized to have a mean of 0 and standard deviation of 1. 1000 simulated data sets with 41 samples were then generated with the sample_bnet function of the Bayes Net Toolbox. The structure learning method used to learn the original network was then used for each of the simulated data sets. The edges in the original network were highly reproduced in the simulated data (Figure S1).

Prediction of effects of macrophage depletion. We predicted the effects of intervention using a hybrid Bayesian network including both the discrete genotype node and continuous nodes modeled with conditional Gaussian distributions with the Bayes Net Toolbox. The parameters of the network were learned with a maximum likelihood approach. Macrophage depletion is an external intervention to the model. The intervention sets the value of the MAS node and relieves it from the influence of its parent node. Therefore, prediction was performed by removing the link *Ctrq3*/IRGM2→MAS and setting macrophage activation status to the minimum value observed in the data used for parameter learning [action *do* (MAS = MIN), where MIN = 0,032 is the minimum observed MAS value]. The probabilistic inference was executed using the Bayes Net Toolbox. The effects of macrophage depletion on the parameters of the conditional Gaussian

distributions for each node are compared in Table S1 and Figure S2. Depletion of macrophages causes increases in the levels of neutrophils and pathogen load and decreased weight. The magnitude of these changes is larger for mice with the D genotype at *Ctrq3*.

Bayesian network cross-validation. Leave-one-out cross validation was also used to test the performance of the hybrid Bayesian network. For each test strain, parameter learning of the remaining 40 strains and inference was performed with the Bayes Net Toolbox with the methods mentioned above. To evaluate the quality of the continuous predictions, we used the Q^2 parameter [39], which is given by:

$$Q^2 = 1 - \frac{\sum (y_i - \hat{y}_i)^2}{\sum (y_i - \bar{y})^2}$$

where y_i is the value of the ith sample, $\hat{y}_i$ is the predicted value of the ith sample, and $\bar{y}$ is the sample mean. The values of Q^2 for MAS, neutrophil level, pathogen load, and weight were 0.51, 0.59, 0.45, and 0.68, respectively. Additionally, we discretized the original data and the predictions from the leave-one-out-cross validation for each strain and used this discretized data to test the accuracy of the predictions. A threshold for each of the continuous variables was determined by averaging the mean value of the original data for all strains with the B genotype and the mean value for all strains with the D genotype. Then, the continuous variables for the original data and the predictions were classified as being either High or Low through comparison with these threshold values for each strain. The accuracy was then determined by dividing the number of predictions that matched the original data by the total number of strains. For MAS, neutrophil level, pathogen load, and weight, the accuracy was accuracy 85%, 93%, 80%, and 88%, respectively.

Strain dependent influence of pathogen load on weight change after infection: To test if the arc from pathogen load to weight ratio was genotype dependent, the data for mice with B and D genotypes at the *Ctrq3* locus were separated. As each data set only contained data from strains with one genotype, the genotype node was removed from the network, and the structure of the network, using model averaging of an exhaustive search of possible structures with *deal*, was learned for both the B and D data. For strains with the D genotype, a directed edge from pathogen load to weight ratio had a posterior probability of 0.64, while the same edge for strains with the B genotype had a posterior probability of only 0.16, indicating that weight change was dependent on *C. psittaci* load only for strains with the susceptible D genotype. This conclusion was confirmed by grouping the pathogen load and weight ratio for a total of 197 mice into B and D groups using the genotype at *Ctrq3*. Slopes of the linear regression lines of pathogen load vs. weight ratio for each group were calculated and compared using the analysis of covariance tool in Matlab 7.8 (R2009a). The slopes of the lines were significantly different with a p-value of 0.02.

Validation experiments

B6 and *D2* mice were each grouped into two groups (N = 5) that received clodronate containing liposome or PBS containing liposome injections on day −1, 1, 3, 5 (day −1: 200 uL iv, 200 uL i.p., day 1, 3, 5: 200 uL i.p.) [40]. All mice were infected on day 0 with *C. psittaci* 6BC at 10^4 IFU i.p. and monitored daily for weight changes. On day 6 post infection, mice were euthanized and peritoneal lavage was obtained. The peritoneal lavage was processed for pathogen load, cell population (number of neutrophils and macrophages) and macrophage activation status by flow cytometry as described before. The total number of cells in the lavage was enumerated by cytometer and total numbers of neutrophils were calculated.

Supporting Information

Figure S1 Reproducibility of network structures. The number next to each edge is the fraction of times that the edge was present in the structure of 1000 simulated data sets. The simulated data sets were generated from the parameters of the original network and contained 41 samples, the same number of samples as in the original data set. The structure learning method used for the simulated data sets was the same as that used for the original network. No edges not present in the original network occurred in more than 0.29 of the simulated data sets.
(TIF)

Figure S2 Effect of macrophage depletion on predictions of continuous data by Bayesian network. Probability density functions for Gaussian distributions describing the predicted values of macrophage activation status (A), pathogen load (B), neutrophils (C), and weight (D) in normal mice (solid lines) and in mice with depleted macrophages after treatment with clodronate (dashed lines). The effect of macrophage depletion has a much larger effect on predictions for mice with the resistant B6 genotype (blue lines) than with the susceptible D2 genotype (orange lines).
(TIF)

Table S1 Mean values of Bayesian network predictions as a function of genotype and macrophage intervention.
(DOC)

Author Contributions

Conceived and designed the experiments: IM JZ YC. Performed the experiments: IM JZ JDL XW YC. Analyzed the data: IM JZ YC GIB. Contributed reagents/materials/analysis tools: LL RWW NvR. Wrote the paper: IM JZ YC GIB RWW.

References

1. Burton MJ, Mabey DC (2009) The global burden of trachoma: a review. PLoS Negl Trop Dis 3: e460.
2. Centers for Disease Control and Prevention (2009) Chlamydia Prevalence Monitoring Project Annual Report 2007. Atlanta, GA.
3. Hammerschlag M, Kohlhoff S, Apfalter P (2009) Chlamydophila (Chlamydia) pneumoniae. In: Mandell G, Bennett J, Dolin R, eds. Mandell, Douglan, and Bennett's Principles and Practice of Infectious Diseases. 7th ed. Philadelphia, PA: Churchill Livingstone.
4. Beeckman DS, Vanrompay DC (2009) Zoonotic Chlamydophila psittaci infections from a clinical perspective. Clin Microbiol Infect 15: 11–17.
5. Bernstein-Hanley I, Balsara ZR, Ulmer W, Coers J, Starnbach MN, et al. (2006) Genetic analysis of susceptibility to Chlamydia trachomatis in mouse. Genes Immun 7: 122–129.
6. Bernstein-Hanley I, Coers J, Balsara ZR, Taylor GA, Starnbach MN, et al. (2006) The p47 GTPases Igtp and Irgb10 map to the Chlamydia trachomatis susceptibility locus Ctrq-3 and mediate cellular resistance in mice. Proc Natl Acad Sci U S A 103: 14092–14097.
7. Miyairi I, Tatireddigari VR, Mahdi OS, Rose LA, Belland RJ, et al. (2007) The p47 GTPases Iigp2 and Irgb10 regulate innate immunity and inflammation to murine Chlamydia psittaci infection. J Immunol 179: 1814–1824.
8. Boon AC, deBeauchamp J, Hollmann A, Luke J, Kotb M, et al. (2009) Host genetic variation affects resistance to infection with a highly pathogenic H5N1 influenza A virus in mice. J Virol 83: 10417–10426.
9. Abdeltawab NF, Aziz RK, Kansal R, Rowe SL, Su Y, et al. (2008) An unbiased systems genetics approach to mapping genetic loci modulating susceptibility to severe streptococcal sepsis. PLoS Pathog 4: e1000042.

10. Kotb M, Fathey N, Aziz R, Rowe S, Williams RW, et al. (2008) Unbiased forward genetics and systems biology approaches to understanding how gene-environment interactions work to predict susceptibility and outcomes of infections. Novartis Found Symp 293: 156–165; discussion 165–157, 181–153.
11. Mozhui K, Ciobanu DC, Schikorski T, Wang X, Lu L, et al. (2008) Dissection of a QTL hotspot on mouse distal chromosome 1 that modulates neurobehavioral phenotypes and gene expression. PLoS Genet 4: e1000260.
12. Nelson DE, Virok DP, Wood H, Roshick C, Johnson RM, et al. (2005) Chlamydial IFN-gamma immune evasion is linked to host infection tropism. Proc Natl Acad Sci U S A 102: 10658–10663.
13. Taylor GA (2007) IRG proteins: key mediators of interferon-regulated host resistance to intracellular pathogens. Cell Microbiol 9: 1099–1107.
14. Howard J (2008) The IRG proteins: a function in search of a mechanism. Immunobiology 213: 367–375.
15. Feng CG, Collazo-Custodio CM, Eckhaus M, Hieny S, Belkaid Y, et al. (2004) Mice deficient in LRG-47 display increased susceptibility to mycobacterial infection associated with the induction of lymphopenia. J Immunol 172: 1163–1168.
16. Hunn JP, Howard JC (2010) The mouse resistance protein Irgm1 (LRG-47): a regulator or an effector of pathogen defense? PLoS Pathog 6: e1001008.
17. Pearl J (1988) Probabilistic Reasoning in Intelligent Systems. California: Morgan Kaufmann Publishers.
18. Pearl J (2000) Causality: Models, Reasoning, and Inference. Cambridge, UK: Cambridge University Press.
19. Neapolitan RE (2003) Learning Bayesian Networks. Upper Saddle River: Prentice Hall.
20. de Jong H (2002) Modeling and Simulation of Genetic Regulatory Systems: A Literature Review. Journal of Computational Biology 9: 67–103.
21. Needham CJ, Bradford JR, Bulpitt AJ, Westhead DR (2007) A Primer on Learning in Bayesian Networks for Computational Biology. PLoS Computational Biology 3: e129.
22. Rockman MV (2008) Reverse engineering the genotype-phenotype map with natural genetic variation. Nature 456: 738.
23. Friedman N (2004) Inferring cellular networks using probabilistic graphical models. Science 303: 799–805.
24. MacMicking JD, Taylor GA, McKinney JD (2003) Immune control of tuberculosis by IFN-gamma-inducible LRG-47. Science 302: 654–659.
25. Raberg L, Sim D, Read AF (2007) Disentangling genetic variation for resistance and tolerance to infectious diseases in animals. Science 318: 812–814.
26. Best A, White A, Boots M (2008) Maintenance of host variation in tolerance to pathogens and parasites. Proc Natl Acad Sci U S A 105: 20786–20791.
27. Schneider DS, Ayres JS (2008) Two ways to survive infection: what resistance and tolerance can teach us about treating infectious diseases. Nat Rev Immunol 8: 889–895.
28. Medzhitov R (2009) Damage control in host-pathogen interactions. Proc Natl Acad Sci U S A 106: 15525–15526.
29. Seixas E, Gozzelino R, Chora A, Ferreira A, Silva G, et al. (2009) Heme oxygenase-1 affords protection against noncerebral forms of severe malaria. Proc Natl Acad Sci U S A 106: 15837–15842.
30. Ayres JS, Schneider DS (2008) A signaling protease required for melanization in Drosophila affects resistance and tolerance of infections. PLoS Biol 6: 2764–2773.
31. Ayres JS, Schneider DS (2009) The role of anorexia in resistance and tolerance to infections in Drosophila. PLoS Biol 7: e1000150.
32. Feng CG, Zheng L, Jankovic D, Bafica A, Cannons JL, et al. (2008) The immunity-related GTPase Irgm1 promotes the expansion of activated CD4+ T cell populations by preventing interferon-gamma-induced cell death. Nat Immunol 9: 1279–1287.
33. Bafica A, Feng CG, Santiago HC, Aliberti J, Cheever A, et al. (2007) The IFN-inducible GTPase LRG47 (Irgm1) negatively regulates TLR4-triggered proinflammatory cytokine production and prevents endotoxemia. J Immunol 179: 5514–5522.
34. Bottcher S (2001) Learning Bayesian networks with mixed variables Artificial Intelligence and Statistics, Key West, Florida. pp 149–156.
35. Heckerman D, Geiger D, Chickerling D (1995) Learning Baysian networks: The combination of knowledge and statistical data. Machine Learning: Microsoft Research. pp 197–243.
36. Pe'er D (2005) Bayesian network analysis of signaling networks: a primer. Sci STKE 2005: pl4.
37. Hartemink AJ, Gifford DK, Jaakkola TS, Young RA (2001) Using graphical models and genomic expression data to statistically validate models of genetic regulatory networks. Pac Symp Biocomput. pp 422–433.
38. Murphy KP (2001) The Bayes Net Toolbox for Matlab. Computing Science and Statistics 2001.
39. Hawkins DM, Basak SC, Mills D (2003) Assessing model fit by cross-validation. J Chem Inf Comput Sci 43: 579–586.
40. Van Rooijen N, Sanders A (1994) Liposome mediated depletion of macrophages: mechanism of action, preparation of liposomes and applications. J Immunol Methods 174: 83–93.